C O N T E N T S

Design and Implementation of a Textile-Based Embroidered Frequency Selective Surface

[1]İbrahim Üner 0000-0002-4669-5894
[2]Sultan Can 0000-0002-9001-0506
[1]Banu Hatice Gürcüm 0000-0001-9687-9598
[2]Asım Egemen Yılmaz 0000-0002-4156-4238
[3]Ertugrul Aksoy 0000-0002-6184-7112

[1]Textile Desing Dept. Art and Desing Faculty of Ankara Hacı Bayram Veli University, Ankara, Türkiye
[2] Department of Electrical and Electronics Engineering, Ankara University, Ankara, Türkiye
[3] Department of Electrical and Electronics Engineering, Gazi Universityi Ankara, Türkiye

Corresponding Author: İbrahim Üner, ibrahim.uner@hbv.edu.tr

ABSTRACT

This article presents the design, fabrication, and analysis of a textile-based band-stop frequency selective surface (FSS), in GSM, Wi-Fi, LTE, and WiMAX bands where the electromagnetic (EM) pollution is intense. The unit cell of the proposed FSS has been designed and simulated via a full-wave EM solver; CST Microwave Studio at the frequency of interest. In contrary to traditional FSS designs, which are printed on solid materials such as PCBs, this study presents an FSS considering a woven fabric as a substrate layer having features such as flexibility and compact weight. Two fabrication techniques have been considered one is conducted with a copper tape having a thickness of 35 μm denoted as CT FSS and the second one is conductive yarn embroidering technique denoted as CY FSS for the conducting pattern. Fabricated samples are evaluated in terms of transmission characteristics and a satisfactory agreement is obtained between CT FSS and CY FSS for both simulations and fabricated prototypes.

1. INTRODUCTION

Increasing demand on using electronic devices in our daily routine gave a rise on using the particular frequency bands, such as GSM (including 2G, 3G, LTE, and LTE-advanced sub-bands), Bluetooth, and Wi-Fi / Wi-Max in the wireless networks [1–3] and EM field emitting devices. Spotlight on these bands caused electromagnetic pollution since the devices have to satisfy the increasing demands of the users regarding high speed, large coverage, mobility, propagation, transmission power, spectrum efficiency, safety, and security [4–7]. The literature conveys significant amount of research on electromagnetic pollution [8], especially on electromagnetic interference (EMI). EMI which is a serious problem to cope with since it may cause electrical and electronic malfunctions, can prevent the proper use of the

radio frequency spectrum, can ignite flammable or other hazardous atmospheres [9], and more importantly can endanger human health [6, 9]. The evaluation of its side effects on human health has attracted many interests in medical studies, especially for people suffering from electromagnetic hypersensitivity [10], for environmental exposure to RF radiation [11, 12], and the measurement of electromagnetic radiation [12–19]. Consequently, EMI shielding, defined as the prevention of the propagation of EM waves from one region to another by using shield materials [20], is crucial to hinder those problems and to protect human beings and sensitive appliances.

To reduce the EMI [21], or to eliminate interference in desired frequencies [5], frequency selective surfaces (FSS) are used extensively in electromagnetic shielding

applications. They are periodic structures with conductive unit cell element arrays (patches or cavities) arranged on a dielectric substrate in any periodicity, any lattice, and any shape. FSSs can be designed as a band-pass or band-stop filter. The responses of their surface transmission and reflection on incident electromagnetic waves depend on the geometry and material properties of the unit cell as well as the periodicity [22]. Especially FSSs with the band-stop filter characteristics have the property of preventing the undesired interferences and transmitting the selected signals at a particular frequency simultaneously [23, 24]. FSS designs have widespread application area including enhancing the efficiency of the smart houses, which are getting popular since people demand amenity and comfort in the last few decades [21]. With these shielding characteristics, FSSs are used as radar absorption materials, radome design, and antennas [5].

In electronic and communications engineering, several EMI-shielding or EM-absorbing issues have been studied for decades. These can be summarized as; shielding effectiveness measurements [25], metamaterials, specialized materials used for shielding enclosures [26], conduction mechanisms, problems on waveguide aperture and ventilation [27], dielectric materials for absorber applications [28], electromagnetic wave absorbers [29, 30]. However, in the field of textile engineering EMI shielding and frequency selective surface (FSS) metamaterials are the most recent topics [5, 31].

All shielding materials must meet required specifications in chemical and corrosion resistance, tunable morphology, ease of operation, and financial cost [32, 33]. Besides these requirements, two basic demands urge the use of shielding material designs; one is weight reduction or lightweight, which reasons the employment of lighter materials such as aerogels [20], foam-based materials [34], magnetic nanoparticles [35], conductive polymer composites [36], and conductive textiles [37] within the fabrication process of shielding materials. The second is the demand for flexible designs implemented on curved platforms for any shielding applications. So, the development of electronics and material science leads the path to the scope of textile formation techniques making textile a research area in EMI shielding or FSS design. The studies proposed in literature emphasizes, conductivity is critical for EMI shielding of textiles [38]. Therefore, metal fibers, copper, or silver wires are used in spinning processes. Conductive dyes or solutions are applied to fabrics. For instance, to obtain a multilayered composite cloth structure against EMI, copper-coated interlining fabric and other textile components are sandwiched together to get composite EMI shielding fabric [39]. In another study, the EMSE (electromagnetic shielding effectiveness) values of copper plate and copper composite woven and knitted fabrics were compared [40]. In the study, PA6/silver mixture was used to investigate the EM shielding property of electrospun nanofibers [41]. For technical textile application, kevlar/stainless steel/polyamide fibers composite knitted specimens were tested at the frequency band of 0-3000 MHz [37].

The studies about shielding are focusing on the EMSE value, reaching an acceptable EMSE value in the relevant frequency range is mostly the main aim of the studies. Previous studies on EM shielding textiles, such as woven and knitted fabrics, generally indicate the effect of weaving or knitting structure and metal density in textiles [42]. Dielectric properties of textiles are not taken into account in EMI shielding studies. Also simulation studies based on EM wave theories are not needed before the experimental study. However, FSSs show EM filter behavior by stopping or passing EMI at the relevant frequency (e.g., 2.45 GHz).

This study presents a novel textile based FSS design fabricated with embroidering technique. The study includes the analysis of the band-stop characteristics of the proposed frequency selective surface denoted as Conductive Yarn (CY) FSS. The prototype CY FSS was fabricated, measured, and validated via the conventional band-stop frequency selective surface conducted with a copper tape denoted as CT FSS. The designs and simulations of the unit cells were carried out via a full-wave EM solver (CST Microwave Studio) at the frequency of interest. Samples were evaluated in terms of transmission characteristics (S21).

2. MATERIAL AND METHOD

In this article, band-stop FSS was designed for the frequencies of GSM, LTE, Wi-Fi, and WiMAX bands and simulated with a full-wave electromagnetic simulator, CST Microwave Studio. The EM wave filtering performances of FSSs were calculated, designed, and simulated by numerical method and produced with copper tapes onto cotton and cotton / PES blend fabrics. To create more flexible and durable textile-based FSS, conductive yarn was employed by embroidery technique subsequently and compared with simulations.

2.1 Material

FSS designs consists of conducting patches or cavities etched on the dielectric layer depending on the aim on blocking or passing the EM waves. The dielectric layers are commonly rigid and inflexible materials and patches are made of a thin copper plate as shown in Figure 1.
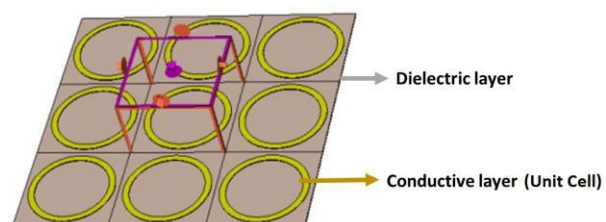

Figure 1. Conventional FSS structure

In the novel design proposed in this study, woven fabrics were used as a dielectric layer and embroidered conductive yarn was patterned as a conductive layer (unit cell). Since previous research has proven that plain woven fabrics are having a good aggrement with the designs, three samples (F1, F2, F3) are chosen plain woven with different thicknesses, weights, and setts together with only one twill woven (F4) sample. The physical properties of woven fabrics used for designs are presented in Table 1.

Table 1. Physical properties of textile materials

Code	Structure	Materials	Thickness	g/m²	Warp yarn. cm-1	Weft yarn. cm-1
F1	Plain 1/1	Cotton	0.6 mm	300	14	10
F2	Plain 1/1	Cotton	0.53 mm	170	17	17
F3	Plain 1/1	Cotton	0.40 mm	150	22	14
F4	Twill 2/2 S	Cotton/PES	0.55 mm	220	45	24

The first design, referred to as "CT FSS" standing for "copper tape FSS" is fabricated by agglutinating 35µm copper tape as a conductive layer on the fabric substrate in-house. On the other hand, the second design, referred to as "CY FSS" standing for "conductive yarn FSS" is fabricated by Shieldex Statex (117d/f17-2 ply) conductive yarn as a unit cell on a fabric substrate.

2.2 Method

2.2.1 Measurement of dielectric values of fabrics

The dielectric values of the woven fabrics are important to ensure filtering at the relevant frequencies. For this reason, the dielectric values of the fabric substrates are measured. In this study, the permittivity of the textile materials has been extracted employing Keysight 85070E Dielectric Probe Kit in the frequency interval 500-3000 MHz.

2.2.2 Unit-cell design and numerical results for the proposed FSS

Since free space measurements requires mass production of the unit cell designs for simplicity on measuring procedure waveguide measurement set up has been preferred for conducting the studies. For that aim both simulation and measurement setup for analyzing the unit cell responses Pasternack WR-229 waveguide (2.29 inches [58.166 mm] x 1.145 inches [29.083 mm]) having a frequency range of 3.3 GHz to 4.9 GHz is used. This waveguide is selected in particular since it satisfies the requirements for the band of interest as well as having low loss RF transmission lines capable of handling high power with high isolation. Since the unit cell is designed according to the measurement set up (WR-229 waveguide measurement set up), for ensuring the alignment, the side lengths of the unit cell are defined as having a length value of Lwg and a width value of Wwg so the unit cell fit in the waveguide perfectly. The textile

substrate having a thickness value of Hs is considered as the substrate having the permittivity value of Ɛr and the resonator pattern is proposed in Figure 2.
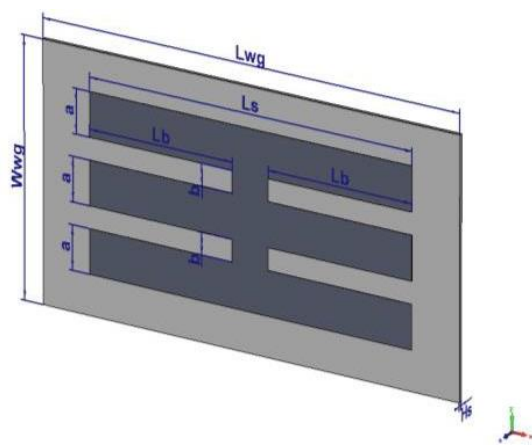
Figure 2. Unit cell design of FSS with its parameters

As shown in Figure 2, the textile dielectric substrate is represented with the light grey part of the unit cell and the dark grey part represents the conductor material having the dimensions of Ls, a, b and Lb. The optimized unit cell has the dimensions of Lwg = 58.17 mm, Wwg = 29.08 mm, and Hs = 0.5 mm. Resonator dimensions Ls, Lb, a, and b are given as 45 mm, 20 mm, 5 mm, and 2.5 mm, respectively. The boundary conditions are assigned as electric boundary conditions on the x and y axes and open boundaries on the z-axis. As a port assignment, a waveguide port is assigned.

2.2.3 Embroidery process of FSS unit cell

The embroidery technique was used for the production of FSS and the patterns were created with the PFAFF Creative 1.5 embroidery machine. Shieldex Statex 117 / f 17 2 plies conductive yarn was used in the formation of the conductive patch. The optimized FSS unit cell was drawn in the premier + embroidery software and transferred to the embroidery machine (Figure 3a-b-c). The embroidery density applied in the study includes 154 punch / cm² in complex fill and a total of 1396 punch and punch angle is 450 within the FSS design.

Today, embroidery design can be done with CAD systems, which provides unlimited patterning possibilities with embroidery technique. This technological advance has made it possible for digital images to be directly embroidered using a computer-aided embroidery machine.
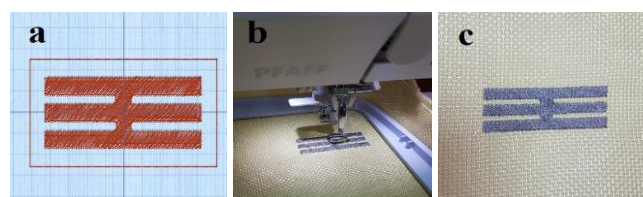
Figure 3. CY FSS (a) patterning of FSS on Premier + software, (b) embroidery process of FSS, (c) embroidered FSS

2.2.4 Measurement set-up

S-parameters (|S11|, |S12|, |S21|, |S22|) Considered for evaluating the band stop and band pass characteristics of the fabricated samples. |S11| (magnitude of reflection coefficient) indicates how much electromagnetic waves are reflected from the medium, |S21| (transmission coefficient) indicates how much electromagnetic waves are transmitted through a medium [14]. In this study, |S21| is the key parameter For the evaluation of the band characteristics of the proposed designs. Pasternack WR-229 waveguide having a frequency range of 3.3 GHz to 4.9 GHz is connected to Rohde & Schwarz ZVL13 Vector Network Analyzer, which is capable of measuring a frequency interval of 9 kHz - 13.6 GHz, is used throughout the measurements and the cross-section of the waveguide is shown in Figure 4.

The unit cell simulation is mimicked throw-out the measurement set up and the sample is located at the midpoint of the waveguide by using foams. The foams are critical in satisfying the stability and they are having approximate permittivity and permeability values of air so that it has a negligible effect on measuring the scattering parameters; however, it helps to sample to stay firm.
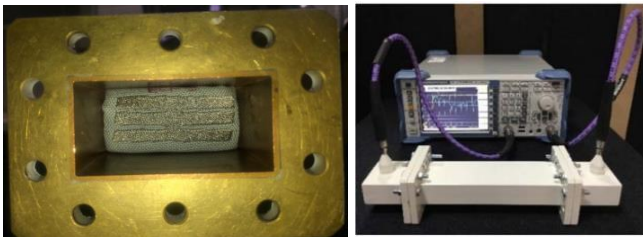
**Figure 4.** One of the proposed sample in the WR-229 rectangular waveguide

3. RESULTS AND DISCUSSION

3.1. Measurement of dielectric values of fabrics

The dielectric properties of four different textile samples (F1, F2, F3, F4) within the scope of the study were examined between 500 MHz and 3000 MHz. ε_r' values for each fabric sample were measured 3 times (M1, M2, and M3 are corresponding to the first, second, and third measurements, respectively) and tested at 201 different frequencies scaled between 500 MHz and 3000 MHz with an accuracy of 12.5 MHz. Accordingly, while the maximum ε_r' values occurred at 537.5 MHz in all samples, the minimum ε_r' values were observed at 950 MHz in all samples except F1which peaked at 2287.5 MHz for minimum ε_r'.

As presented in Figure 5, the dielectric coefficients decrease as the frequency increase in all fabric types. In the dielectric studies of textiles in the literature [43–48], it is seen that external factors such as humidity, temperature, and frequency range affect the measured values. In this respect, there is a concordance between our study and the literature. Moreover, the result of an inverse relationship between the frequency increase and the dielectric coefficient has been revealed. In reviewing the literature, no data was found on the association between frequency and dielectric coefficient of textiles, hence it maybe contribution to literature. Although the resonance dependent dielectric tendency of the F1, F2, and F3 was similar, each sample did not show exactly the same dielectric properties due to the differences in the physical properties (thickness, weight, and sett values) of the fabrics.

F1

F2

F3

F4
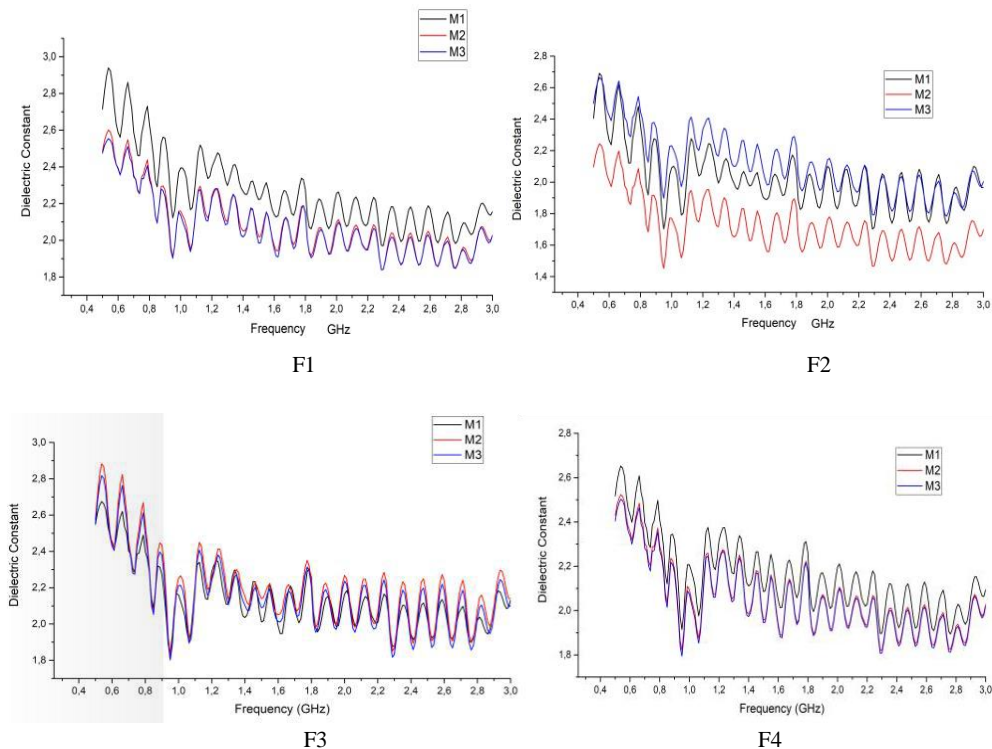
Figure 5. Relative Permittivity values of samples (see Table 1) depending on the frequency

3.2 Measurement results of FSS

The effect of the dielectric coefficient on the frequency is seen in the simulation study performed by taking into account the maximum and minimum εr' values of the fabrics under test (Figure 6).

Firstly, proposed textile-based structures were compared as a function of minimum and maximum εr' values depending on frequency. In Figure 6, when the εr' value increased, the resonance frequency shifted to the down side. Thus, the conclusion can be drawn that the dielectric permittivity of fabrics affects the resonance frequency of FSS. This finding is consistent with [49]'s statement, which gives information about permittivity.

According to Figure 6, the corresponding upper and lower frequencies of F1 are 4.19 GHz and 3.74 GHz for the simulations as a function of εr' and 4.19 GHz for the CT FSS measurement respectively. For F2, the resonance frequencies are 4.38 GHz and 3.79 GHz for the simulations, and 4.38 GHz for CT FSS. The resonance frequencies of F3 are 3.76 GHz and 3.56 GHz for the simulations, and 4.47 GHz for CT FSS. For F4, 4.31 GHz, and 3.93 GHz for simulations and 4.28 GHz for the CT FSS measurement. The % error fr calculated via equation (1) based on minimum εr' is lower than 1% compared to copper tape, except F3. Therefore, it was stated that the measurements of the CT FSS samples, except F3, matched quite well with the minimum εr' simulation results. For this reason, it was decided to use F1 and F4 fabrics in the CY FSS fabrication phase of the study.

$$\% \ Error \ fr = \left(\frac{fr \ simulated - fr \ measured}{fr \ simulated} \right) x100 \quad (1)$$
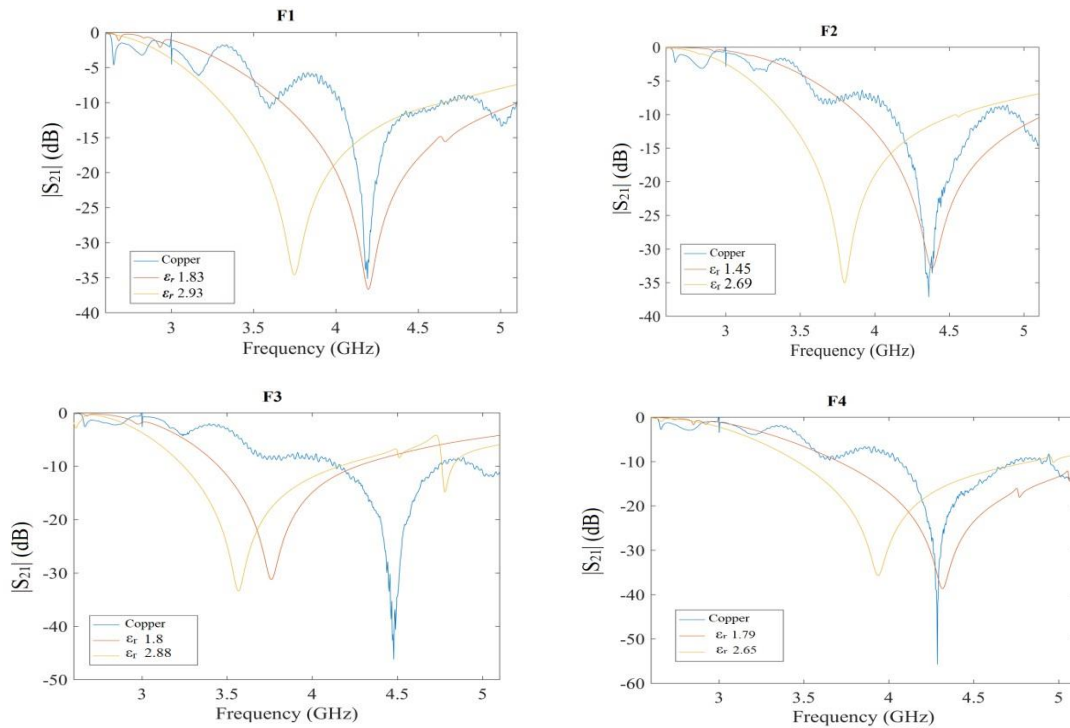
Figure 6. |S21| characteristics for CT FSS a) simulations and CT measurements
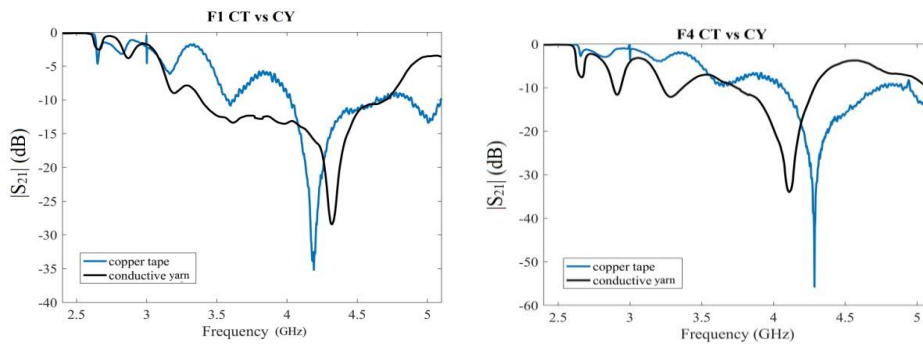
Figure 7. Measurement of CT FSS and CY FSS Resonance frequencies and |S21| (dB) values of F1 and F4

The good results of CT FSS measurements compared to simulation results have provided the opportunity to use textiles as a dielectric layer in FSSs. There are similarities between the attitudes expressed by [10] in this study and those described by us. Since the copper tapes used in CT FSS are not as flexible as the fabric and resistant to environmental conditions such as rubbing, wetting, bending, and folding, the FSS unit cell is produced with conductive yarn to solve these problems. The embroidered unit cell structures (CY FSS) are more compatible with the textile structure and more flexible and durable than CT FSS. The results of CT FSS and CY FSS were compared in Figure 7. Accordingly, the conductive yarn results for F1 are 4.3208 GHz and –28.46 dB, while the copper tape results are 4.1918 GHz and –35.2 dB, respectively. The conductive yarn results for F4 are 4.11 GHz and –34.01 dB, while the copper tape results are 4.2858 GHz and –55.77 dB, respectively. As can be seen from figure 7, there is a slight frequency difference between CT FSS and CY FSS, while transmission coefficients are acceptable (under -10 dB) in both. This also accords with the researchers' earlier observations, which showed that there are differences between simulation/copper and textile FSS [10, 50, 51].

4. CONCLUSION

This project was undertaken to design a textile-based EM filter and evaluate its filtering performance versus its rigid counterpart. To eliminate the weightiness and stiffness disadvantages of conventional FSS, four different fabric structures were designed as the dielectric layer and the unit cell was fabricated by copper tape (CT FSS) and conductive yarn (CY FSS). To design FSS, the dielectric permittivity of four different fabrics was tested between 500 MHz and 3000 MHz with 12.5 MHz accuracy.

The conclusion can be drawn that the dielectric permittivity is dependent on the physical properties of the textile and has an effect on the resonance frequency as well as the geometric structure of the conductive surface (unit cell). Also, as the dielectric value increases, the resonance frequency of the FSS decreases.

Measurements of CT FSSs made by agglutinated copper tape onto fabric are well-matched with simulations because of the perfectness of the unit cell geometry. However, the inflexibility of copper tape and its weakness against environmental factors constitute a disadvantage. The unit cell produced with conductive yarn is thought to be a better fit with the textile dielectric layer due to the embroidery technique. The experimental results of CY FSS have been compared to CT FSS and satisfactory agreement is obtained.

As a result of this study, it can be concluded that the embroidery samples are having approximate performance in terms of filtering and they are good candidate for EM filter applications. To increase the efficiency of the embroidery technique in this regard, researches on embroidery parameters such as stitch density, surface filling method, and stitch slope will yield positive results.

REFERENCES

1. Zulkifli CZ, Hassan HN, Ismail W, Semunab SN. 2015. Embedded RFID and wireless mesh sensor network materializing automated production line monitoring. *Acta Physica Polonica A.* 128 (2B), 86-89.

2. Basit A, Qureshi IM, Khan W, Malik AN. 2016. Range–angle-dependent beamforming for cognitive antenna array radar with frequency diversity. *Cognitive Computation.* 8(204), 204-2016.

3. Mukanova B, Mirgalikyzy T. 2015. Simulation of the electric field of a point source on the relief surface. *Acta Physica Polonica A* 128(2B), 142-144.

4. Karan Y, As N, Şahin ME. 2017. Investigation of GSM, LTE and WI-FI electromagnetic radiation in dwellings. *Acta Physica Polonica A 132(3),* 509-512.

5. Can S, Karakaya EU, Yılmaz AE. 2020. Design, fabrication, and measurement of textile-based frequency selective surfaces. *Microwave and Optical Technology Letters.* DOI: 10.1002/mop.32474.

6. Eurocontrol, "Criteria for selection of frequency band(s) for the future aeronautical communication infrastructure," 2005. [Online]. Available: https://www.icao.int/safety/acp/ACPWGF/ACP-WG-F-13/WP36-Band Selection criteria for AI 1[1].6 ITU.doc.

7. Velentza O. 2015. Electromagnetic pollution - pathological effects of electromagnetic fields in man. *AASCIT Journal of Health*.2(6) 74-79.

8. Richman R, Munroe AJ, Siddiqui Y. 2014. A pilot neighborhood study towards establishing a benchmark for reducing electromagnetic field levels within single family residential dwellings. *The Science of the Total Environment.* 466, 625-634.

9. Tan K-S, Hinberg I. 2004. Electromagnetic interference with medical devices: in vitro laboratory studies and electromagnetic compatibility standards, In Biomedical Engineering. Editor: Dyro J F, *Clinical Engineering Handbook*, Academic Press, 254-262.

10. Hesarian MS, Shaikhzadeh NS, Sarraf SR. 2018. Design and fabrication of a fabric for electromagnetic filtering application (experimental and modeling analysis). *The Journal of the Textile Institute* (109), 775–784.

11. Ayinmode BO, Farai IP, Pacific J. 2014. Evaluation of GSM radiation power density in three major cities in Nigeria. *International Journal of Environmental and Ecological Engineering* 8(10), 740 - 743.

12. Seyfi L. 2013. Measurement of electromagnetic radiation with respect to the hours and days of a week at 100kHz–3GHz frequency band in a Turkish dwelling. *Measurement* 46(9), 3002-3009.

13. Cansiz M, Abbasov T, Kurt MB, Çelik AR. 2016. Mobile measurement of radiofrequency electromagnetic field exposure level and statistical analysis *Measurement* 86, 159-164.

14. As N, Dilek B, Şahin ME, Karan Y. 2014. Electromagnetic pollution measurement in the RTE university campus area *Global Journal on Advances Pure and Applied Science* 3, 65.

15. Urbinello D, Joseph W, Huss A, Verloock L, Beekhuizen J, Vermeulen R, Martens L, Röösli M. 2014. Radio-frequency electromagnetic field (RF-EMF) exposure levels in different European outdoor urban environments in comparison with regulatory limits *Environ International* 68, 49.

16. Sahin ME, As N, Karan Y. 2013. Selective radiation measurement for safety evaluation on base stations *Gazi University Journal of Science* 26(1), 73-83.

17. Eyüboğlu E, Kaya H. 2010. December. Measurement of TV/radio transmitters at Trabzon-Boztepe region induced electric field strength and evaluation of results. In: Electrical, Electronics and Computer Engineering Editor (Ed) IEEE , (ELECO) 2010 2010 National Conference on Electrical, Electronics and Computer Engineering Bursa, Turkey.

18. Henderson SI, Bangay MJ. 2005. Survey of RF exposure levels from mobile telephone base stations in Australia. *Bioelectromagnetics Journal* 27, 73.

19. Akkurt I, Mavi B. 2010. The measurement of radiation dose around base-stations. *Scientific Research and Essays* 5(15), 2088-2090.

20. Zhang L, Bi S, Liu M. 2019. Lightweight electromagnetic interference shielding materials and their mechanisms, *Electromagnetic Materials and Devices*. 1–20.

21. Can S, Kapusuz KY, Yılmaz AE. 2017. Optically transparent frequency selective surface for ultra-wideband applications. *Microwave and Optical Technology Letters* 59 (12), 3198-3200.

22. Munk BA. 2000. *Frequency Selective Surfaces: Theory and Design.* Hoboken, NJ, USA: John Wiley & Sons, Inc. DOI: 10.1002/0471723770.

23. Karahan M, Aksoy E, Yavuz YA. 2017. June. Frequency selective surface design to reduce the interference effect on satellite communication. In IEEE, 8th International Conference on Recent Advances in Space Technologies (RAST), 221–223. Istanbul, Turkey.

24. Karahan M, Aksoy E. 2020. Design and analysis of angular stable antipodal F-type frequency selective surface with multi-band characteristics. *International Journal of RF and Microwave Computer Aided Engineering* (30), 1-16.

25. Fang CH, Zheng SQ, Tan H, D. Xie G, Q Zhang, 2008. Shielding effectiveness measurements on enclosures with various apertures by both mode-tuned reverberation chamber and GTEM cell methodologies, *Progress In Electromagnetics Research B* 2, 103–114.

26. Atxaga G, Marcos J, Jurado M, Carapelle A, Orava R. 2012 October. Radiation shielding of composite space enclosures, 63rd International Astronautical Congress, Naples, Italy.

27. Li M, Nuebel J, Drewniak JL, DuBroff RE, Hubing TH, Van Doren TP. 2000. EMI from airflow aperture arrays in shielding enclosures—experiments, FDTD, and MoM modeling, *IEEE Transactions on Electromagnetic Compatibility* 42(3), 265–275.

28. Hamat Ö. 2014. Design and development of electromagnetic wave absorbing composites effectıv at microwave frequencies Middle East Technical University, (Master's Thesis) Department of Metallurgical and Materials Engineering, Ankara.

29. Costa F, Monorchio A, Manara G. 2016. Theory, design and perspectives of electromagnetic wave absorbers. *IEEE Transactions on Electromagnetic Compatibility* 5(2), 67–74.

30. Watts C, Liu X, Padilla W. 2012. Metamaterial electromagnetic wave absorbers. *Advanced Optical Materials* 24(23) 98-120.

31. Michalak M, Brazis R, Schabek D, Krucińska I. 2019 June. Textile metamaterials, in AUTEX 2019-19th World Textile Conference on Textiles at the Crossroads, Ghent, Belgium.

32. Gairola P, Gairola SP, Dhawan SK, Tandon RP, Gupta V, Purohit LP, Sharma S. 2018. Carbon material-nanoferrite composite for radiation shielding in microwave frequency, *Integrated Ferroelectrics* 186(1), 40–48.

33. Gonzalez M, Pozuelo J, Baselga J. 2018. Electromagnetic shielding materials in GHz range. *The Chemical Record* 8(7–8), 1000–1009.

34. Wang YY, Zhou ZH, Zhou CG, Sun WJ, Gao JF, Dai K, Yan DX, Li ZM. 2020. Lightweight and robust carbon nanotube/polyimide foam for efficient and heat-resistant electromagnetic interference shielding and microwave absorption. *ACS Applied Materials & Interfaces* 12(7), 8704-8712.

35. Parveen S, Veena C, Vijayan N, Kotnala RK. 2012. Improved electromagnetic interference shielding response of poly(aniline)-coated fabrics containing dielectric and magnetic nanoparticles. *The Journal of Physical Chemistry C* 116(24), 13403-13412.

36. Valente R, De Ruijter C, Vlasveld D, Van Der Zwaag S, Groen P. 2017. Setup for EMI shielding effectiveness tests of electrically conductive polymer composites at frequencies up to 3.0 GHz. *IEEE Access* (5), 16665-16675.

37. Demiray Soyaslan D. 2020. Design and manufacturing of fabric reinforced electromagnetic shielding composite materials. *Tekstil ve Konfeksiyon*, 30(2), 92-98.

38. Çetiner S, Köse HA. 2021. Systematic study on morphological, electrical and electromagnetic shielding performance of polypyrrole coated polyester fabrics. *Tekstil ve Konfeksiyon* 31(2), 111-121.

39. Šaravanja B, MalariĆ K, PušiĆ T, Ujević D. 2020. Exposure analysis of electromagnetic shield effect of a copper composite cloth structure. *Tekstil ve Konfeksiyon* 30(2), 139-143.

40. Özkan İ. 2020. Investigation on the electromagnetic shielding performance of copper plate and copper composite fabrics: A comparative study. *Tekstil ve Konfeksiyon* 30(2), 156-162.

41. Sancak E, Özen MS, Erdem R, Yılmaz AC, Yüksek M, Soin N, Shah T. 2018. PA6/silver blends: Investigation of mechanical and electromagnetic shielding behavior of electrospun nanofibers. *Tekstil ve Konfeksiyon* 28 (3), 229-235.

42. Örtlek HG, Güneşoğlu C, Okyay G, Türkoğlu Y. 2012. Investigation of electromagnetic shielding and comfort properties of single jersey fabrics knitted from hybrid yarns containing metal wire. *Tekstil ve Konfeksiyon* 2012 (2), 90-101.

43. Ibanez-Labiano I, Alomainy A. 2020. Dielectric characterization of non-conductive fabrics for temperature sensing through resonating antenna structures. *Materials* (13), 1271.

44. Sankaralingam S, Gupta B. 2010. Determination of dielectric constant of fabric materials and their use as substrates for design and development of antennas for wearable applications. *IEEE Transactions on Instrumentation and Measurement* (59), 3122– 3130.

45. Mustata FC, Mustata A. 2014. Dielectric behaviour of some woven fabrics on the basis of natural cellulosic fibers. *Advances in Materials Science and Engineering* (2014).

46. Lesnikowski J. 2012. Dielectric permittivity measurement methods of textile substrate of textile transmission lines. *Przegląd Elektrotechniczny* (88), 148-151.

47. Pourova M, Zajicek R, Oppl L. 2008, April. Measurement of dielectric properties of moisture textile. In: 2008 14th Conference on Microwave Techniques. 1–4. Prague, Czech Republic.

48. Cerovic DD, Asanovic KA, Maletic SB. 2013. Comparative study of the electrical and structural properties of woven fabrics. *Composites Part B: Engineering* (49), 65–70.

49. Delihasanlar E, Yüzer AH. 2020. Wearable textile fabric based 3D metamaterials absorber in X-band. *Applied Computational Electromagnetics Society Journal* 35 (2), 230–236.

50. Alonso-Gonzalez L, Ver-Hoeye S, Fernandez-Garcia M. 2018. Layer-to-layer angle interlock 3D woven band stop frequency selective surface. *Progress in Electromagnetics Research* (162), 81–94.

51. Guan F, Xiao H, Shi M. 2017. Realization of planar frequency selective fabrics and analysis of transmission characteristics. *Textile Research Journal* (87), 1360–1366.

A Vibro-Haptics Smart Corset Trainer for Non-Ideal Sitting Posture

Mehmet Arda Özden[1] 0000-0003-4882-0190
Eda Acar[2] 0000-0002-4468-5297
Mücella Güner[2] 0000-0001-8910-7338
Hasan Yıldız[1] 0000-0002-3432-2249
Mahmut Pekedis[1] 0000-0002-3350-0277

[1]Ege University / Faculty of Engineering / Department of Mechanical Engineering, 35100, Bornova, Izmir, Türkiye
[2]Ege University / Faculty of Engineering / Department of Textile Engineering, 35100, Bornova, Izmir, Türkiye

Corresponding Author: Mahmut Pekedis, mahmut.pekedis@ege.edu.tr

ABSTRACT

This study aimed to develop a vibro-haptics feedback based smart corset to stimulate humans to be in ideal posture by monitoring the spline in thoracic vertebrae of T5-T12 levels, and provide a vibro-tactile stimuli to human's skin at lumbar L3 level. A corset contains a microcomputer, sensors and an actuator was implemented on 12 participants for 2 cases to determine its efficiency. In the first case, tactile stimuli was not provided to the participants, while in the second case tactile stimuli was ensured. The results showed once the vibro-tactile stimuli was represented to the participants, their posture regime improved significantly with a value of 53.13±23.14 %. Moreover, it was also observed that their non-ideal postural duration significantly decreased. These results suggest that the corset provides vibro-tactile feedback that encourage humans in seated posture to beneficial postural habits while using computers.

1. INTRODUCTION

Incorrect or non-ideal posture is a problem that becomes increasingly widespread in today's world. This can be affected by daily activities, physiological and living conditions, and it has a great role in decreasing the quality of life. It can also cause musculoskeletal problems which are the second most common and costly spinal disorder [1]. Low back pain is one of these problems [2] which contributes to many factors such as physical [3-4], psychological [5], biological [6] and genetic factors [7]. One of the most usual strategies used by physiotherapists to the management of low back pain is providing advice to the patients on spinal postures. There are widely accepted clinical beliefs concerning ideal or non-ideal posture [2]. However, there is not any consensus upon an ideal posture during sitting [4]. An unbalanced posture can affect the person's posture while standing and walking [8]. In slump sitting, the intervertebral disks are subjected to compressive stresses at the anterior part of the fibrous ring, posterior migration of the nucleus [9] and an increase in these stresses may cause damages to intervertebral disks [10]. It has been reported that an increase in lumbar flexion in slump sitting can cause lower back pain [11] due to higher compression stresses created in the spine compared to the "neutral" sitting [4, 12]. These stresses may produce intervertebral disk degeneration as well as damage and misalignment of vertebrae. Hence, the correct posture is the principal factor for the health of the spine [13]. Some authors have suggested lordotic seated postures in sitting can prevent this damage [14, 15]. Furthermore, it has been reported that a sitting posture which complied with the natural curvature of the spine, and appeared comfortable

without excessive muscle stretch includes advantages [2].

Some instruments such as inclinometers [13, 16], radiographic images [17], 3D electromagnetic tracking systems [4], photographs [2], camera [18], motion capture systems [19], laser scanners [20] have been widely deployed to measure and to analyze the curvature of the spine. However, many of these expensive systems used in clinics and labs may be costly and not fit to monitor day to day conditions for the users. In order to monitor and control the posture for daily uses, haptic stimuli has been performed in various studies [8, 21]. This type of sensory stimuli has largely been explored in postural control using the principles of sensory substitution by the neuroscience community. Sensory substitution refers to a multitude of different processes of reorganization within the brain, each of which the way information is processed and may ultimately result in behavior change [22]. Typically, vibration actuators with an array have been implemented as vibrotactile feedback devices due to the fact that they can provide additional information without interfering with the basic functions like hearing or seeing [8,21,23,24]. To monitor and to improve the posture for daily regular users, several portable and haptic feedback-based devices have been proposed [25]. For instance, Zhang et al., embedded force sensors to the chair to determine the sitting posture and used vibro-tactile feedback to encourage the users to correct their postures [26]. Barone et al., performed flexible strain sensors to monitor the thoracic spinal angles and provided visual feedback during flexion and extension [21]. A network of three inertial measurement units were used to determine the thoracic and lumbar angles and provide auditory feedback to encourage users to a neutral standing position [19]. In brief, fiber optic [27], inertial [28] and flexible strain [21] sensors are the most typical sensors that have been suggested to monitor the posture. In addition to the studies performed by academic researchers, wearable posture trainers have also attracted the commercial markets such as Jins Meme, Alex+, Nadi X, Sense U, Upright Go posture trainer and Mevics [29]. However, the details about the determinations of posture using these devices are not available since they are for commercial purposes. The majority of these devices are built with processor, microcontroller, accelerometer, gyroscope, magnetometer, inertial sensor and feedback instruments. The feedback is provided via vibrotactile cues allow tracking and logging the posture via app-based graphics and mostly attached to the skin or garment via adhesive clips or pins. Most of them determine the posture from a single node. Hence, it is not certain whether they have a capability to assess the relative joint angle using a single node.

In this study, we aimed to design a corset made of fishline breathable stretch fabric, assembled with a low weight and low-cost instrument to improve the users' postures in sitting by allowing them vibro-haptics feedback. Different from the majority of the available devices, the sensors can be located to the place specifically for the user's spine, and the smart corset fits the user's abdomen, and allows to measure joint angle. The idea here is once the user's posture exceeds slouching posture angle limit, the vibro haptic motor is actuated to encourage humans to adjust his/her posture. The main goal is to evaluate how such a smart corset with vibrotactile feedback could improve the sitting posture of the user.

The study is organized as follows. First, textile material used in smart corset device is demonstrated. Next, the hardware and software framework of this device is described. Then, the results obtained from participants are presented. Finally, the performance of the device is summarized and discussed in terms of participants' posture improvement rate.

2. MATERIAL AND METHOD

2.1 Textile material

Various fabric samples such as fishline sketch and knitted fabric containing 92%PES 8%EL were supplied from various manufacturers. The goal is to choose a fabric that provides reasonable properties in terms of comfort, moisture transfer and air permeability. Since the PES / EL blended fabric does not wrap the body tightly as the gutted fabric, it leads to undesirable consequences such as changing the position of the sensors/ actuator and making a bulge at the sensor's location. Therefore, fishline stretch fabric (Misineteks Tekstil, Turkey) was preferred due to its sensitivity of transfering the vibrotactile stimuli to the human body. Various experimental tests such as air permeability and moisture transmission were performed on fish line samples to characterize the fabric [30, 31]. For the weight per unit area (g/m^2) test, the measurement was performed on 5 samples in accordance with ISO 3801 standard [32]. Those samples were cut with a grammage stencil with an area of 100 cm^2 and weighed in precision balance. For the measurement of air permeability, the test was performed for 10 samples, and each has an area of 5 cm^2. The test was carried out using Fx 3300 Instrument at pressure of 100 Pa in accordance with ASTM D 737 [31]. For the determination of transmission properties, a moisture management tester instrument was implemented for 5 samples, and each has dimensions of 8x8 cm^2. The fabric has a plain weave that includes 70 denier polyamide warp yarn, 1200 number gipe yarn (150 filament polyester coated over elastane) and polyamide fishline yarn with a thickness of 0.15 mm and 200 dtex. The weft and warp density of the fabric are 12 and 25 threads/cm, respectively. It is 100% flexibile, and a typical weave plan of the fabric is shown in Figure 1.

Once the fabric was characterized, the next step was to sew the corset using a lockstitch machine. Velcro fasteners were used on the corset for upper straps, waist region and placement of electronic devices. The corset's fabric and velcro bands were stitched with 100% PES sewing. The corset consists of four main components which are upper straps from the right and left, back and belt parts. Note that,

it is not covering the body completely, but only a part of it. The front and back straps have a length of 6 cm while the waistband has 13 cm (Table 1). Three different corset sizes for female and male were manufactured. They fit on users' abdomen comfortably and help them not to be in extreme slump posture. Furthermore, the corsets do not have to be in touch with the body's skin directly, and could be worn on the specific user's garment. Velcro fasteners were used on the corset for upper straps, waist region and placement of electronic components.
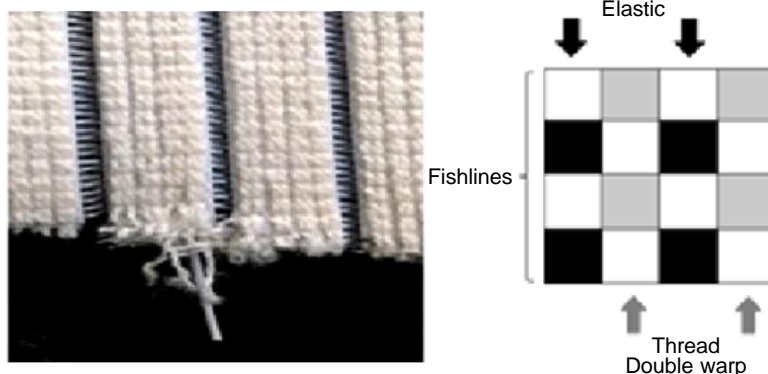
Figure 1. Fishline stretch fabric and its weave plan

Table 1. The dimensions of the corset

Strap	Female		Male	
	Length (cm)	Width (cm)	Length (cm)	Width (cm)
Front	62	6	78	6
Back	39	6	45	6
Waistband	84	13	102	13

2.2 Hardware and software setup

The instrument developed in this study consists of two absolute orientation sensors (BNO055, Bosch, Sensortec, Germany), a microcomputer (Raspberry Pi Zero, Raspberry Pi Org, UK) and a vibro actuator (Precision Microdrives, UK). Total weight of the instrument is 145 g. These components are powered by 2 x 1550 mAh Lipo batteries. Since 1S2P LiPo battery's voltage level is 3.7 V, a 5 V step-up boost converter was used to supply the orientation sensors and the micro-Computer. The vibration actuator is powered with a rail from 3.7 V LiPo battery directly without any regulator. The intensity of the vibro actuator can be adjusted using PWM (Pulse-width modulation), while it is excited with constant current. The device, orientation sensors and vibro-haptic actuator are enclosed in two different 3D printed boxes that have dimensions of 94 x 84 x 23 mm, and 30 x 28 x 9 mm. Each of these units is attached to the corset with velcro; so the region of each enclosed unit can be modified for users. Although there is not any general indicator that describes the ideal sitting posture with quantitative data [4], it is reported that a posture which matches the natural shape of the spine and appears comfortable without excessive muscle stretch has advantages [2]. In this study, T5-T12 levels were assessed as reference landmarks [33]. Therefore, one enclosed absolute orientation sensor was located at T5, and the other at T12 (Figure 2). It is noted that, while these sensors can measure lateral bending and extension-flexion angles of the spine, the instrument is adjusted to collect only the flexion- extension measurements with a sampling rate of 5 Hz. The enclosed vibro-tactile unit is attached to the L3 level of the user via velcro, and excited when the threshold exceeds. The reason for choosing this level is to allow a person to sense the vibro-actuation stimulus noticeably and may also avoid noises due to environmental effects [8]. The communication between the microcomputer and the orientation sensors are performed using I^{2}C (Inter Integrated Circuit) protocol. The reason for preferring this protocol is that it allows communication with multi sensor nodes with a single data cable on 8-bit address system. The processing unit includes an expansion unit to store the data in MicroSD. Moreover, it also includes a modem to transfer the data over Wi-Fi. The device can be recharged with a micro-USB cable. In power consumption tests, it has been observed that the device can operate about 6 hours continuously with 2x1550 mAh LiPo rechargeable battery.

Figure 2. Placement of sensors and actuator

Once the hardware setup is completed, the next stage is to develop an algorithm that monitors the posture and determines the incorrect posture (Figure 3). It starts when the mi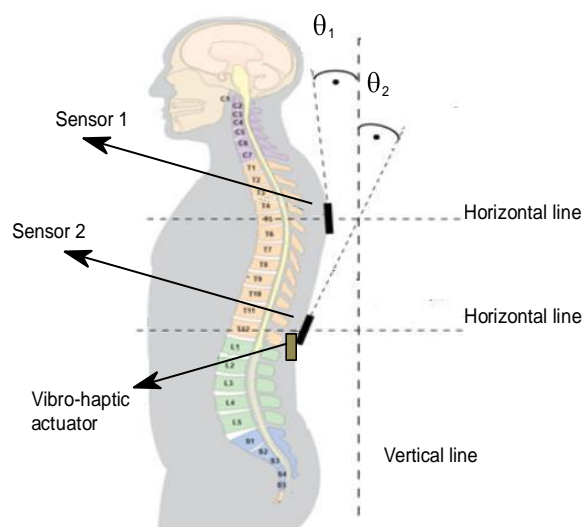cro-computer is powered on and then it checks the sensors' status by trying to acquire sample data from them. Here, θ_1, θ_2 and θ_r refer to the 1st, 2nd, and relative angle (θ_1-θ_2) of the two sensors. If the process is successful, it waits for the operator's command for calibration (Figure 3). In this process, the user is instructed to pose upright verbally. Then the angle θ_r is saved for later calculations as an offset value θ_o. Next, the user is instructed to pose in a non-ideal posture which makes the user uncomfortable by slouching his/her spine. Then, the angle difference for this position is measured again and stores as θ_r. By subtracting the offset value θ_o from this angle θ_r, the algorithm computes a new value and stored it as a threshold value θ_t. Once the calibration process is completed, the program enters an infinite while loop. The algorithm subtracts the offset value θ_o from the θ_r and stores the new induced angle difference value as θ_i. This θ_i value is logged with a time tag and stored as time series in the MicroSD card. Next, if θ_i is lower than θ_t the algorithm assumes that there is no anomaly "ideal posture", and it returns to the first step in the loop and continues. On the other hand, if θ_i is higher θ_t, there is an anomaly "non-ideal posture", and it alerts the user. Then it creates a warning event by using θ_i value with time info and then logs the event in the MicroSD card. The final step is to transfer the data. If a WiFi internet connection is available, then the device sends this event to the remote server over TCP/IP. If not, it logs the event in the MicroSD card in a separate file to send it later. Finally, the process returns the first step of the algorithm loop. The algorithm embedded in the micro-computer was developed using PYTHON 3.

2.3 Human test procedure

Twelve healthy participants (9 females 27 to 58 yrs, 3 males 32 to 40 yrs) from academic staff and graduated students have enrolled in the study. The clinical ethical review board of the Ege University approved the study with a designated document ID of 103-2016. All participants provided written consent to participate to study. First, the participant wears the corset that is suitable for him/her (Figure 4). Then, the enclosed 1st, 2nd sensor, and vibro-haptic actuator are adjusted to be on user's T5, T12, and L3 landmarks. Second, the participant sits in front of his/her own computer. We encouraged each user to arrange the height of the chair and computer before the tests. Third, we asked to sit what he/she considers to be an ideal and non-ideal for the calibration process and determination of range of motion (ROM) with the directions of the physiotherapist. If the participant slouches to a limit out of ROM threshold, the vibro-haptic actuator warns the user to correct his/her posture.
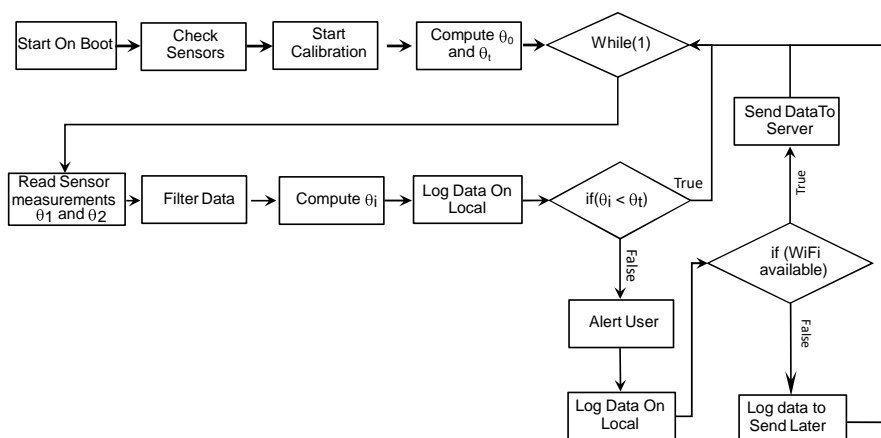

Figure 3. Flowchart of the algorithm used in microcomputer

Figure 4. A participant with a vibro-haptic corset from various views

The investigation was implemented for 2 cases to figure out the efficiency of the smart corset. In the first case, tactile stimuli was not provided to the participants while in the second case tactile stimuli was ensured. The idea of the first case was to determine the user's habitual daily sitting posture, while in the 2nd case was to investigate how well the vibro-tactile stimulation could rehabilitate the user's posture by changing his/her cognitive attitude. The duration of each test case was one hour and performed from 2:00 PM to 3:00 PM to ensure the same daily conditions.

2.4 Statistical assessment

Statistical differences between case 1 and 2 were investigated through one-way analysis of variance and paired *t*-test by imposing a confidence interval of 95%. Differences between the cases are significant for *p*-value is lower than 0.05 level. The statistical assessments were performed using SPSS 22.0. Furthermore, the participants' scores were processed using receiver operating characteristics (ROC) curves to determine how well their results in case 1 and 2 could be discriminated using MATLAB 2012. ROC curves summarize any possible classification between groups' datasets. They are typically established by plotting the true positive rate (TPR) against the false positive rate (FPR) at various threshold settings. For a curve close to the TPR left vertical axis, the classification score increases, while it is close to the FPR horizontal axis the score decreases. Therefore, the best possible classification would yield a point in the upper left horizontal corner point (0,1). The performance of the curve is assessed via area under curve (AUC) and critical optimum point (COP). The best performance is observed for AUC=1, while the worst is for AUC =0.5. Generally, an AUC of 0.5 is considered "no separation" between groups, 0.6 to 0.7 is "sufficient", 0.7 to 0.8 is "acceptable", 0.8 to 0.9 is "very good", and higher than 0.9 is outstanding.

3. RESULTS

In this study, a vibro-tactile feedback-based corset was developed to stimulate humans to be in ideal posture. Initially, various experiments have been performed on corset's textile to investigate whether it provides reasonable comfort properties in terms of wetting time, absorption rate, maximum wetted radius, spreading speed, accumulative one-way transport capacity and overall moisture management capacity. The overall moisture management capacity (OMMC) is the combination of one-way transportation of liquid, moisture absorption and spreading rate inside the fabric [34]. Typically, this value represents the liquid that effectivity transferred from top surface to the bottom [35]. The higher OMMC resulted in higher spreads of liquid. The results showed that fish line fabric has an advantage such that it can prevent any possible textile bulges during human daily activity. The weight per unit area and air permeability values of this fabric are 479.4 g/m^2 and 710.7 L/m^2s, respectively. It was obtained from comfort tests that the selected fabric allows air and moisture to pass through. The overall results suggest that the corset's fabric is reasonable and promise comfort to the user (Table 2).

In the next step, the smart corset efficiency was determined on participants. Typical raw measurements that show the relative angle of motion for a participant is represented in Figure 5a. The red horizontal dashed line refers to the threshold line while the red vertical line shows the separation band between the two cases. The sampling rate of the measurement is 5 Hz. Each case measurements include 18K data points that yield 60 min. It is observed that the number of data points that exceeds the threshold line (16.34º) is found to be higher in case 1 than the second case. The raw measurements were also investigated using the box plots (Figure 5b). In brief, the box plot is a standard method of distribution of data samples corresponding to the features using boxes and whiskers. It represents the inter quartile range of samples while the whiskers refer to a multiple of the first and third quartile of any variable. Any data points that are placed out of this limit are considered as outliers. The inter-quartile values for case 1 and 2 range from 4.92º to 13.30º and 6.11º to 11.11º, respectively (Figure 5b). These results suggest that the range of motion (ROM) due to slouching was decreased in case 2 and indicate that the participant's posture was improved when stimulated by vibro-haptic actuation. The reason for higher outliers encountered in case 2 may have occurred due to participant's sudden motion to correct the posture once they feel the vibro stimuli.

Table 2. Moisture management results of the fish line stretch fabric

Variable	Region	Result	Scale
Wetting Time (s)	Top	4,9687	Fast
	Bottom	4,9167	Fast
Absorption Rate (%/s)	Top	33,7898	Medium
	Bottom	34,6331	Medium
Maximum Wetted Radius (mm)	Top	16,6667	Medium
	Bottom	16,6667	Medium
Spreading Speed (mm/s)	Top	3,0496	Fast
	Bottom	3,1412	Fast
Accumulative One-Way Transport Capacity (%)	Top- Bottom	33,3048	Bad
Overall Moisture Management Capacity (OMMC)	Top- Bottom	0,3394	Very bad

In order to observe and determine all participants' performance, the results are plotted via bar and scatter graphs (Figure 6). The colored circular disk represents the performance and its value as well as the color scale distribution is located at the right of the graph. The performance is computed via $(p_1-p_2)/p_1 \times 100$, while p_1 and p_2 refer to the non-ideal posture number for case 1 and case 2, respectively. The mean non-ideal posture numbers for case 1 and case 2 are 694.66 and 272.25, respectively. In addition, the mean non-ideal posture duration for case 1 and 2 are 147.02 s and 62.18 s, respectively. The highest posture improvement is obtained in the 2nd participant (81.11 %), while the lowest in subject 6 (11.68 %). One possible reason for the low performance of this 6th participant is that he/she may not feel the vibro-haptic stimuli well. The average posture improvement percentage for all participants is 53.65 ± 23.14.

One way ANOVA test assessment was performed for each participant's raw time measurement series to determine the efficiency of vibro-tactile stimuli. The postural angles of all participants in case 1 and 2 are $23.25° \pm 3.44°$ and $20.81° \pm 4.51°$, respectively. The ANOVA test results demonstrate that there is a significant difference between the two cases. ($p<0.05$)

The relative angle measurements obtained for all subjects are combined as two-dimensional vector datasets to investigate the inter quartile range for each case. The size of these datasets is 192K x 2 and the 1st and 2nd dimension refer to case 1 and 2, respectively. The inter quartile relative angle for case 1 is in a range of -3.29° to 5.33°, while for the 2nd case is -2.1° to 2.96° (Figure 7a). It is observed that the range of the box in the 2nd case is lower than the 1st one which indicates that the range of motion due to slouching decreases in case 2.

The subjects' scores were further assessed using receiver operating characteristics (ROC) curves to determine how well all participants' results for two cases could be discriminated against (Figure 7b). The size of the raw measurements for each case is 96Kx2. In addition, the size of the non-ideal posture number and posture duration is 12x2. Note that, the first two dimensions refer to the 1st and 2nd case data. Area under curve (AUC) value obtained for the raw measurements is 0.6531, and critical optimum point is located at (0.2833, 0.4807). These results show that the raw measurements in each case could be separated with a sufficient score. However, acceptable AUC values are obtained for non-ideal posture number (AUC = 0.7083) and non-ideal posture duration (AUC = 0.7361). The overall ROC curves results indicate that once a user is stimulated via vibro-haptic stimuli his/her posture regime changes to a lower slouching range.

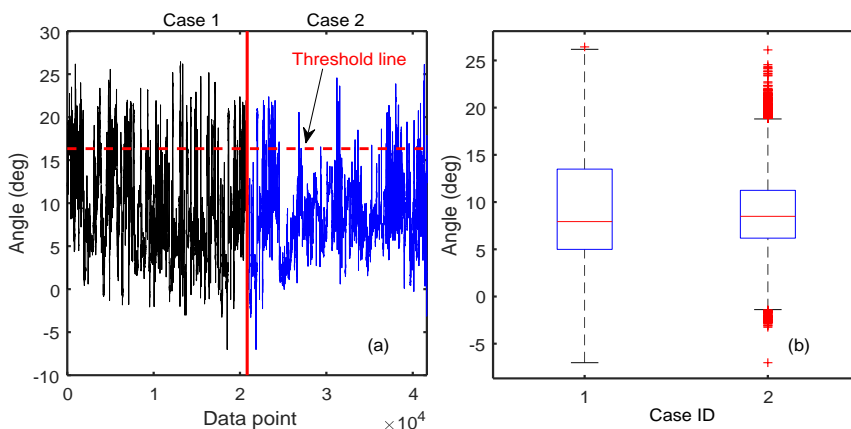**Figure 5.** Typical measurements obtained for a participant. (a) Raw measurements, (b) Box-plot of the raw measurements
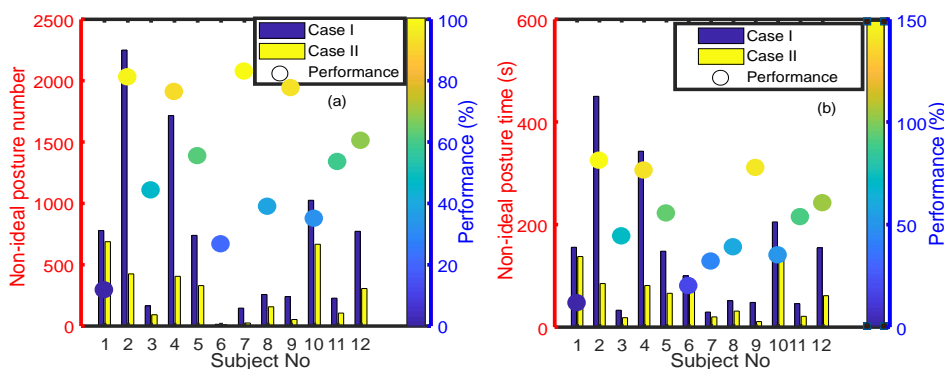
Figure 6. The performance of human subjects for the two cases (a) Non-ideal posture numbers, (b) Non-ideal posture duration
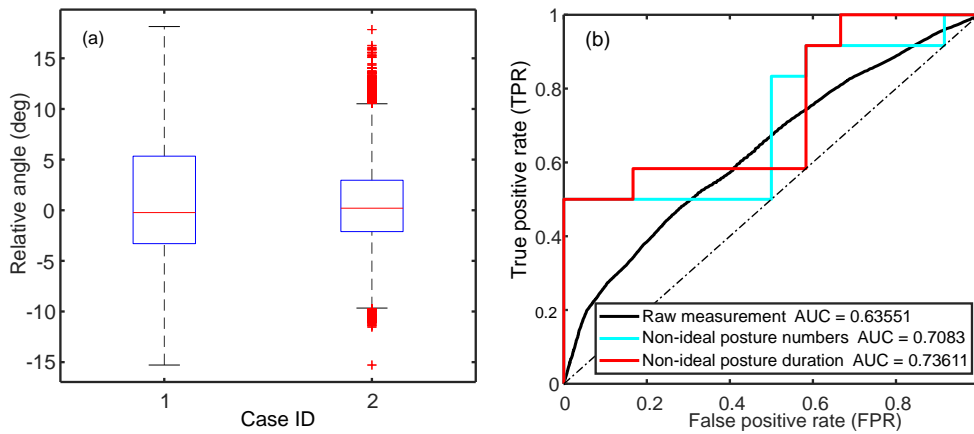
Figure 7. All participants' results. (a) Box-plots, (b) ROC curves

4. DISCUSSION AND CONCLUSION

This study aimed to develop a vibro-haptic corset that stimulates humans to be closely in an ideal posture. Initially, an appropriate fabric textile that provides reasonable properties for the human's comfort was chosen. Then, two orientation sensors and a vibro-haptic actuator were attached to the corset via at T5-T12 and L3 level, respectively. An algorithm was developed to perform some features such as monitoring the posture, calibrating the sensors, storing the raw measurement, determining the critical non-ideal posture threshold angle, acquiring the non-ideal postures as well as the duration, and transferring them over a Wi-Fi connection to the server. Then, two test cases were implemented on 12 participants for the case duration of one hour. In the first case vibro-haptic stimulation was not provided to participants while in the second case it was ensured. The results obtained for participants are given in the previous section. In order to summarize the efficiency of the corset, the participants' results are represented in Figure 8. A paired t-test is implemented on these results to figure out whether there are statistical differences between case 1 and 2. The results show that there is significant statistical difference between

them ($p<0.05$) which indicates that the vibro-haptic corset improves the posture. The improvement is around 53%, and their non-ideal posture duration was significantly decreased showing that their motor learning could be encouraged.

We believe that the use of adjustable velcros fasteners ensure appropriate placement of sensors and actuator to each specific subject's spine anatomy. Furthermore, the instructions provided to participants prior to the tests were sufficient and prevented any misalignments. All of them completed the two case tests successfully. A Likert type survey was arranged for subjective evaluation of the participants to figure out how well they were satisfied by using such a smart corset. Statements and results of this survey are given in Table 3, and they show a favorable response for this corset. The subjective evaluation also showed that the corset's fabric and electronic components are suitable, their size fits on each participant and they feel their self comfort. In addition, 91 % of all subjects agree that it aids to improve posture and they want to use it for their daily life. Their responses are also visualized with bar graphs (Figure 9). In overall, the participants' sentiments are mainly located at "agree" and "strongly agree " choices (73 %).

Figure 8. The results of all participants. (a) Non-ideal posture numbers, (b)Non-ideal posture duration (Whiskers represent the standard errors)

Table 3. User satisfaction survey

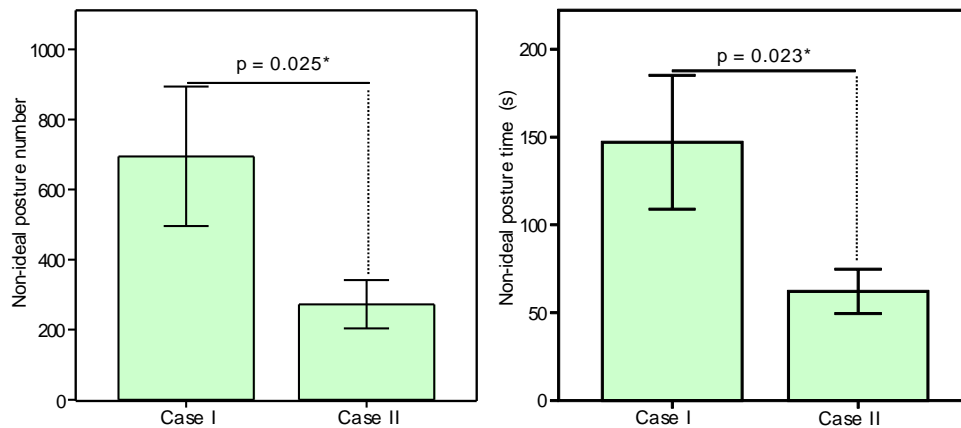| No	Statement	Score
1	The instructions provided with the vibro-corset are easy to understand and adapting it is not difficult.	4.0
2	The corset is comfortable in terms of moisture transmission and air permeability.	4.2
3	The fabric texture does not hurt my skin.	4.1
4	Satisfied with the electronic components	4.2
5	The corset does not cause sweating.	3.9
6	The corset does not cause pain in my body.	4.1
7	The corset and its electronic components neither restrict my movements nor prevent me from performing my daily life activities.	4.3
8	Satisfied with the vibro actuators of the corset	4.0
9	I think that it aids in improving posture stability.	4.2
10	I want to use it in my daily life.	4.3
Response choices: 1) Strongly disagree, 2) Somewhat disagree, 3) Neither agree nor disagree, 4) Somewhat agree, 5) Strongly agree		

The algorithms used in posture curvature recognition could be classified as model and data-based approaches. The model-based approach is generally implemented by building a geometrical model for determining the spine's posture. Once the geometrical model based on anatomical spine's curvature is established it is updated using measurements from sensors that are attached to humans' skin, garment or corset. Implementing such a model-based approach is simple and does not cause CPU power to consume the battery fast. On the other hand, a data-based approach is performed mostly using pattern recognition and machine learning techniques [36]. It uses direct raw data of measurements, and the algorithm is established using statistical techniques. In primary investigation, we also used this approach to test null hypothesis. The null hypothesis can be considered as; if H_0: $P(\varepsilon_x) = P(\varepsilon_y)$, "ideal posture" against the alternative hypothesis, if H_1: $P(\varepsilon_x) \neq P(\varepsilon_y)$, "non ideal posture". ε_x and ε_y refer to the reference healthy posture and testing posture, respectively. The non-ideal posture could be detected using F-statistics for 99 % confidence interval. However, large datasets and higher computational power are required to process them by using a data-based approach that causes higher consumption of a battery. Hence, we preferred to use the model-based approach. However, we expect that the advancements in battery and processor technology will allow us to embed powerful machine learning and pattern recognition

approaches in these portable devices to monitor and detect the posture anomalies.

Currently, radiological images that are constructed using X-ray, computer tomography (CT), and magnetic resonance imaging are key standard devices for evaluation of posture curvature [37]. However, expensive lab-based instruments may not effectively monitor the user's posture for daily conditions. Recently, wearable technologies have been proposed and some of them commercially available in the market [29]. These typical devices can monitor one's posture, stimulate him/her in non-ideal posture. However, the algorithms embedded in them are not open to the public due to commercialization. In addition, although many studies reported in history belong to the sitting posture, the ideal sitting posture has not been defined yet [4]. Therefore, the lack of a standardized postural metrics method is challenging. Furthermore, the majority of studies reported in literature have been focused on the postural device placed on the garment, while its ergonomic features have not been investigated [21,28]. In addition, many of commercial postural devices include a single sensor node, and it is not clear whether a single node has a capability to measure relative joint angle. In this study, we characterized the corset's fabric and developed an algorithm that could detect the relative range of motion of a joint, store and transfer the data over a Wi-Fi connection to the server. The microcomputer, sensors and haptic actuator have been enclosed in 3D printed boxes and attached to the corset via velcros. The corset is washable for reuse by detaching the components.
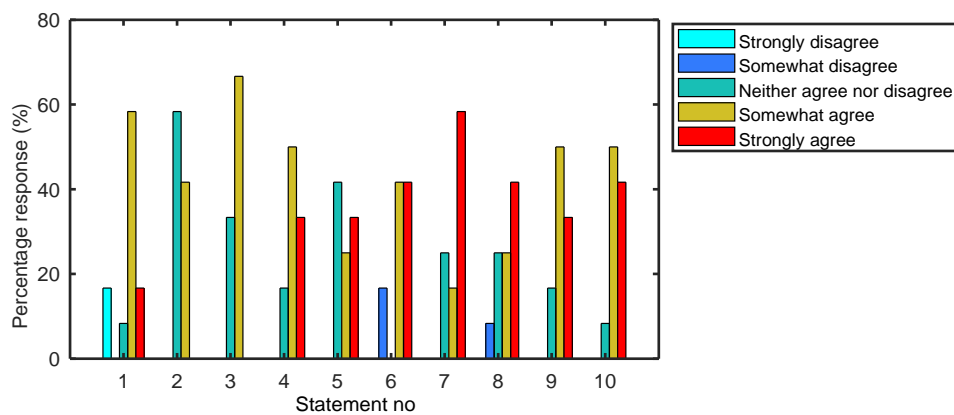

Figure 9. Summary of subjects percentage responses in satisfaction survey

Recently, technological advances have empowered us to design and create powerful wearable tools not just only for patients but also for regular healthy persons. Professional healthcare may be overwhelmed when their patients increase, or such as in a global pandemic, these wearable devices could be brought to the table. It is demonstrated in methodology that the vibro-haptic corset has a capability to transform the user's data to the server. It is expected that a healthcare professional at server side can monitor the user's data and allow preventive care and manage ongoing conditions. It is also expected that the vibro-haptic corset may be used as a supporting tool in the healthcare system and to reduce the overwhelm in clinics.

Although the participants' results indicate that the vibro-haptic corset significantly improves their posture, there are some limitations regarding this study. First, the small population and age demographic are useful for determining its performance. Hence, the population of participants should be increased to figure out how the vibro-haptic stimuli could change the cognitive of participants across age and body index. Second, although the algorithm embedded in corset's device is programmed for sitting posture, it should be expanded to include all daily activities. The current version of the corset monitors a single flexion-extension direction in the sagittal plane. However, it should also include multi axis direction such as left-right lateral bending and twisting along the axis of spine. Future studies should focus on expanding the measurement capabilities.

The overall conclusion is that the vibro-haptic corset effectively provides postural improvements and could be deployed as a promising trainer. To further verify its feasibility, future efforts should be directed to include multi nodes in a network for a large population.

Acknowledgement

REFERENCES

1. Woolf AD, Pfleger B. 2003. Burden of major musculoskeletal conditions. *Bulletin of the World Health Organization* 81, 646-656.

2. O'Sullivan K, O'Sullivan P. 2012. What do physiotherapists consider to be the best sitting spinal posture? *Manual Therapy* 17, 432-437.

3. Bullock MI, Bullock-Saxton JE. 2000. *Control of low back in the workplace using an ergonomic approach*. In: Twomey LT, Taylor JR, editors. Physical therapy of the low back. 3rd ed. New York: Churchill Livingstone, 297–326.

4. Claus AP, Hides JA, Moseley GL, Hodges PW. 2009. Is 'ideal' sitting posture real?: Measurement of spinal curves in four sitting postures. *Manual Therapy* 14, 404–408.

5. Jarvik JG, Hollingworth W, Heagerty PJ, Haynor DR, Boyko EJ, Deyo RA. 2005. Three-year incidence of low back pain in an initially asymptomatic cohort: clinical and imaging risk factors. *Spine* 30(13), 1541-8.

6. Moseley GL. 2007. Reconceptualising pain according to modern pain science. *Physical Therapy Reviews* 12(3), 169-178.

7. Reichborn-Kjennerud T, Stoltenberg C, Tambs K, Roysamb E, Kringlen E, Torgersen S, Harris JR. 2002. Back neck pain and symptoms of anxiety and depression: a population- based twin study. *Psychological Medicine* 32(06), 1009-20.

8. Ballardini G, Florio V, Canessa A, Carlini G, Morasso P, Casadio M. 2020. Vibrotactile feedback for improving standing balance. *Frontiers in Bioengineering and Biotechnology* 8, 94.

9. Nazari J, Pope MH, Graveling RA. 2012. Reality about migration of the nucleus pulposus within the intervertebral disc with changing postures. *Clinical Biomechanics* 27(3), 213–217.

10. Castanharo R, Duarte M, McGill S. 2014. Corrective sitting strategies: An examination of muscle activity and spine loading. *Journal of Electromyography and Kinesiology* 24, 114–119.

11. Womersley L, May S. 2006. Sitting posture of subjects with postural backache. *Journal of Manipulative and Physiological Therapeutics* 29(3), 213-218.

12. Adams M, Dolan P, Hutton WC. 1988. The lumbar spine in backward bending. *Spine* 13, 1019–1026.

13. Baranda PS, Cejudo A, Martínez-Romero MT, Aparicio-Sarmiento A, Rodríguez-Ferrán, Collazo – Dieguez M, Hurtado-Aviles J, Andujar P, Santonja-Medina F. 2020. Sitting posture, sagittal spinal curvatures and back pain in 8 to 12-year-old children from the region of Murcia (Spain): ISQUIOS Programme, *International Journal of Environmental Research and Public Health* 17, 2578.

14. Pynt J, Mackey MG, Higgs J. 2008. Kyphosed seated postures: extending concepts of postural health beyond the office. *Journal of Occupational Rehabilitation* 18(1), 35-45.

15. Sprague RB. 2001. Differential assessment and mobilisation of the cervical and thoracic spine. In: Donatelli R, Wooden MJ, editors. *Orthopaedic physical therapy*. 3rd ed. New York: Churchill Livingstone, 108–43.

16. Saur PMM, Ensink FBM, Frese K, Seeger D. 1996, Hildebrandt J. Lumbar range of motion: reliability and validity of the inclinometer technique in the clinical measurement of trunk flexibility. *Spine* 21, 1332–38.

17. Wu H, Chu CC, He C, Wong M. 2020. Assessment of the plane of maximum curvature for patients with adolescent idiopathic scoliosis via computed tomography. *Prosthetics and Orthotics International* 44(5), 1–7.

18. Brulin D, Benezeth Y, Courtial E. 2012. Posture recognition based on Fuzzy logic for home monitoring of the elderly. *IEEE Transactions on Information Technology in Biomedicine* 16(5), 974-82.

19. Wong WY, Wong MS. 2008. Trunk posture monitoring with inertial sensors. *European Spine Journal* 17, 743–753.

20. Poredoš P, Čelan D, Možina J, Jezeršek M. 2015. Determination of the human spine curve based on laser triangulation, *BMC Medical Imaging* 15, 2.

21. Barone VJ, Yuen MC, Kramer-Bottiglio R, Sienko KH. 2019. Sensory garments with vibrotactile feedback for monitoring and informing seated posture, *2nd IEEE International Conference on Soft Robotics* 391-397.

22. Grosse-Wentrup M, Mattia D, Oweiss K. 2011. Using brain computer interface to induce neural plasticity and restore function. *Journal of Neural Engineering* Apr; 8(2):025004.

23. Franco C, Fleury A, Guméry PY, Diot B. 2012. Demongeot J, and Vuillerme N. iBalance-ABF: a smartphone-based audio-biofeedback balance system. *IEEE Transac. Biomed. Eng.* 60, 211–215.

24. Pekedis M, Mascarenas D, Turan G, Ercan E, Farrar C.R, Yildiz H. 2015. Structural health monitoring for bolt loosening via a non-invasive vibro-haptics human-machine cooperative interface. *Smart Materials and Structures* 24, 085018.

25. Xu J, Bao T, Lee UH, Kinnaird C, Carender WJ, Huang Y, Sienko KH, Shull PB. 2017. Configurable, wearable sensing and vibrotactile feedback system for real-time postural balance and gait training: proof-of-concept. *Journal of NeuroEngineering and Rehabilitation* 14, 1–10.

26. Zhang Y, Morrell JB. 2010. A vibrotactile feedback approach to posture guidance. *IEEE Haptics Symposium*, 351–358.

27. Dunne LE, Walsh P, Hermann S, Smyth B, Caulfield B. 2008. Wearable monitoring of seated spinal posture. *IEEE Transactions on Biomedical Circuits and Systems* 2, 97–105.

28. Voinea GD, Butnariu S, Mogan G. 2017. Measurement and geometric modelling of human spine posture for medical rehabilitation purposes using a wearable monitoring system based on inertial sensors. *Sensors* 17(1), 3.

29. Yoong KMY, Perring JJ, Mobbs RJ. 2019. Commercial postural devices: A review. *Sensors* 19(23), 5128.

30. AATCC 195. Liquid moisture management properties of textile fabrics.

31. ASTM D 737 Test method for air permeability of textile fabrics.

32. ISO 3801. Textiles-Woven fabrics-Determination of mass per unit length and mass per unit area.

33. Kolessar D, Stollsteimer GT, Betz RR. 1996. The value of the measurement from T5 to T12 as a screening tool in detecting abnormal kyphosis. *Journal of Spinal Disorders* 9(3), 220-222.

34. Özdil N, Süpüren G, Özçelik G, Pruchova J. 2009. A study on the moisture transport properties of the cotton knitted fabrics in single jersey structure. *Tekstil ve Konfeksiyon* 19(3), 218-223.

35. Ünal ZB, Acar E, Yildirim F. 2015. Evaluating performance characteristics of lining fabrics used for children dresses. *Tekstil ve Konfeksiyon* 25(4), 323-328.

36. Pekedis M. 2021. Detection of multiple bolt loosening via data based statistical pattern recognition techniques. *Journal of the Faculty of Engineering and Architecture of Gazi University* 36(4), 1993-2010.

37. Shah VA, Casadio M, Scheidt RA, Mrotek LA. 2019. Spatial and temporal influences on discrimination of vibrotactile stimuli on the arm. *Experimental Brain Research* 237, 2075–2086.

Investigation of Performance Properties of Denim Fabrics Containing Cotton/Sustans® Blend Rotor Yarn

Muhittin Özkan[1] 0000-0001-8749-5605
Pınar Duru Baykal[1] 0000-0003-1461-2203
İlkan Özkan[2] 0000-0003-1006-895X

[1]Çukurova University, Engineering Faculty, Department of Textile Engineering, Adana, Türkiye
[2]Adana Alparslan Türkeş Science and Technology University, Engineering Faculty, Department of Materials Science and Engineering, Adana, Türkiye

Corresponding Author: Pınar Duru Baykal, pduru@cu.edu.tr, pdbaykal@gmail.com

ABSTRACT

It is common to use open-end rotor yarn in the production of denim fabric, which is preferred by people of all ages and social status due to its durability and comfort. Recently, the demand for stretch denim fabrics that can take the body's shape due to the elastic fibers in its structure has been increasing. However, producing elastane-containing yarns in the rotor spinning system is not as practical as ring spinning. For this reason, this study aimed to use the staple Sustans® fibers with high elasticity in the rotor spinning system together with cotton fibers and reflect the good elasticity and elongation properties of Sustans® fibers to the rotor yarns and denim fabrics. In the study, the staple Sustans® fibers based on PTT (Polytrimethylene Terephthalate) were spun with cotton fibers in the rotor spinning system. Then denim fabrics were produced using these yarns in the weft. Later, strength (breaking and tear), dimensional stability (dimensional change after washing, fabric elasticity and growth), abrasion resistance and pilling tests were applied to the produced denim fabrics. Thus, the effects of using Sustans® fibers on the strength, dimensional stability, abrasion and pilling properties of denim fabrics were analyzed. As a result of the study, the dimensional change and growth values after washing were developed by using Sustans®. Although good dimensional stability was observed in the samples, the degree of elasticity was lower than expected. The use of Sustans® at rates of 50% and above improved the pilling values of the fabrics. In addition, it has been determined that the use of Sustans® in terms of abrasion resistance has a more positive effect at the end of long wear periods.

1. INTRODUCTION

It is known that natural fibers are insufficient to meet the increasing demand, and this situation causes an increase in the consumption of synthetic fibers. Compared to natural fibers, it is predicted that the production of synthetic fibers will increase even more in the future. Recently released world fiber consumption data supported that the production of synthetic fibers will increase. The synthetic polymer industry is largely based on fossil fuels. The ability of petroleum-based plastics to survive in nature for many years brings environmental pollution and sustainability concerns. Some studies stated that 9 million tons of plastic waste reach oceans annually [1]. Regenerated fibers, in which relatively natural resources are used in their production, are not likely to be an alternative to synthetic fibers in terms of production amounts. The increase in synthetic fiber production is unavoidable due to factors such as production factors, costs, and fiber properties. In this case, it is essential to prefer sustainable resources in the polymer industry [2].

To cite this article: Özkan M, Duru Baykal P, Özkan İ. 2022. Investigation of performance properties of denim fabrics containing cotton/sustans® blend rotor yarn. *Tekstil ve Konfeksiyon* 32(4), 314-326.

The textile industry emits 1.2 billion tons of CO_2 equivalent of harmful gas per year. During the production processes of Sorona®, 30% less energy is consumed than Nylon 6 and 40% less than Nylon 6.6. Besides, 63% and 56% lower gas emitted than Nylon 6 and Nylon 6.6, respectively. 37% of the Sorona® polymer, introduced as an example of a more sustainable synthetic polymer by DuPont company, is produced from vegetable-based renewable natural resources such as corn. Therefore, it is shown as an example of more sustainable synthetic polymer production that causes lower greenhouse gas emissions [3, 4, 5, 6].

PTT forms the phthalates branch of aromatic polyesters together with Polyethylene Terephthalate and Polybutylene Terephthalate. PTT polymer is produced with the polycondensation reaction of pure terephthalic acid or dimethyl terephthalate with 1,3 propanediol (PDO). This polymer was firstly synthesized in 1941, and its commercialization was realized in 1990 by Shell Chemicals using the ethylene oxide hydroformylation method [4, 7, 8]. DuPont company produced its own PTT with the Sorona brand using PDO obtained by fermentation from corn starch [4]. PTT fibers have favorable properties such as good elasticity and dimensional stability, easy cleaning, easy dyeing, good color fastness, low static electricity, and soft-touch compared to most other fibers. Sustans® is the staple fiber produced by Haixing company using Sorona® polymer [9].

The denim fabric has become a popular cultural item in recent years. Because it is known in all societies and it is used in many areas such as upholstery, home textile products, and advertising products, especially in the production of clothes. Denim fabrics are expressed in the world with names such as "jeans", "blue-jeans", "jeans wear" and "sportswear".

Classic denim fabrics are produced from high twisted and strong cotton yarns. These fabrics are structurally dense, tough, and durable, and the yarns used in the warp are indigo dyed. However, with the effect of changing fashion trends and technological possibility, denim fabrics are produced in different ways, such as weft dyed denim fabrics or dyed with other processes. Synthetic fibers or cotton-synthetic blend yarns are frequently used in denim production [10, 11]. Increasing usage area changes the features expected from denim fabrics. For example, denim trousers are used frequently in different seasons and weather conditions.

Consequently; many properties such as strength, pilling, dimensional stability, abrasion resistance, and clothing comfort are expected to be good. For this reason, it is quite common to use fibers different from cotton and stretch yarns containing elastane in denim fabrics today. Elastic yarn requirement in denim fabrics is provided with multi-component core yarns. Core components except elastane are generally used to reduce the growth [12].

The literature review has shown a gap regarding the production of yarn and fabric from staple PTT fibers. Most of the studies on PTT fibers are related to polymer production, pure or bicomponent filament yarn production, and elasticity properties of these yarns [4, 7, 13, 14, 15, 16, 17, 18, 19]. Previous studies on the subject of research are as follows.

Zhao et al. investigated the factors affecting the return of fabrics produced from PTT filaments to their original shape after wrinkle. For this purpose, three different samples having different densities, including 8.3 tex PTT filament yarns, were produced. The researchers stated that the temperature had little effect on wrinkle recovery because of the fabric's tight structure and the filament crystallization rate [20].

Lou et al. studied the elasticity of woven fabrics containing PTT / PET bicomponent filament fibers. In the study, PET, PET/PTT-PET bicomponent, and PTT / PET bicomponent yarns were used as weft yarn in woven fabric. Researchers investigated the effects of fiber ratio, twist level, weft density, and weave type. It was noted that increasing PTT / PET fibers' ratio up to 66.7% increases elasticity property significantly; besides, increasing twist level prevented the curling in filaments, thereby considerably affecting the elasticity of fabrics [21].

Yan et al., examined swimwear fabrics, including Sorona-based fibers. The study stated that PET / Spandex and PA / Spandex yarns were mainly used in swimwear fabrics, but these yarns had defects such as easy deformation and short life. As an alternative to spandex-containing fabrics, swimwear fabrics were produced from PA / PTT / Spandex yarns and compared. According to research, the elasticity, elastic recovery, and plastic deformation properties of the new fabric structure were better than the commercialized fabrics. Besides, it had excellent explosion resistance and lower water absorbency [22].

Wang et al. investigated the elastic elongation properties of PTT / PET bicomponent fibers in their study. The study examined the effect of different nozzle structures and PTT/PET ratios on the elasticity properties. The curving degree of samples was predicted depending on the fiber cross-section and properties. As a result, they found that with the increase in PTT ratio in the existing structure, the elasticity feature also increased, but the nozzle types did not significantly affect elasticity. They also revealed a positive correlation between curving degree and elasticity [15].

Zhao et al., investigated the use of PTT / PET bi-component fibers instead of PU / PA to produce seamless knitted garments. As a result, they have shown that PTT / PET bicomponent fibers exhibit high elongation and elastic recovery. The researchers stated that the use of PTT / PET yarns provided more controlled and efficient knitting. Besides, the dimensional stability and anti-wrinkle properties of fabrics produced from PTT / PET bicomponent yarns were better than PU / PA [23].

Jin et al., examined the breaking elongation, elasticity, wrinkle recovery, pilling resistance, water absorption, and air permeability of Sorona/Cotton blended seamless knitted fabrics. As a result of the research, it was emphasized that an increase in Sorona fiber ratio improved the elongation, elasticity, crease recovery and pilling resistance properties of knitted samples [24].

Jianbo et al. Investigated the functional properties of fabrics knitted with modal / cashmere / Sustans® fiber blended spun yarn with antibacterial properties. As a result of the research, it was noted that the fabrics produced had positive antibacterial properties, as well as good pilling resistance and warm keeping properties [25].

Özkan et al. aimed to spin Sustans® fibers together with cotton in an open-end (OE) rotor spinning system. In this way, it is desired to transfer the favorable properties of Sustans® fibers such as good elasticity, good dimensional stability, low static electrification, and soft hand to the staple yarn structure. Researchers successfully produced OE yarns using Sustans®/Cotton blends in the open-end rotor system and were stated the 50/50% blend ratio as the optimum value for the process [9].

Recently, the demand for stretch denim fabrics, containing elastic yarns, that can stretch and take the body shape easily has been increasing. The open-end spinning technique is a highly productive method, and OE yarns are frequently used in denim fabric production. For this reason, this study aimed to spin the Sustans® fibers with high elasticity in the rotor spinning system together with cotton and thus reflect the good elasticity and elongation properties of Sustans® fibers to the rotor yarns and denim fabrics. With this study, it is also aimed to contribute to the lack of literature on yarn and fabric production with staple PTT fibers. In this context, the effects of the positive properties of PTT fibers such as elasticity and dimensional stability on yarn and fabric structure when these fibers are in staple form were investigated. In the study, the staple Sustans® fibers based on PTT (Polytrimethylene Terephthalate) were spun with cotton in the rotor spinning system. Then denim fabric was produced using these yarns in the weft. Breaking strength and elongation, tear strength, dimensional stability (dimensional change after washing, fabric elasticity and growth), abrasion resistance and pilling tests were applied

to the produced denim fabrics. According to the results, the effects of Sustans® fibers in weft on the properties of denim fabrics were analyzed statistically and compared.

2. MATERIAL AND METHOD

2.1. Material

In this study, Sustans® fibers and American cotton were used as raw materials. Cotton fiber properties were determined with the Uster HVI Spectrum (High Volume Instrument). The average measurement results of cotton fiber provided from nine different bales. The Sorona® polymer-based Sustans® fibres supplied by Chinese Haixing Material Technology Company. The fineness and length data of Sustans® fibers were obtained from the manufacturer. The strength and elongation tests were carried out using a 2.5 N capacity load cell, 10 mm jaw distance and 50 mm / min speed by Instron 5564 universal tensile tester. Tests results represented as the average of 20 tests. Cotton and Sustans® fiber properties are given in Table 1 [9].

Table 1. Cotton and Sustans® fiber properties

Properties	Results	
	Mean	%CV
Sustans® (SU)		
Linear Density (dtex)	2.00	-
Length (mm)	38.00	-
Mean Breaking Strength (cN/tex)	31.80	1.65
Mean Breaking Elongation (%)	35.73	24.96
Cotton (CO)		
Spinning Consistency Index)	136.00	6.69
Fiber Fineness (Micronaire)	4.01	5.08
Maturity	0.87	1.63
Length (mm)	29.26	1.87
Uniformity (%)	82.28	1.70
Short Fiber Index (shorter than 12.7 mm) (%)	8.20	6.57
Strength (cN/tex)	30.87	4.70
Elongation (%)	7.27	3.51
Moisture (%)	7.30	3.99
Reflectance Degree	76.16	1.46
Yellowness Degree (+b)	7.37	8.00
Color Grade (C Grade)	41-1	-
Trash Count	40.22	32.08

Table 2. Yarn production stages and machines

Production Stages	Machine Brand-Model-Year		Process Output
Bale Opener-Mixer	Rieter B 34 - 1989		Blended fiber
Fine Opener-Cleaner	Rieter B 5/5 ERM - 1989		Homogeneous blend
Carding	Trützschler DK 760 - 1995		Sliver - Ne 0.13
Drawing	Rieter RSB D50 - 2017		Sliver - Ne 0.11
Drawing	Rieter RSB 51 - 1991		Sliver - Ne 0.11
	Saurer Schlafhorst Autocoro 9- 2017		
	Rotor Type / Diameter	T 640 BD/40 mm	
	Navel Type	K 4-A	
Open-End Rotor Spinning	Torquestop Type	30-0G (Green)	Yarn - Ne 8,25
	Opening Roller Type	B 174DN	(71.60 tex)
	Twist Coefficient (αe)	4,5	
	Rotor speed (rev / min)	60.000	
	Opener (rev / min)	7000	

2.2. Method

In the research, Cotton / Sustans® blend yarns and 100% cotton yarn were produced with the same production parameters. In blended yarns, the cotton ratios were 70%, 60%, 50%, 40% and 30%, respectively. The number of the produced yarns was set to Ne 8.25 (71.6 tex).

The first fiber blend was obtained by feeding fiber bales in pieces to the bale opener. The following steps were carried in the yarn production process; bale opening, blending, opening-cleaning, carding, the first passage of drawing, the second passage of drawing and spinning. In the production, the homogeneity of blending was increased in the fine opener and cleaner machine. The carded slivers in the mentioned blending ratios were passed through two passage drawing processes. The obtained slivers were spun to yarn in an open-end rotor spinning frame. Four bobbins of yarn were produced for each blending ratio. Yarn production stages, used machines and spinning parameters are indicated in Table 2 [9].

Yarn breaking strength and elongation tests were performed in Uster Tensorapid 3 V7.0 device according to the ISO 2062: 2009 standard. In the measurements, ten tests were applied to four bobbins from each blending ratio. Denim fabrics were produced by the Dornier AWSE 4 / E D model air-jet weaving machine. Ne 8.25 rotor warp yarns, which are rope dyed in the classical denim production style, are used in the fabrics. Weaving was carried out sequentially on the same machine with 10 m lengths of warps. Weaving production parameters are listed in Table 3.

Table 3. Weaving production parameters

Parameters	Values
Comb number	68/4
Comb width	175 cm
Total number of warps	4760 pcs
Machine speed	520 rpm
Warp density	27 pcs / cm
Weft density	17 pcs / cm
Weave type	Twill - 3/1 Z
The raw material of warp yarn	%100 Cotton
Warp yarn number	Ne 8.25 (71.60 tex)
Warp yarn type	OE rotor

Burning, washing, pre-drying and sanforizing processes were applied to the woven fabrics as finishing processes. These processes have been implemented in a single machine line, which is a combination of different machine parts and provides continuous operation. Besides, all fabrics were treated as one piece under the same conditions. The burning process was applied in the Osthoff brand machine with 90 ° burner angle, 30 mm burner distance, 9 bar burner pressure and 35 m / min processing speed. Acetic acid was used as an acidity regulator to provide a pH range of 5-5.5 in the washing process. Then, the fabrics were pre-dried by passing through drums at 110 °C. Finally, sanforizing is applied with the felt-blanket system at 35 m / min speed.

Breaking strength and elongation (ISO 13934-1: 2013), tear strength (ISO 13937-1: 2000), dimensional change after washing (ISO 3759: 2011, ISO 6330: 2012), elasticity and growth (ASTM D 3107-07: 2015) tests were applied to fabric samples. Elasticity and growth tests were only applied in the direction of the fabric showing elastic properties. Elasticity and growth tests were conducted to fabrics both in finished form and after washing at 60°C. The dimensional change after the washing was tested at 40 °C and 60 °C separately. Washings at 40°C and 60°C were carried out according to Table B.1 4N and 6N methods of the related standard. Fabric production parameters are kept constant in all blending ratios. Density (EN 1049-2:1993), weight (ISO 3801:1977), and finished product width (EN 1773: 1996) tests were also performed to determine the effect of different weft yarn types on these properties.

Both the abrasion resistance and pilling tests were performed on the James H. Heal brand and Nu-Martindale model abrasion and pilling tester. The tests were applied on the reverse side of the fabrics because the produced Cotton/Sustans® blend yarns were used in the weft of the fabrics and the weft density was higher on the reverse side of the fabrics. Abrasion resistance tests were applied on the basis of ISO 12947-3: 1998 standard method. The fabrics were abraded up to 25000 cycles using 9 kPa pressure and woolen abrasion fabric. The loss of mass was determined by weighing at every 5000 cycles. Pilling tests were applied according to the ISO 12945-2: 2000 standard method. The test samples were evaluated at the end of 125, 250, 500, 1000, 2000, 5000 and 7000 cycles according to the EMPA SN 198525 W3 standard photograph series. VeriVide brand pilling evaluation cabinet was used for visual evaluation. For both methods, 3 samples from each fabric type were tested. Test results of all samples for pilling tests are indicated. In terms of abrasion resistance, the average of 3 samples belonging to each fabric type is reflected in the results.

Pilling test results are evaluated by visual scale and are not numerical data. Therefore, statistical analysis was not applied for the pilling test results, the results of all test samples were stated and interpreted. Considering that the use of Sustans® will affect the fabric stiffness and also the fabric stiffness will affect the abrasion resistance, the circular stiffness test was also performed on the fabrics according to the ASTM D 4032-94: 2001 standard.

In statistical analysis, firstly, Kolmogorov-Smirnov (K-S) normality analysis was applied. The relationship between Sustans® ratio and fabric properties was examined with Pearson correlation analysis for the normally distributed data, and Spearman correlation analysis was used for the other data sets. According to the correlation analysis, the level of significant relationships between fiber blend ratio and data sets was defined according to the power of the coefficients [26]. Analysis of variance (ANOVA) was applied to the normally distributed data, and the Kruskal Wallis test [27, 28] was used for the other data sets.

3. RESULTS AND DISCUSSION

According to the Kolmogorov-Smirnov (K-S) test, the data except for the density, warp tear strength of the fabrics, and the growth after washing at 60ºC showed normal distribution. Since all the growth test results in the finished state are 0.4%, statistical analysis could not be done. The correlation analysis results between Sustans® ratio and fabric properties are given in Table 4.

ANOVA test results of normally distributed data are given in Table 5, and Kruskal Wallis test results of data that do not show normal distribution are given in Table 6.

3.1. Finished Fabric Width, Weight and Densities

It is seen in Tables 5 and 6 that the weft yarn blending ratio has a statistically significant effect on the weight, width and warp density of finished fabric (p <0.05). However, there was no significant effect of blending ratio on weft density. The width of 100% cotton fabric is greater than the width of all fabrics containing Sustans®, and it differs statistically from them (Figure 1). Fabrics containing 40%, 50% and 60% Sustans® yarns formed a separate group from fabrics containing 30% and 70% Sustans® yarns. Fabrics containing 40%, 50% and 60% Sustans® yarns have the lowest finished widths. Besides, these three fabrics had the highest warp density values (Figure 1). As a result, while there was no difference between weft densities according to blending ratio, a weak correlation and statistically significant effect was found between warp densities and Sustans® ratio. A statistically significant decrease in the width of the finished fabric was observed with the use of sustans fibers in the weft. The reduction in fabric width has increased the warp density.

Parallel to the increase in warp density, an increase was observed in fabric weight (Figure 2).

Table 4. Results of correlation test between Sustans® ratio and fabric properties

Fabric Properties	Correlation Coefficient	Significance Value (p)
Pearson Correlation Results		
Weight	0.408*	**0.025**
Finished Width	-0.843**	**0.000**
Tensile Strength (Weft Direction)	-0.009	0.967
Tensile Strength (Warp Direction)	0.348	0.096
Elongation at Break (Weft Direction)	0.982**	**0.000**
Elongation at Break (Warp Direction)	-0.065	0.763
Tear Strength (Weft Direction)	0.085	0.695
Dimensional Change (Weft Direction-40ºC)	-0.948**	**0.000**
Dimensional Change(Weft Direction-60ºC)	-0.802**	**0.000**
Dimensional Change (Warp Direction-40ºC)	0.549*	**0.018**
Dimensional Change (Warp Direction-60ºC)	0.326	0.187
Elasticity (Finished)	-0.651**	**0.003**
Elasticity (60ºC)	-0.873**	**0.000**
Circular Stiffness	0,215	0,314
Abrasion-5000 Cycle	-0,062	0,805
Abrasion-10000 Cycle	-0,202	0,421
Abrasion-15000 Cycle	-0,343	0,164
Abrasion-20000 Cycle	-0,436	0,070
Abrasion-25000 Cycle	**-0,469***	**0,050**
Spearman Correlation Results		
Weft Density	0.054	0.775
Warp Density	0.323	0.081
Tear Strength (Warp Direction)	0.622**	**0.001**
Growth (60ºC)	-0.469*	**0.049**

* Correlation is significant at 0.05 level. ** Correlation is significant at 0.01 level.

Table 5. ANOVA test results

Fabric Properties	Sum of Squares	Degree of Freedom	Mean Squares	F Value	Significance Value (p)
Weight	396.87	29	43.21	5.74	**0.001**
Finished Width	77.19	29	15.40	1885.50	**0.000**
Breaking Strength Weft Direction	41975.03	29	5565.24	9.44	**0.000**
Breaking Strength Warp Direction	57051.89	29	4975.54	3.71	**0.012**
Breaking Elongation Weft Direction	251.89	29	49.58	299.45	**0.000**
Breaking Elongation Warp Direction	16.71	29	2.38	11.85	**0.000**
Tear Strength Weft Direction	27.98	29	0.78	0.78	0.575
Dimensional Change- Weft Direction (40º C)	9.53	17	1.81	43.32	**0.000**
Dimensional Change Weft Direction (60º C)	6.72	17	1.00	6.90	**0.003**
Dimensional Change Warp Direction (40º C)	4.91	17	0.70	6.05	**0.005**
Dimensional Change Warp Direction (60º C)	3.22	17	0.47	6.72	**0.003**
Elasticity Finished	2.10	17	0.33	9.40	**0.001**
Elasticity (60ºC)	3.16	17	0.50	9.47	**0.001**
Circular Stiffness	5402479	29	449843.71	3.42	**0.018**
Abrasion-5000 Cycle	0.97	17	0.05	0.88	0.522
Abrasion-10000 Cycle	1.20	17	0.04	0.43	0.821
Abrasion-15000 Cycle	1.86	17	0.06	0.42	0.827
Abrasion-20000 Cycle	3.06	17	0.13	0.64	0.671
Abrasion-25000 Cycle	5.51	17	0.26	0.76	0.595

Table 6. Kruskal Wallis test results

Fiber Blending Ratio	Weft Density		Warp Density		Warp direction tear strength		Growth (60ºC)	
	Mean Rank	Sig. Value (p)	Mean Rank	Sig. Value (p)	Mean Rank	Sig. Value (p)	Mean Rank	Sig. Value (p)
%100 CO	12.50		4.70		14.30		13.50	
%70 CO %30 SU	18.10		14.90		7.50		10.50	
%60 CO %40 SU	18.10		17.30		6.40		7.50	
%50 CO %50 SU	13.10	0.572	25.60	**0.001**	18.40	**0.001**	10.50	0.299
%40 CO %60 SU	13.10		19.70		18.40		7.50	
%30 CO %70 SU	18.10		10.80		28.00		7.50	

(a)

(b)

Figure 1. a) Fabric width - blend ratio graph b) Yarn density - blend ratio graphs
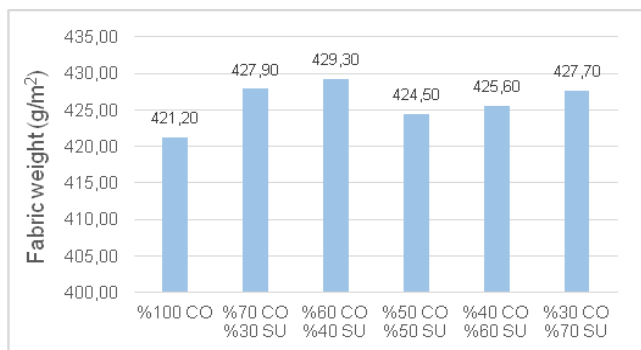
Figure 2. Fabric weight - blend ratio graph

3.2. Fabric Tensile Strength and Elongation

As a result of the ANOVA test (Table 5), it was seen that the blending ratio had a statistically significant effect on the tensile strength and elongation in both directions (p <0.05). The average of the fabric test results is given in Figure 3, and the strength-elongation graphs of the weft yarns are shown in Figure 4 [9]. Although the fabrics have the same warp yarns, it has been determined that the differences in warp strength and elongation are related to the warp density. Similar trends are seen in warp density and warp direction strength graphs.
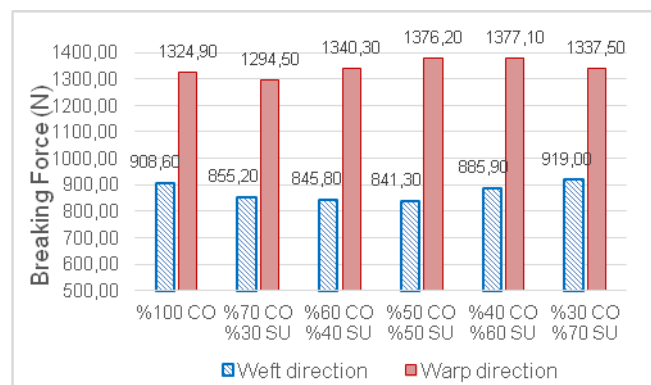
(a)
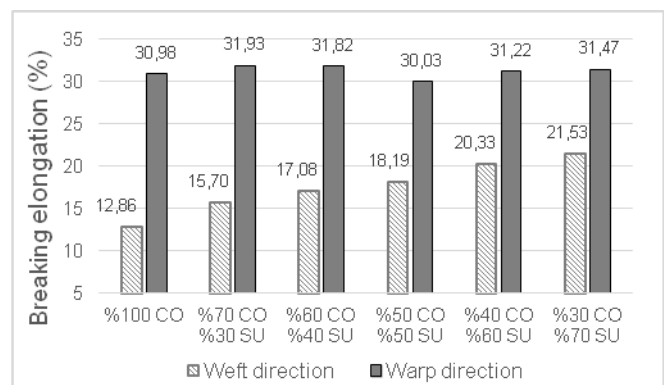
(b)

Figure 3. a) Fabric breaking strength graph b) Fabric breaking elongation graph

As shown in Figure 4-a, with the use of Sustans®, there has been a slight decrease in yarn breaking strength values compared to 100% cotton yarn. This situation is explained by the inability of Sustans® fibers to be sufficiently incorporated into the yarn structure in blended yarns. Although the strengths of the used cotton and Sustans® fibers are very close to each other, as the Sustans® ratio increases (60% and 70% Sustans® ratios) in the blended yarns, fiber clumps (Figure 5) has formed inside the rotor and spinning has become difficult [9]. The trend seen in yarn strength values is also reflected in the weft direction tensile strength of the fabrics.

(a)

(b)
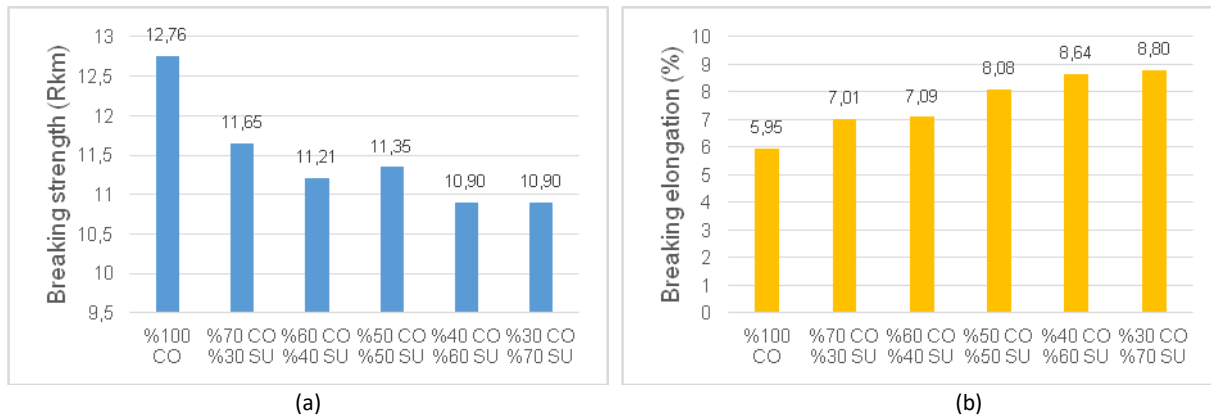
Figure 4. a) Yarn breaking strength graph   b) Yarn breaking elongation graph

Figure 5. Fiber clumps inside the rotor for 60% and 70% Sustans® ratios [9]

Figure 6. Tearing strength at the weft and warp direction

Since the elongation value of the Sustans® fibers is 35.73% and is five times higher than the cotton fibers with 7.27%, the yarn elongation values have increased with the use of Sustans® (Figure 4-b). A similar trend was observed in fabric breaking elongation at weft direction (Figure 3-b). According to the Pearson correlation test, a statistically significant and very high positive correlation was found between the blending ratio and breaking elongation at the weft direction (Table 4). Since the warp threads of all fabrics are the same, the warp direction elongation values are close to each other (Figure 3-b). There was no statistically significant linear correlation between blending ratio and fabric breaking elongation at the warp direction (Table 4).

3.3. Fabric Tear Strength

In the tearing tests, the tearing behaviour of the weft yarns is determined in the warp direction. For this reason, warp tear strength values are essential for the research. The average test results are given in Figure 6 graphically.

Correlation analysis showed a statistically significant (p <0.01) and moderately positive correlation in the warp direction, but there is no statistically significant relationship between the Sustans® ratio and fabric tear strength in the weft direction. According to the ANOVA test (Table 5), there was no statistically significant effect of blending ratios on tear strength in weft direction (p> 0.05). The variation graph of tear strength is consistent with the ANOVA results. It is an expected result because the warp threads of the fabrics are the same. The Kruskal Wallis test (Table 6) showed that the blending ratios have a statistically significant effect on the warp direction tearing values (p <0.05).

It can be said that the use of Sustans® has not improved the tear strength of the warp direction up to 50% blending ratio. Above this ratio, Sustans® supports the tear strength of fabrics in warp direction. In the tear strength test, the yarns are forced to break sequentially. Therefore, the most critical factor in test results is yarn strength. However, the yarn under the effect of force is supported by following yarns at

the yarns' level of adhesion. It was also observed that yarns, including 60% and 70% Sustans® exhibit the lowest strengths. The fabrics produced from these yarns showed the highest warp tearing strength values. This indicates that the yarns which include a high percentage of Sustans® fiber have higher adhesion and the ability to move together within the fabric.

3.4. Dimensional Change after Washing

Washing processes are conducted at two different temperatures, which are frequently used in domestic washing, to examine dimensional change behaviour. All dimensional changes occurred as minus shrinkage. Test results are given graphically in Figure 7. When the dimensional change graph is examined, as the general trend at both temperatures, decreasing shrinkage was observed as the Sustans® ratio increased. Correlation analysis results also support the trend in the graph (Table 4). The Pearson correlation test exhibited very high and high levels of significant negative correlation among the blending ratio with 40ºC and 60ºC weft direction washing data. According to results, a significant and moderately positive relationship between the Sustans® ratio and the 40ºC warp direction washing data were determined. On the other hand, there was no statistically significant relationship between warp direction 60ºC washing data and blending ratio. The ANOVA test (Table 5) showed that the blending ratios have a statistically significant effect on all washing types (p <0.05).

A negative and high-level linear relationship was found between weft direction shrinkage and yarn elongation values with the correlation coefficients -0.815 for 40ºC and -0.702 for 60 ºC. Besides, there was an increase in shrinkage after 60ºC washing compared to 40ºC. This situation is expected because the washing done at 60ºC caused the fabric structure to be relaxed more than 40ºC. Because the tensions within the fabric relaxed during washing cause shrinkage, and some strains can loosen at higher temperatures.

In Figure 7, shrinkage at 60ºC increased compared to 40ºC, similar to the weft direction. Dimensional variations in warp direction generally tend to increase slightly with an increase of the Sustans® ratio, and this trend is not as evident as in the weft direction. Correlation analyzes also support this weak trend. Besides, considering that the fabrics have the same warp yarns, it is concluded that the Sustans® ratios do not have a significant effect on the warp direction shrinkage.

3.5. Elasticity and Growth

Tests were applied only in the weft direction, as there was only elasticity expectation in weft direction. However, the tests were conducted separately to the finished samples, and samples washed at 60ºC. Correlation test showed that (Table 4) the moderate and high level negative correlations among blending ratio with finished product elasticity and post-washing elasticity data (p <0.01). A weak level of significant negative correlation (p <0.05) was found between the growth after washing and the blending ratio. According to the ANOVA test results (Table 5), it was determined that the blending ratio had a statistically significant effect on the elasticity of samples (p <0.05).

In Figure 8, it is seen that the finished fabrics containing weft yarns, which include 60% and 70% Sustans®, had lower elasticity compared to other samples. In the elasticity data of washed fabrics, elasticity values decrease with increasing Sustans® ratio. Graphic trends in terms of elasticity are consistent with correlation analysis.

The Kruskal Wallis test showed that the blending ratio had no statistically significant effect (p = 0.299) on the growth data after washing. The graph of growth changes and correlation analysis also did not indicate a strong relationship. Elasticity values of washed fabrics have increased compared to finished samples. Compared to 100% cotton fabric, some improvement was observed in the growth values of the fabrics containing Sustans® after washing.
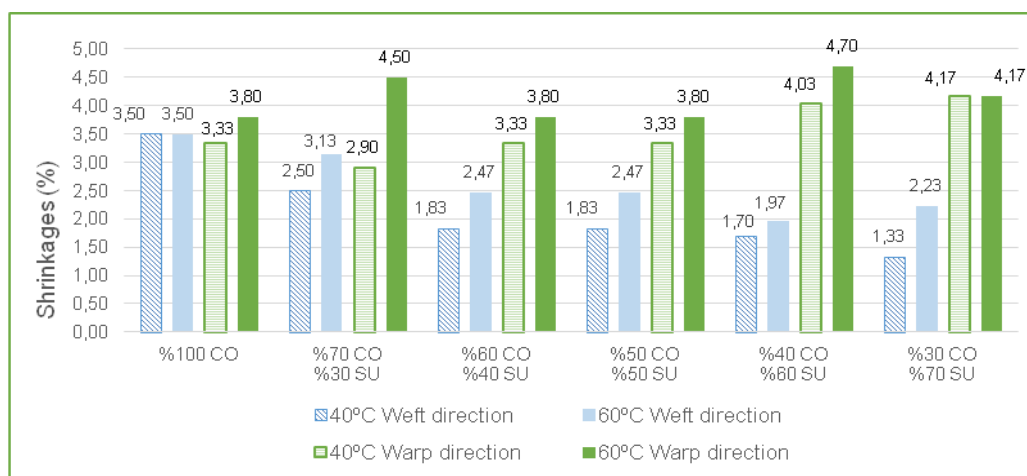

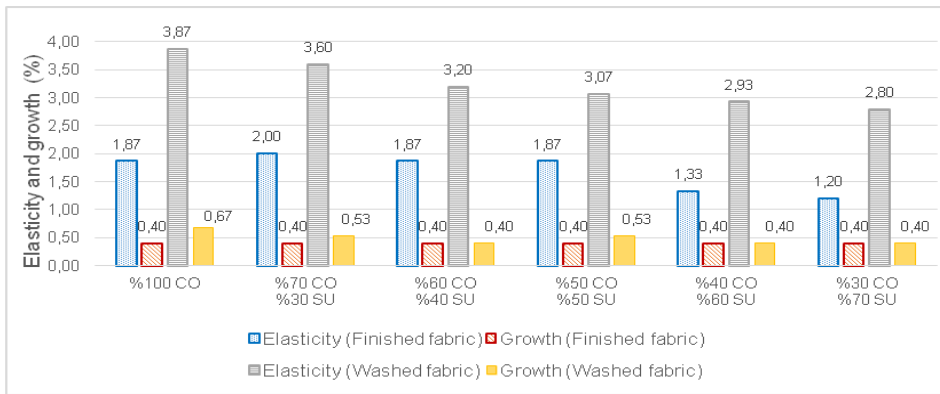**Figure 7.** Dimensional change graphs

Figure 8. Elasticity and growth graphs

As a result, it was determined that the finished fabrics elasticity values were not affected by the use of Sustans® up to 60%; the Sustans® ratios above 60% negatively affect the elasticity. Moreover, the elasticity values after washing decreased with the increase of the Sustans® ratio. Besides, it was determined that the after washing elasticity values increased compared to the finished fabrics. It has been concluded that 60ºC washing provides more relaxing in the finished fabric than 40ºC, the fabric recover a little more. As a result, the potential elongation capability becomes a little more active. It has been evaluated that the dimensional changes after 60ºC washing are greater than 40ºC, which confirms this claim. More shrinkage is observed in washing at higher temperatures, which provides more elongation in the elasticity test. Thus, the elasticity and the growth values increase.

When elasticity and growth data are analyzed together, the low growth and elasticity values indicate that the fabrics exhibited low elongation during the tests. However, it was seen that the breaking elongation values increase as the Sustans® ratio increases both in yarn and fabric. The critical detail at this point is that, in accordance with standard methods, the breaking elongation values of the fabrics were obtained at the force level of 850-900 N, and elasticity values at the force level of approximately 23 N. In other words, as the Sustans® ratio increases, the elongation values

increase, but this increase can manifest itself at much higher levels than the stresses that may occur in daily use and applied elasticity tests.

Sustans® fibers must be opened and longitudinally settled in the yarn structure during the spinning process to benefit sufficiently from the elasticity and dimensional stability properties. It was concluded that the airflow, centrifugal force, etc., parameters in the rotor were not adequate to open Sustans® fibers longitudinally; therefore, the elasticity property of Sustans® fibers could not be adequately transferred to the yarn and fabric structure. However, while a slight decrease was observed in the elasticity value of the fabrics with a 50 % Sustans® determined in the previous study as the optimum blending ratio [9], there was some improvement in the growth after washing.

3.6. Pilling

Pilling and abrasion behavior of fabrics are affected by many factors such as fiber type, yarn and fabric properties. However, in the study, all factors except weft yarn fiber mixing ratios were kept constant. For this reason, fabric pilling and abrasion behaviors were investigated by considering the results of weft yarn hairiness and fabric stiffness. For this purpose, the graphics of weft yarn hairiness data evaluated in the previous study are given in Figure 9 [9].
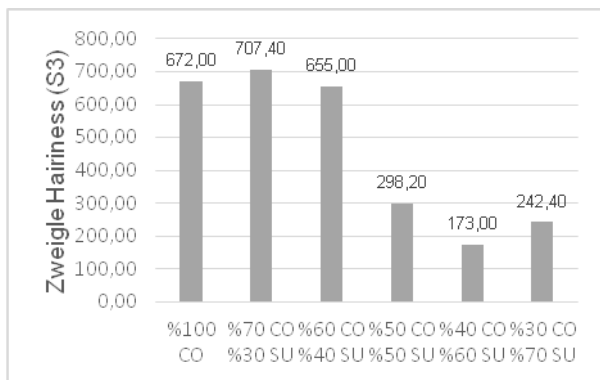
(a)
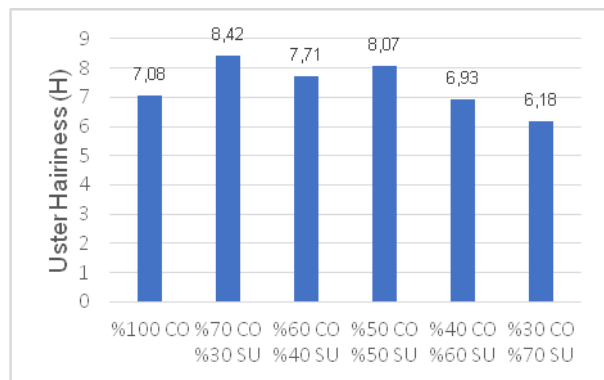
(b)

Figure 9. a) Zweigle S3 hairiness graph; b) Uster H hairiness graph

In terms of hairiness data S3, yarns with a Sustans® ratio of 50% and above and yarns with a Sustans® ratio of less than 50% were separated into two different groups. These two groups did not show significant differences within themselves. It was stated that the use of Sustans® had a statistically significant effect on the hairiness values of Uster H and Zweigle S3. The use of Sustans® at rates of 50% and above significantly reduced the S3 hairiness values. A statistically significant and highly negative linear relationship (Pearson correlation coefficient -0.791) was observed between the sustans ratio and S3 hairiness value. A statistically significant linear relationship was not found between the Uster H hairiness values and the Sustans® ratio [9].

The similar or different behavior of yarns in terms of H and S3 hairiness is highly affected by the amount of fibers shorter than 3 mm or not [29]. Considering that unwanted hairs in yarns consist of fibers of 3 mm and longer [30], yarns containing 50% and more Sustans® are more advantageous compared to other yarns [9].

Circular stiffness tests were applied to determine the possible effects of weft yarns containing Sustans® in different mixing ratios on the resistance of fabrics to bending. The graphic reflecting the average test results obtained is given in Figure 10.

According to the ANOVA test result given in Table 5, the Sustans® ratio has a statistically significant effect on fabric stiffness (p <0.05). With the use of Sustans® fibers, which

are known to have a soft touch, the fabric stiffness values have decreased, in other words, the softness of the fabrics has increased. On the other hand, Pearson correlation analysis showed that there was no statistically significant linear relationship between Sustans® ratio and stiffness test results (Table 4). The fabric with 50% Sustans® ratio became the softest fabric with the lowest stiffness value. As in most of the other tests applied to yarns and fabrics, 50% Sustans® ratio is the mixing ratio at which the trend reversed [2, 9].

Fabric pilling values are given in Table 7. According to the test results, it was observed that all fabrics reached the highest pilling level 2000 cycles. It was determined that the pilling levels of all fabrics decreased at 5000 cycles and the reduction continued at 7000 cycles in some of them.
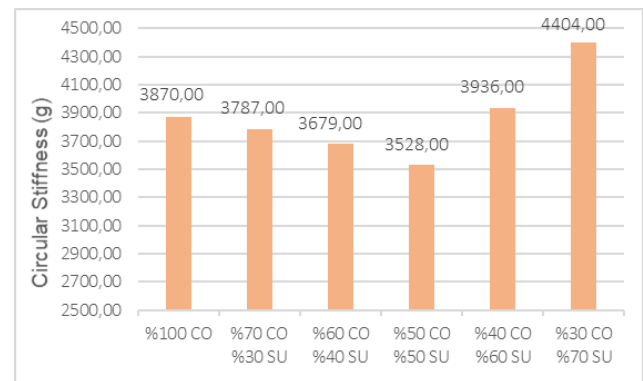
Figure 10. Circular Stiffness graph

Table 7. Pilling test results

Weft Yarn Blend Ratio	Sample Number	Pilling Cycles					
		125	500	1000	2000	5000	7000
%100 CO	1	4	3/4	3/4	3	3	3/4
	2	4	4	3/4	3/4	3/4	4
	3	4	4	3/4	3	3/4	4
%70 CO - %30 SU	1	4	4	3/4	3	3/4	3/4
	2	4	3/4	3	3	3/4	3/4
	3	4	3/4	3	3	3/4	3/4
%60 CO - %40 SU	1	4	4	3/4	3	3/4	3/4
	2	4	3/4	3	3	3/4	3/4
	3	4	3/4	3	3	3/4	3/4
%50 CO - %50 SU	1	4	4	3/4	3/4	3/4	3/4
	2	4	4	3/4	3/4	3/4	4
	3	4	3/4	3/4	3	3/4	4
%40 CO - %60 SU	1	4/5	4	4	3/4	4	4
	2	4	4	4	3/4	4	4
	3	4	4	3/4	3/4	4	4
%30 CO - %70 SU	1	4	3/4	3/4	3/4	3/4	4
	2	4	4	3/4	3/4	4	4
	3	4	4	4	3/4	4	4

The worst results were seen at 30% and 40% Sustans® ratio with 3 degrees of pilling at 2000 cycles. Even though a sample of 100% cotton fabric was better than these two fabrics with a level of 3/4, when the 3 pilling degree of the other two samples were evaluated, it was determined that three fabrics formed a group. Although a sample of the fabric containing 50% Sustans® had a half point worse result with 3 degree of pilling than those containing 60% and 70% the three fabrics formed a separate batch at 2000 cycles. It was determined that these results match the S3 hairiness data of the yarns. All three samples of 50% Sustans® fabric were pilled at the level of 3/4 at 5000 cycles. In other words, 30%, 40% and 50% Sustans® fabrics showed the same amount of pilling at 5000 cycle. However, it was grouped with 60% and 70% Sustans® fabrics again in 7000 cycles. In other words, in 50% Sustans® fabric, the reduction in pilling after the worst level was slower than 60% and 70% Sustans® fabrics. In addition, the pilling degree of 100% cotton fabric at the end of 500 and 7000 cycles is closer to 50% and above Sustans® fabrics. As a result, the use of Sustans® at rates of 50% and above improved the pilling values by half a point for most of the pilling process. However, there was no significant difference in pilling according to the change in Sustans® ratio among the groups formed.

3.7. Abrasion Resistance

The change of abrasion resistance test results is given in Figure 11. Statistical analyzes were applied to make a comparison between fabrics according to the mass losses occurring at the end of each abrasion period, and no comparison was made between different abrasion periods.

Figure 11. Abrasion resistance graph

According to the results of Kolmogorov-Smirnov normality analysis, all data sets showed normal distribution. As a result of the Pearson correlation test (Table 4), a statistically significant and weakly negative linear relationship at the level of 0.05 was found only in the data of 25000 cycl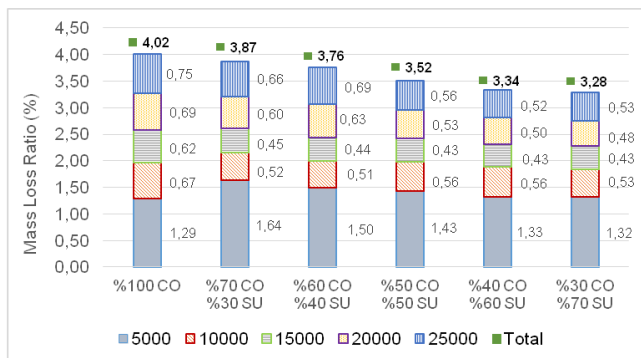es. According to ANOVA test results (Table 5), there was no statistically significant effect of blend ratios on abrasion resistance ($p > 0.05$).

Although there is no clear trend among the mass losses occurring in the cycle ranges, as a result, the increase in the

Sustans® ratio had positive effect on the abrasion resistance. The mass loss of 100% cotton fabric is the lowest at the end of the first 5000 cycles. However, more mass loss was observed than any of the fabrics containing Sustans® in all of the subsequent 5000 cycle periods. As a result, the 100% cotton fabric has abraded more than any other fabric after 25000 cycles. When the graphical view of the first 5000 cycle results is examined, it is determined that the graph show a similar trend to the yarn H hairiness values. In the abrasion test, the highest mass losses are usually seen at the beginning of the test. The reason for the high mass losses at the beginning is the rapid removal of the fibers on the fabric surface, which is caused by the yarn hairiness. This explains the similarity of the graphic image at the end of the first 5000 cycles to the H hairiness graph.

However, 100% cotton yarn is much hairier than the yarns including 60% and 70% Sustans® in terms of Uster H and S3 hairiness values. In fact, according to the mass loss data at the end of the first 5000 cycles, 100% cotton fabric is more durable than all fabrics. In this case, it was concluded that fiber melting and pilling observed on the yarn surfaces containing Sustans® are also effective [9]. It was evaluated that these beads rapidly moved away from the fabric surface at the begining of the abrasion resistance test and increased mass loss in the first 5000 cycles of fabrics containing Sustans®. As a result, although the hairiness of yarns containing 60% and 70% Sustans® was lower than 100% cotton yarn, the mass loss of fabrics containing these yarns in the first 5000 cycles was higher than 100% cotton fabric due to the fiber beads. It has been determined that fabrics produced with less hairy yarns have higher abrasion and pilling resistance, and this result is consistent with previous studies [31].

As raw materials, polyester, polyamide, polypropylene fibers are high, wool, cotton fibers are medium; viscose and acetate fibers have low abrasion resistance [32]. Therefore, the abrasion resistance of Sustans® fibers, which form the phthalates branch of aromatic polyesters together with Poly (ethylene Terephthalate) (PET) and Poly (butylene Terephthalate) (PBT), is higher than cotton fibers. For this reason, the abrasion resistance of the fabrics containing Sustans® was higher.

4. CONCLUSION

In this study, Sustans® fibers, produced from renewable natural resources, bio-based, sustainable, having good elasticity and dimensional stability, were used in rotor spinning system. Although there is a slight decrease in the weft and warp tensile strength of denim fabrics, including these yarns in the weft, these values have provided the required limit values according to the TS 2791 "Textile - Cotton Denim Fabric" standard. On the other hand, a statistically significant and very high positive correlation was found between weft breaking elongation and Sustans® ratio.

The use of 50% or more Sustans® has increased the tear strength of fabrics compared to 100% Cotton fabric. Study results showed that the use of Sustans® has improved the dimensional stability of the denim fabrics against washings.

The elasticity of Sustans® fibers has not been adequately transferred to the yarn and fabric structure. The reason for this result was evaluated that Sustans® fibers could not be opened enough longitudinally during spinning. However, it was observed that the use of Sustans® slightly improved the permanent elongation values.

When the results are evaluated in general, the use of Sustans® 50% and above in the weft yarn improved the pilling values of the fabrics. S3 hairiness values of the yarns affected the fabric pilling especially at 2000 cycles. However, due to the reduction of hairiness on the fabric surface as a result of processes such as finishing, it has been determined that this effect is limited according to the difference between the amount of hairiness.

In general, it has been observed that the use of Sustans® has a positive effect on abrasion resistance and the abrasion resistance increases as the Sustans® ratio increases. However, it has been determined that the positive effect is limited until about 10.000 abrasion cycles especially at low Sustans® rates. Within the scope of the study, it has been determined that the use of Sustans® has a more positive effect at the end of long abrasion periods and this positive effect can create an advantage for denim fabrics that are used frequently and for a relatively long time.

In the previous study, 50/50% Sustans®/Cotton was specified as the optimum blending ratio for the yarns [9]. In terms of fabric properties measured in this study, denim fabrics, containing 50% Sustans® in the weft, were also evaluated as the having optimum blend yarns. However, it should not be ignored that the yarns containing Sustans® are only weft in the fabrics. If also 50/50% Sustans®/Cotton yarns are used in the warp direction, it is most likely that some advantages, obtained in the weft direction, will be seen in the warp direction. In addition, improvement in pilling and abrasion resistance properties may also occur.

REFERENCES

1. Kerkhof RVD. 2018. Innovative by Nature Time to Act. Lenzing AG Retrieved from https://www.unece.org/fileadmin/DAM/timber/meetings/2018/20181105/COFFI2018_-_Circular_Economy_-_van_de_Kerkhof.pdf.

2. Özkan M. 2019. *Investigation of the Performance Properties of PTT/Cotton Blended OE-Rotor Yarns and Denim Fabrics Using These Yarns* (MSc Thesis). Çukurova University, Institute of Natural and Applied Sciences, Department of Textile Engineering.

3. Kurian JV. 2005. A new polymer platform for the future—Sorona® from corn derived 1, 3-propanediol. *Journal of Polymers and the Environment* 13(2), 159-167.

4. Yıldırım FF, Avinç OO, Yavaş A. 2012. Poly (trimethylene terephthalate) fibres, Part 1: Production, properties, end-use applications, enviromental Impact. *Journal of Textiles and Engineer* 19(87), 43-54.

5. Springer Nature. 2018. The price of fast fashion. Nature Climate Change, Retrieved from https://www.nature.com/articles/s41558-017-0058-9.

6. DuPont. 2019. The Sorona® Story. Retrieved from http://sorona.com/our-story/

7. Houck MM, Huff R, Lowe P, Menold R. 2001. Poly (trimethylene terephthalate): A "new" type of polyester fibre. *Forensic Science Communications* 3(3), 217–221.

8. Perepelkin KE. 2001. Poly (ethylene terephthalate) and polyester fibres–60th anniversary of the first patent-Poliester fibres abroad in the third millenium. *Fibre Chemistry* 33(5), 333-339.

9. Özkan M, Duru Baykal P, Özkan İ. 2022. Investigation on the performance properties of polytrimethylene terephthalate (PTT) based staple fibers and cotton blended OE-rotor yarns. *The Journal of the Textile Institute* 113(3), 449-459.

10. Bağıran İC. 2011. *Problems occuring in denim laundry, their preventive solutions and correction possibilities* (MSc Thesis). Ege University, Institute of Natural And Applied Sciences, Department of Textile Engineering.

11. Telli A, Babaarslan O. 2017. The effect of recycled fibers on the washing performance of denim fabrics. *The Journal of the Textile Institute* 108(5), 812-820.

12. Seyrek Kurban N. Babaarslan O. 2019 Literature review on the properties of super stretch denim fabrics. *Journal of Textiles and Engineer* 26(113), 104-115.

13. Oh TH. 2006. Effects of spinning and drawing conditions on the crimp contraction of side-by-side poly(trimethylene terephthalate) bicomponent fibers. *Journal of Applied Polymer Science* 102, 1322–1327.

14. Luo J, Wang F, Xu B. 2011. Factors affecting crimp configuration of PTT/PET bi-component filaments. *Textile Research Journal* 81(5), 538-544.

15. Wang F, Gu F, Xu B. 2013. Elastic strain of PTT/PET self-crimping fibers. *Journal of Engineered Fibers and Fabrics* 8(2), 50-55.

16. Al-Juaidiyah J. 2015. Pyrolysis kinetics of recycled polyesters. *International Journal of Clothing Science and Technology* 27(4), 523-531.

17. Resch-Fauster K, Klein A, Blees E, Feuchter M. 2017. Mechanical recyclability of technical biopolymers: Potential and limits. *Polymer Testing* 64, 287-295.

18. İçoğlu Hİ, Oğulata RT. 2017. Effect of ambient parameters on morphology of electrospun poly(trimethylene terephthalate) (PTT) fibers. *Tekstil ve Konfeksiyon* 27(3), 215-223.

19. Hua T, Wong NS, Tang WM. 2018. Study on properties of elastic core-spun yarns containing a mix of spandex and PET/PTT bi-component filament as core. *Textile Research Journal* 88(9), 1065-1076.

20. Zhao L, Qin L, Wang F, Chuah HH. 2009. Factors affecting recovery of PTT shape memory fabric to its initial shape. *International Journal of Clothing Science and Technology* 21(1), 64-73.

21. Luo J, Wang FM, Li D, Xu B. 2011. Elasticity of woven fabrics made of polytri-methylene terephthalate/polyethylene terephthalate bicomponent filaments. *Textile Research Journal* 81(8), 865-870.

22. Yan YX, He L, Lei SS, Lu YP, Feng YN, Tao JW. 2013. The performance test and analysis of sorona elastic swimsuit fabric. *Advanced Materials Research* 821, 415-418.

23. Zhao L, Hu H, Shen J, Rong H. 2013. The use of a polytrimethylene terephthalate/polyester bi-component filament for the development of seamless garments. *Textile Research Journal* 83(12), 1283-1296.

24. Jin ZM, Li X, Yan YX, Tao JW. 2014. Study on wearing characteristics of sorona/cotton blended seamless knitted fabric. *Applied Mechanics and Materials* 633, 460-463.

25. Jianbo XIAO, Xiaogang ZHA, Xiaomei LI, Xinxin LI. 2020. Development of nano-crystallite functional modal/cashmere/ Sustans fiber blended yarn. *Wool Textile Journal* 48(3), 30-35.

26. Akgül A, Çevik O. 2003. Statistical Analysis Techniques, Business Management Applications in SPSS. Journal of Accounting and Tax Applications. 1st Edition, Ankara, Emek Ofset (in Turkish).

27. Sheshkin DJ. 2020. Handbook of parametric and nonparametric statistical procedures. New York: CRC Press.

28. Hollander M, Wolfe DA, Chicken E. 2013. Nonparametric Statistical Methods (Vol. 751). USA New Jersey: John Wiley & Sons.

29. Alay S, Göktepe F. 2008. An investigation of the correlation between different yarn hairiness parameters. *Tekstil ve Konfeksiyon* 1, 28-34.

30. Örtlek HG, Babaarslan O. 2003. An investigation of the hairiness of core-spun yarns containing spandex (lycra). *Uludağ University Journal of the Faculty of Engineering and Architecture* 8(1), 79-93.

31. Türksoy HG, Akaya T, Üstüntağ S. 2017. Evaluation of woven fabric performances of air-jet yarns. *The Journal of Textiles and Engineer* 24(107), 138-145.

32. Tayyar AE, Sarı F, Yağız İ. 2011. The effects of structural parameters of shirting fabrics on abrasion resistance. *The Journal of Textiles and Engineer* 18(84), 23-26.

A Study on the Strength Properties of Various Buttons Used in Garments

Nilgün Özdil[1] 0000-0001-9488-5337
Esra Zeynep Yıldız[2] 0000-0001-6143-8768
Gamze Süpüren Mengüç[2] 0000-0002-2786-7283
Oktay Pamuk[1] 0000-0001-6751-2527

[1] Ege University Textile Engineering Department Izmir, Türkiye
[2] Ege University Emel Akin Vocational Training School Izmir, Türkiye

Corresponding Author: Esra Zeynep Yıldız, esra.zeynep.yildiz@ege.edu.tr

ABSTRACT

Auxiliary materials are as important as fabric, which is the main material of a garment. One of the most important auxiliary materials is the button. There are different types of buttons, made of different materials, with different numbers of holes in different sizes. The breaking strength of the button determines the performance characteristics of the buttons during usage. In this study, commonly used types of buttons were investigated and the breaking strength values of different buttons were measured. The results show that the breaking strength of buttons is related to the number of holes in the button, the size of the sewing thread, and the fabric type. However, the effects of button size and button material were found to be statistically insignificant.

1. INTRODUCTION

The development of fashion accessories has gained momentum with the fast-growing fashion consciousness. A garment is an ensemble of fabric and accessories. It is possible to say that the garment remains incomplete without accessories [1]. While fabrics are the main component of the garment, an equally important component is the accessories that make up the complete assembly [2]. Auxiliary materials and accessories are indispensable elements, especially in the garment industry. They are as important as the fabric, which is the main material of a garment. They complete the garment or utility item in terms of functionality or aesthetics. One of the most important auxiliary materials is the button, which has been known since pre-Christian times. They are commonly used in the ready-to-wear industry to fasten garments, but they are also an important accessory as they add aesthetic value to garments.

A button is a small, usually round disk usually attached to a garment to close an opening or decorate it. Buttons come in a variety of materials, colors and shapes. They can be made from a variety of materials, including natural materials such as antler, bone, hard fiber, pearl, horn, ivory, shell, vegetable ivory and wood or synthetic materials such as celluloid, glass, metal, bakelite and plastic. The choice of buttons depends on the clothing style, cost and care of the garments [1, 3, 4]. Natural materials offer buttons with some variability in color, pattern, possibly in size and shape, at a higher cost, while man-made materials are more uniform and less expensive [5].

Buttons usually have a round shape. The diameter of the button is measured by the same system regardless of the type of button or material. The unit for measuring the diameter is the line (L). One line is equal to 1/40 of an inch [3]. Buttons that can be sewn usually have 2 or 4-holes [6] and they are sewn onto garments using the single-thread chain stitch, lockstitch or simulated hand stitch. The single-

thread chain stitch provides an insecure button attachment [5]. For this reason, the lockstitch is preferred for children's garments.

Important properties of buttons are color fastness, compressive strength, dry cleaning solubility (durability), heat resistance, impact resistance, mildew resistance, launderability, tensile strength and water resistance [3].

The button strength test shows how tightly the button is attached to the fabric. For this purpose, by attaching special apparatus to conventional tensile strength devices or special test devices for buttons strength are used. In addition, other important mechanical strength tests are performed on buttons. The "fatigue test" measures the performance of the button after it has been subjected to a certain load. The "button leg separation strength test" shows the structural deformation of the button [7].

There is some research on the performance characteristics of auxiliary materials such as zippers [8,9], linings [10,11], sewing threads [12,13,14] and interlinings [15,16]. However, as a result of the literature review, no systematic study has been conducted to investigate and compare the effects of different variables on the breaking strength of buttons for apparel products with specific types, sizes and numbers of holes. Therefore, the aim of this paper is to investigate and compare the effects of button material, button size, number of buttonholes, fabric type and sewing thread count on the breaking strength of buttons. It is thought that this study will lead the way in conducting studies to investigate the properties of buttons.

2. MATERIAL AND METHOD

2.1 Material

In this study, 28 buttons with different sizes and materials were used. Polyester, wooden and coconut buttons, commonly used for garments, with 2 and 4-holes in different sizes were selected. The buttons used in the study and their characteristics are shown in Table 1. Different fabrics and sewing threads were used to determine the effects of other parameters. The properties of the fabrics and sewing threads are given in Tables 2 and 3.

2.2 Method

Sample preparation

The Lewis 200-1 button sewing machine was used to sew the buttons to the fabric. Parallel stitches were used when sewing the buttons on. During sewing, the number of needle penetrations was kept constant for all trials. All buttons were first sewn to the same fabric (F1) using the same sewing thread (ST1) to determine the effect of button size, button type and number of holes on the strength of the buttons. To determine the other effects (sewn fabric and sewing thread) a cotton fabric with similar fabric construction (plain) and lower fabric weight (F2) and a polyester core-spun thread with higher thread count (ST2) were used.

Table 1. Properties of the buttons

Button code	Type	Size (L)	Number of holes	Average breaking strength (N)
B1	PES	>40	4	29,43
B2	PES	40	4	27,83
B3	PES	36	4	26,93
B4	PES	28	4	26,20
B5	PES	24	4	25,60
B6	PES	20	4	26,23
B7	PES	18	4	25,53
B8	PES	16	4	25,53
B9	PES	14	4	21,77
B10	PES	40	2	18,47
B11	PES	32	2	18,87
B12	PES	24	2	19,73
B13	PES	22	2	20,00
B14	Wooden	40	4	26,95
B15	Wooden	36	4	26,90
B16	Wooden	28	4	25,70
B17	Wooden	18	4	25,37
B18	Wooden	32	2	16,33
B19	Wooden	20	2	18,97
B20	Coconut	40	4	28,45
B21	Coconut	18	4	26,30
B22	Coconut	40	2	15,90
B23	Coconut	32	2	18,10
B24	Coconut	28	2	19,03
B25	Coconut	24	2	20,17
B26	Coconut	20	2	20,17
B27	Coconut	18	2	19,63
B28	Coconut	14	2	21,20

Table 2. Properties of the fabrics

Fabric code	Material	Construction	Density (thread/cm)		Mass per unit area (g/m²)
			Warp	Weft	
F1	Cotton	Plain	24	17	134
F2	Cotton	Plain	64	42	60

Table 3. Properties of sewing threads

| Sewing thread code | Type | Thread count | | Number of plies |
		Tex	TKT	
ST1	Polyester-polyester core-spun	30	100	2
ST2	Polyester-polyester core-spun	60	50	3

Button breaking strength test

In order to determine the performance of sewn buttons during usage, a button-breaking strength test was conducted by Prowhite Button Strength Measurement Device (Figure 1). In this test, the sewn button is placed between two jaws and the strength of the button is measured by applying tensile and rotational forces (Figure 2).

Statistical evaluation

Evaluation of the test results was assessed by analysis of variance (ANOVA) using SPSS software. To determine if the group means were significantly different, the significance level (p-value) was determined. In this analysis, only those cases that had statistical significance beyond the 5% level ($0 \leq p \leq 0,05$) were considered significant. Independent samples t-test and Student-Newman-Keuls tests were performed to determine whether the effects of button size, button type, number of holes and other parameters on the breaking strength of the buttons were statistically significant.

Figure 1. Button strength measuring device and the jaws
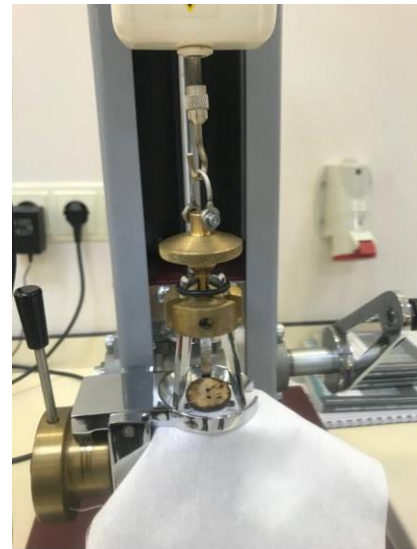
Figure 2. Execution of the test

3. RESULTS AND DISCUSSION

In this part, the effects of button size, number of holes, button type, fabric type and sewing thread count on the breaking strength of buttons were evaluated respectively. When testing the breaking strength of individual buttons, the breakage always occurred in the sewing thread or fabric.

3.1. Effect of button size

4-hole buttons

The breaking strength values of 4-hole buttons are shown in Figure 3. To determine the effects of button size on PES and wooden buttons, the SNK multiple comparison test was used (Table 4), while the independent samples t-test was used to evaluate coconut buttons (Table 5).

Figure 3. Breaking strength values of 4-hole buttons

Table 4. Effect of button size on 4-hole buttons

Button code	N	Subset 1	Subset 2	Button code	N	Subset 1
B9	3	21,7667		B17	3	25,3667
B7	3	25,5333	25,5333	B16	3	25,7000
B8	3	25,5333	25,5333	B15	3	26,9000
B5	3	25,6000	25,6000	B14	3	26,9500
B4	3	26,2000	26,2000			
B6	3	26,2333	26,2333			
B3	3	26,9333	26,9333			
B2	3		27,8333			
B1	3		29,4333			
Sig.		**1,000**	**0,153**	**Sig.**		**0,542**

Table 5. Significance values of independent sample t-test

Parameter	Button type	Button size	Significance
Effect of button size	Coconut 4-hole buttons	B20 (40 L) / B21 (18 L)	0,383
Effect of button size	Wooden 2-hole buttons	B18 (32 L) / B19 (20 L)	0,272
Effect of number of holes	PES buttons (24 L)	B5 (4-hole) / B12 (2-hole)	0,042*
	PES buttons (40 L)	B2 (4-hole) / B10 (2-hole)	0,003*
	Coconut buttons (18 L)	B21 (4-hole) / B27 (2-hole)	0,044*
	Coconut buttons (40 L)	B20 (4-hole) / B22 (2-hole)	0,047*
Effect of fabric type	PES buttons (B12)	F1 / F2	0,001*
	Coconut buttons (B25)	F1 / F2	0,003*
Effect of sewing thread size	PES buttons (B12)	ST1 / ST2	0,013*
	Coconut buttons (B25)	ST1 / ST2	0,003*

* Significant according to p=0,05 significance level.

Figure 3 shows that the breaking strength values of all button types are higher for larger sizes, while they are lower for smaller sizes. Within the group, the PES button with a diameter of >40 L (B1) has the highest value, while the PES button with a diameter of 14 L (B9) has the lowest value. It can be seen that the value of breaking strength tends to decrease for all button types with smaller diameters. However, the statistical test results show that the differences between the results are insignificant, except for the results of the buttons having the largest and smallest button sizes (B1, B2 and B9).

2-hole buttons

The breaking strength values of 2-hole buttons are shown in Figure 4. To determine the effects of button size on PES and coconut buttons, the SNK multiple comparison test was conducted (Table 6), while the independent samples t-test was used to evaluate wooden buttons as indicated in Table 5.
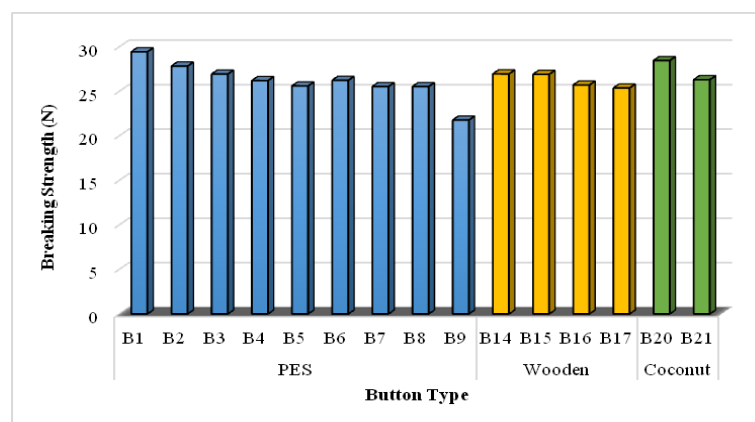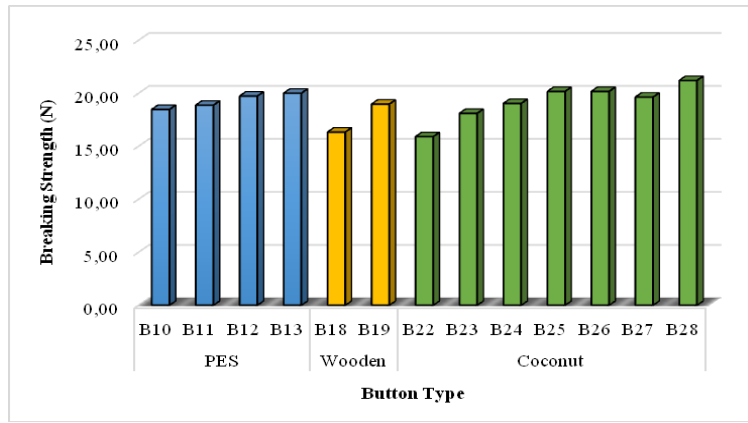
Figure 4. Breaking strength values of 2-hole buttons

Table 6. Effect of button size on 2-hole buttons

| Button code | N | Subset | | Button code | N | Subset |
		1	2			1
B22	3	15,9000		B10	3	18,4667
B23	3	18,1000	18,1000	B11	3	18,8667
B24	3	19,0333	19,0333	B12	3	19,7333
B27	3	19,6333	19,6333	B13	3	20,0000
B25	3	20,1667	20,1667			
B26	3	20,1700	20,1700			
B28	3		21,2000			
Sig.		**0,061**	**0,190**	**Sig.**		**0,730**

As can be seen from Figure 4, in contrast to the 4-hole buttons, the button with the smallest diameter was found to have the highest value for breaking force and as the button size decreased, the mean value for breaking force increased. However, the difference between the results is not statistically significant for PES and wooden buttons.

3.2. Effect of button type

To determine the effect of button type, buttons made of different materials but with the same diameter and number of holes, were selected. The breaking strength values of 2-hole buttons made of different materials with the same diameter (32 L) and 4-hole buttons made of different materials with the same diameter (18 L) are shown in Figure 5. To determine the effect of button type on breaking strength, the SNK multiple comparison test was performed, which is given in Table 7.
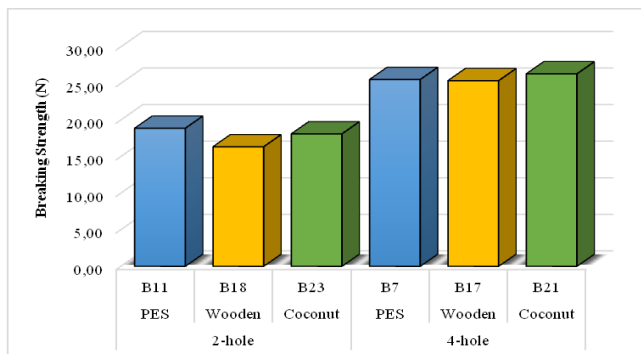
Figure 5. Breaking strength values of 2-hole and 4-hole buttons with same diameter

Table 7. Effect of button type on 2-hole and 4-hole buttons with the same diameter

| Button code | N | Subset |
		1
Wooden (B18)	3	16,3333
Coconut (B23)	3	18,1000
PES (B11)	3	18,8667
Sig.		**0,466**
Wooden (B17)	3	25,3667
PES (B7)	3	25,5333
Coconut (B21)	3	26,3000
Sig.		**0,913**

According to the results, the wooden buttons had the lowest breaking strength values among the other buttons with the same diameter and number of holes. However, no significant differences were found between the button types in the breaking strength values of the buttons (see Table 7). Since the gripper jaw completely grips the button, the breakage always occurs in sewing thread or fabric during the button breaking strength test.

3.3. Effect of number of holes

To investigate the effect of the number of holes on the strength of the buttons, PES buttons with the same diameters, 24 L and 40 L, and coconut buttons 18 L and 40 L were compared respectively. The effect of the number of holes on the breaking strength values is shown in Figure 6, and the statistical analysis is given in Table 5.

When considering the effect of the number of holes on the breaking strength of PES and coconut buttons of the same diameter, it was found that the average value of breaking

strength was higher for buttons with 4-holes and the differences between the values were statically significant. During the sewing process, the number of needle penetrations was kept constant for buttons with 2 and 4-holes. Thus, for 2-hole buttons, the number of needle penetration per hole is twice as higher than 4-hole buttons. For this reason, fabrics sewn with 2-hole buttons have more damage at the puncture points in the fabric structure than fabrics sewn with 4-hole buttons. Moreover, in 4-hole buttons, the button and fabric are connected at four different points, whereas 2-hole buttons have a 2-point connection. It is believed that the higher number of connections between fabric and button positively affects breaking strength test results.
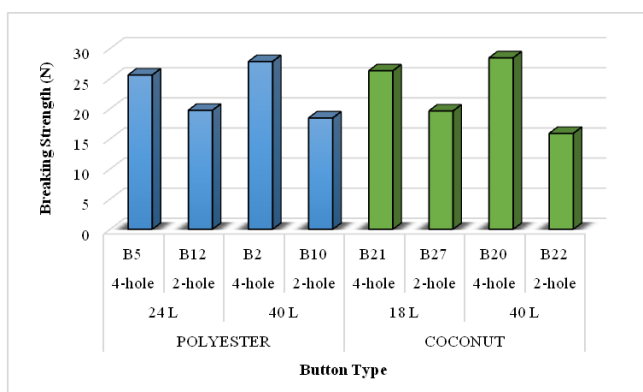

Figure 6. Breaking strength values of buttons with the same diameters in different numbers of holes

3.4. Effect of other parameters

3.4.1. Effect of sewn fabric

For examining the effect of fabric type on the button breaking strength, 2-hole buttons (PES and Coconut buttons) with a diameter of 24 L were sewn using two different fabrics (F1 and F2) with the same sewing thread (ST1). The test results and statistical analysis of the samples are given in Figure 7 and Table 5, respectively.
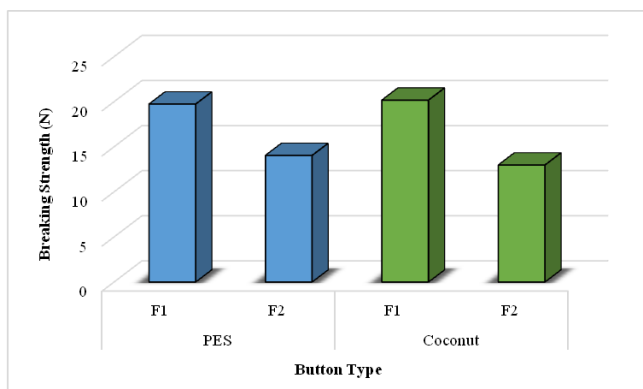

Figure 7. Breaking strength values of 2-hole buttons (24 L) sewn with different fabrics

When sewing 2-hole buttons of the same diameter to different fabrics, it was found that the heavier and tighter fabric had the highest strength, as expected. Since a tight

and heavier fabric is used, the fabric is less damaged, so the button-breaking strength is also higher. This indicates that the type of fabric affects the strength values of the buttons.

3.4.2. Effect of sewing thread

To investigate the effect of sewing thread size on button breaking strength, 2-hole buttons (PES and Coconut buttons) with the same diameter (24 L) were sewn using two different sewing threads (ST1 and ST2). The test results and statistical analysis of the samples are given in Figure 8 and Table 5, respectively.
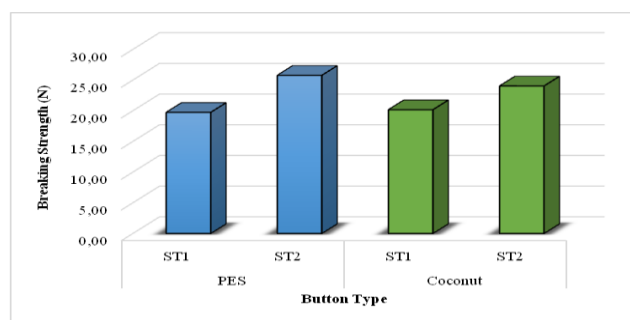
Figure 8. Breaking strength values of 2-hole buttons (24 L) sewn with different sewing threads

As shown in Figure 8, the sewing thread affects the breaking strength of the buttons. In both PES and coconut buttons, the buttons sewn with 60 tex thread showed higher durability than those sewn with 30 tex. The strength of the buttons sewn with thicker threads was higher than the strength values of the buttons sewn with thinner threads.

4. CONCLUSION

Buttons, which can be considered an essential material for garments, are used to fasten or decorate the garment. They are commonly used in the ready-to-wear industry, where they are needed for fastening, but they are also an important accessory, as they add aesthetic value to the garments for which they are used. The properties expected of buttons vary depending on their use. In particular, testing the strength of buttons is critical for garment use, performance and durability.

This study examined button types commonly used in the apparel industry, and the objective was to measure the breaking strength of the different buttons. This study focused on the physical parameters such as button size, button type, number of holes, and the effect of these parameters on the breaking strength of buttons. For this purpose, 28 buttons with different structural properties (size, type and number of holes) were supplied to study the breaking strength of the buttons.

In this study, the following results were found:

- A slight decrease in the breaking strength values of 2-hole buttons was observed with increasing button size. Opposite to that, higher values were obtained for 4-

hole buttons, however, the effect of button size was found to be statistically insignificant.

- The breaking strength values of 4-hole buttons are statistically higher than those of 2-hole buttons. This is due to the fact that fabrics sewn with 2-hole buttons show more damage at the puncture points in the fabric structure than fabrics sewn with 4-hole buttons. Moreover, in 4-hole buttons, the number of connection points between button and fabric is twice as higher than 2-hole buttons. The higher the number of connections between fabric and button, the higher the breaking strength.

- When the strength values of buttons made of different materials owing the same diameter are studied, it is found that wooden buttons have the lowest strength values. Moreover, the material type is not statistically significant.

- It is noted that the fabric plays a significant role in the breaking strength of the buttons. The fabric with a higher weight and tighter structure has a higher strength.

- The sewing thread count used in button sewing has a significant effect on the breaking strength of the button. As the thread count (tex) increases, the breaking strength values also increase.

The results indicate that the breaking strength of buttons is related to the number of holes in the button, the size of the sewing thread and the type of fabric. Therefore, this result can be considered in the selection of buttons according to their aesthetic or functional properties.

According to the literature review, there is no specific study on the strength properties of buttons. In future studies, the scope of the work can be further expanded by using a different number of fabrics and sewing threads. This study will lead the way in conducting studies to investigate the properties of buttons.

Acknowledgement

REFERENCES

1. Chatterjee KN, Jhanji Y, Grover T, Bansal N, Bhattacharyya S. 2015. Selecting garment accessories, trims, and closures. In R. Nayak, R. Padhye (Ed.), *Garment manufacturing technology*. Woodhead Publishing Series in Textiles, 129-177.

2. Gupta D. 2011. Design and engineering of functional clothing. *Indian Journal of Fibre&Textile Research* 36, 327-335.

3. Solinger J. 1980. *Apparel manufacturing handbook.* Van Nostrand Reinhold Company, 795p.

4. Bilen U. 2013. *Materials and accessories used in ready-to-wear.* İstanbul: Kerasus Kitap.

5. Tyler DJ. 2008. *Carr and Latham's technology of clothing manufacture*. Blackwell Publishing.

6. Kurumer G. 2007. *Apparel production and technology*. İzmir: Printer Ofset Matbaacılık, 446s.

7. Yıldız EZ, Süpüren Mengüç G, Özdil N, Pamuk O. 2019, April. Buttons used in apparel products and their performance tests. ERASMUS International Academic Research Symposium in Science, Engineering and Architecture (353-365). Izmir, Turkey.

8. Pamuk O, Yıldız EZ. 2013. The effect of chain width on the strength of the metallic slide fasteners. *Tekstil ve Konfeksiyon* 23(2), 290-296.

9. Umaru S. Kaisan MU, Usman S, Giwa A. 2016. Effect of garment laundry activities on the slider lock and crosswise strengths of nylon coil zippers. *Nigerian Journal of Materials Science and Engineering* 7(1), 81-86.

10. Bahadır Ünal Z, Acar E, Yıldırım F. 2015. Evaluating performance characteristics of lining fabrics used for children dresses. *Tekstil ve Konfeksiyon* 25(4), 323-328.

11. Punitha V, Ajaykarthi AG, Saravanasastha J, Srinivasan M. 2021. The mechanical properties of warp knitted lining fabrics used for sportswear. *International Journal of Recent Advances in Multidisciplinary Topics* 2(6), 85-87.

12. Rudolf A, Gersak J, Ujhelyiova A, Sfiligoj Smole M. 2007. Study of PES sewing thread properties. *Fibers and Polymers* 8(2), 212-217.

13. Eryürük SH, Kalaoğlu F. The effects of different amounts of lubricant application on the sewing thread performance properties. *Textile Research Journal* 80(12), 1232-1242.

14. Ajiki I, Postle R. 2003. Viscoelastic properties of threads before and after sewing. *International Journal of Clothing Science and Technology* 15(1), 16-27.

15. Zhang Q, Kan CW. 2018. A review of fusible interlinings usage in garment manufacture. *Polymers* 10(11), 1230.

16. Yıldız EZ, Özdil N. 2014. Subjective and objective evaluation of the handle properties of shirt fabric fused with different woven interlinings. *Tekstil ve Konfeksiyon* 24(1), 47-55.

The Effect of Rib Fabric Pattern and Yarn Composition on the Mechanical Properties of Polyester Matrix Composites Reinforced by Weft-Knitted Fabric

Mehmet Erdem İnce[1] 0000-0001-7537-9172
Halil İbrahim İçoğlu[2] 0000-0003-0687-4721

[1]Gaziantep University / Textile Engineering Department / Şehitkamil, Gaziantep, Türkiye
[2]Gaziantep University / Metallurgical and Materials Engineering / Şehitkamil, Gaziantep, Türkiye

Corresponding Author: Mehmet Erdem İnce, eince@gantep.edu.tr, meince@ncsu.edu

ABSTRACT

In this study, polyester matrix composites reinforced by 1x1, 2x2, half- and full-cardigan rib pattern weft-knitted fabrics from glass and glass/aramid hybrid yarns were produced. Physical properties such as thickness and volumetric density were determined. Tensile, flexural and low velocity impact tests were applied to the composite samples. The 2x2 rib pattern composite showed the highest thickness and density. The hybridization of glass yarn with aramid yarn increased the thickness, while it decreased the density of composites. The 2x2 rib pattern composite showed the highest tensile modulus and tensile strength. Yarn hybridization increased tensile strength at statistically significant level. The composite with full-cardigan rib pattern displayed considerably higher flexural modulus and flexural strength than the composites with the other patterns. When glass and hybrid composites were considered separately, the rib fabric pattern exhibited significant effect on maximum load. The rib fabric pattern displayed also significant effect on absorbed energy for glass composites. The yarn hybridization dramatically increased maximum load and absorbed impact energy. Rib fabric pattern and yarn composition variables displayed the parallel effect on bursting strength of the soft knitted fabrics and maxium impact load of the composites.

1. INTRODUCTION

Today's modern industries demand lightweight, stiff, strong, corrosion-, and impact-resistant products. However, it is a big challenge to meet all these requirements using a single type of material. This expanded the use of composite materials that contain at least two different material types in their structures. In fiberglass - a typical example of composite materials - short glass fibers (aka reinforcement) that stiffen and strengthen the composite structure are embedded in polyester matrix that enhances the ductility and reduces the density of the whole body [1-3].

Heat resistant, durable, ductile and lightweight aramid fibers that have a high level of energy absorption capacity are used to produce protective soft fabrics or to reinforce polymers. Due to their more flexible structure as compared with glass and carbon fibers, aramid fibers are more easily transformed into weft knitted fabrics with less fiber damage. However, the use of expensive aramid fibers alone in fabric production increases the cost. Converting aramid fibers together with cheaper glass fibers into hybrid fabric is expected to modify mechanical properties without increasing the cost too much.

Due to their integrated structure containing interlaced yarns, textile reinforcement fabrics resist and show tolerance against impact damage more than the unidirectional prepregs do [4-7]. The complex internal structure of weft knitted fabrics that can be rapidly produced with low cost and consisting of interlocked loops makes them different from other reinforcements. Thanks to their porous, flexible and stretchable structure, 3D monolithic preforms can be shaped from these fabrics

without any wrinkle, folding and rupture. As a result of easy to compress and nesting capability of the layers, the composites from weft knitted fabrics keep the impact damage within a limited area and absorb high level energy without delaminations [8-10]. However, their low fiber contents without a specific direction reduce their in-plane load carrying capabilities. This disadvantage can be eliminated using different types of stitches (tuck, skip stitches) and inlay yarns in the course or wale directions [11-15]. Weft knitting needles that can form plain, tuck or skip stitches in different sizes enable to obtain numerous fabric patterns. The literature review shows that the mechanical properties of weft knitted fabric reinforced composites can be designed by the fabric pattern.

De Araújo et al. investigated the effect of fabric pattern (single jersey, 1x1 jersey and fleece) on tensile properties of weft knitted glass fabrics and the composites reinforced by these fabrics [16]. They concluded that the introduction of tuck and skip stitches increased the strength, while it reduced the elongation of both dry fabric and the composite. They also reported that pre-tension of the fabric before composite production improved the tensile properties. Soyaslan investigated the effect of fabric pattern on electromagnetic shielding performance of the composites and reported that fabric pattern had important role on EMSE of the composites [17]. Alpyildiz et al. studied the composites from the weft knitted glass fabrics with 1x1 rib and full cardigan derivative patterns [18]. Tuck stitches enabled the full cardigan derivative composite – containing more fibers – to exhibit more isotropic behavior, higher course-direction tensile strength, greater impact performance with more limited damage area, and better compression-after-impact properties.

Pamuk produced composites reinforced by the weft-knitted spacer fabrics from various yarns; and stated that the composite from double tuck stitched fabric displayed superior impact resistance than the composite from the single tuck stitched fabric [19]. Abounaim et al. stated that the tuck stitch formation in weft-knitted spacer fabrics

caused less yarn strength loss than the plain stitch formation, and the dry fabric with tuck stitches exhibited the same course-direction tensile strength as the fabric with inlay yarns did [20]. Similarly, they noted that the tuck stitched composite exhibited higher tensile, bending and impact strength than the plain stitched composite, and approached the weft-inlay yarn composite in terms of impact strength.

In this study, firstly weft-knitted fabrics were manufactured at four different rib fabric pattern (1x1, 2x2, half- and full-cardigan) with glass and glass/aramid hybrid yarns. Secondly, these fabrics converted into polyester matrix composites via vacuum infusion process. Thereafter, the effect of rib fabric pattern and yarn composition on physical (thickness and density) and mechanical properties (tensile, flexural and impact) were investigated.

2. MATERIAL AND METHOD

2.1 Material

In this study, 136 tex multifilament E-glass yarn with 9 µm filament diameter and 1500 denier multifilament aramid yarn (m-aramid, Dupont) were used for fabric production. Unsaturated polyester resin (CE 92), MEKP (initiator), and 6% Cobalt Naphtanate (promoter) were used for composite production.

2.2 Fabric and composite production

The manual double bed weft knitting machine (Brother KH-864) with a fineness of 5E was used to produce the knit fabrics in 1x1, 2x2, half- and full-cardigan rib patterns. Both 3-ply glass yarns and 2-ply glass/1-ply aramid yarns were used for each rib fabric pattern. Totally 8 different knit fabric samples were produced (Figure 1). The constructional properties of the knitted fabrics and fiber weight percentages of the composite plates are given in Table 1.
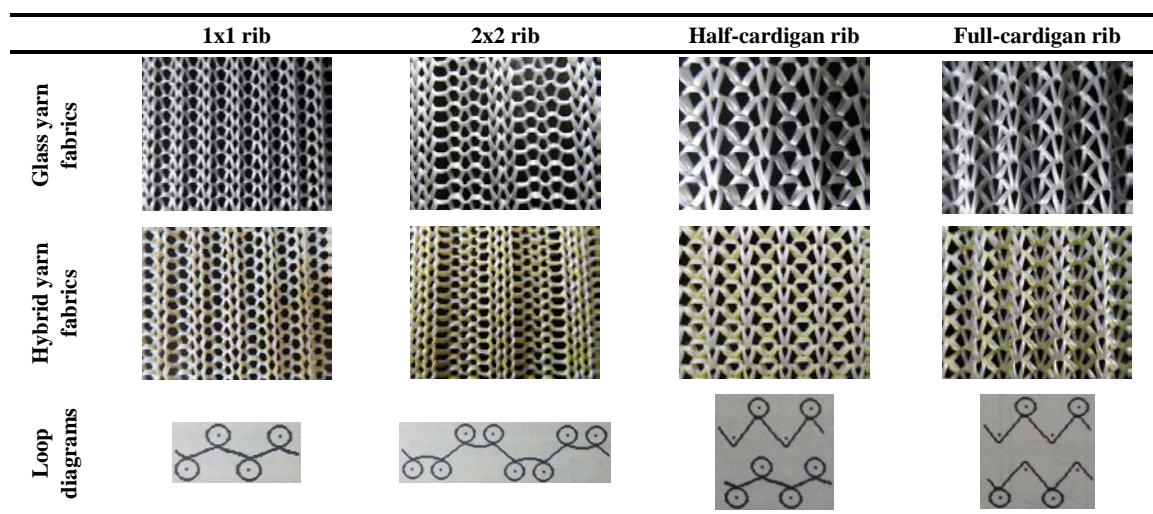

Figure 1. The photographs of the knit fabrics and loop diagrams

Table 1. Constructional properties of the knitted fabrics and fiber weight percent of the composite plates

Yarn composition	Rib fabric pattern	Thickness [mm]	Wale density [#/cm]	Course density [#/cm]	Areal density [g/m²]	Fiber weight percent of conposite [%]
Glass	2x2	2.08	10.4	4.6	1178	60.3
	Full-cardigan	2.18	11.5	3.8	1157	70.1
	1x1	1.44	4.06	2.6	708	48.2
	Half-cardigan	1.56	5.2	4.0	792	55.7
Hybrid	2x2	3.07	7.6	4.6	1142	40.7
	Full-cardigan	3.23	10.2	3.6	1112	46.6
	1x1	2.66	4.8	2.9	857	43.6
	Half-cardigan	2.62	5.4	4.0	889	44.4

Each composite panel was produced from 2-layer fabrics with the same rib fabric pattern and the yarn composition via vacuum infusion composite production technique. Two-layer dry knitted fabrics were placed in stretched form over the waxed glass table, then the top surface of the fabric stack was covered with peel ply fabric and infusion mesh, respectively. Thereafter, spiral tubes were placed over edges of resin inlet and outlet lines. The overall stack was sealed by vacuum bag using tacky tape along the periemeter of the stuck. The air under the vacuum bag was completely evacuated by the vacuum pump that was connected to spiral tube at the resin outlet. Resin propagated through the spiral tube at the resin inlet and wetted the complete stack upto resin outlet. 24 hours were waited at room temperature for complete curing of the resin. The vacuum infusion set up for the composite production with the composite panel specimens was given in Figure 2. Test specimens for physical and mechanical tests were cut via CNC router according to the related standards.

2.3 Physical tests

Thickness, width and length of the specimens were measured by digital calliper. The weights of the specimens were measured by a precision scale. The density of the specimens was calculated as weight over volume.

2.4 Mechanical tests

Tensile and three-point bending tests were performed on Shimadzu Universal Tester with a load cell capacity of 300 kN. Tensile test were applied on dog-bone shaped specimens according to ASTM D3039. Three-point bending tests were applied according to ASTM D790. Low velocity drop tower impact test was performed on Besmak BMT-2000DW impact tester. Impact energy level was adjusted as 25 J. Also, the soft reinforcement knitted fabrics were subjected to bursting strength on SDL Atlas M229 hydraulic bursting tester according to BS EN ISO 13938-1.

The average of five bursting strength measurements was calculated for each different soft fabric.

2.5 Statistical analysis

The tests' results were subjected to statistical analysis of variance (ANOVA) and Tukey-Kramer test to assess the effects of rib fabric pattern and yarn composition on the physical and mechanical properties of the composites using Jump statistical software (JMP the latest trial version). Data analysis was supported by visual and self-explanatory graphs. The results were considered significant at $p \leq 0.05$.

3. RESULTS AND DISCUSSION

3.1 Physical test results

The effect of rib fabric pattern on thickness and density of the composite samples were given in Figure 3 and Table 2. The 2x2 rib pattern showed the highest thickness and density. It can be related to fabric tightness. The dramatic narrowing in the width of the 2x2 rib pattern due to internal tension stemming from consecutive binary placement of loop bars from face and back plain stitches created a tight fabric structure. Also higher thickness and density values of full-cardigan rib pattern could be arisen from the tuck stitches on both sides, which cause tight fabric structure. Although full cardigan rib pattern had the highest thickness in fabric form (Table 1), 2x2 rib pattern in composite form displayed the highest thickness. This can be related to higher inter-layer nesting tendency of soft-touch full cardigan rib pattern fabric as compared with that of hard-touch 2x2 rib pattern fabric, where two-layer fabric in composite production was considered. Half-cardigan rib pattern showed the lowest thickness and density due to its loose structure with low fabric internal tension. The effect of rib fabric pattern on thickness and density of the composite samples was statistically significant ($p < 0.05$).

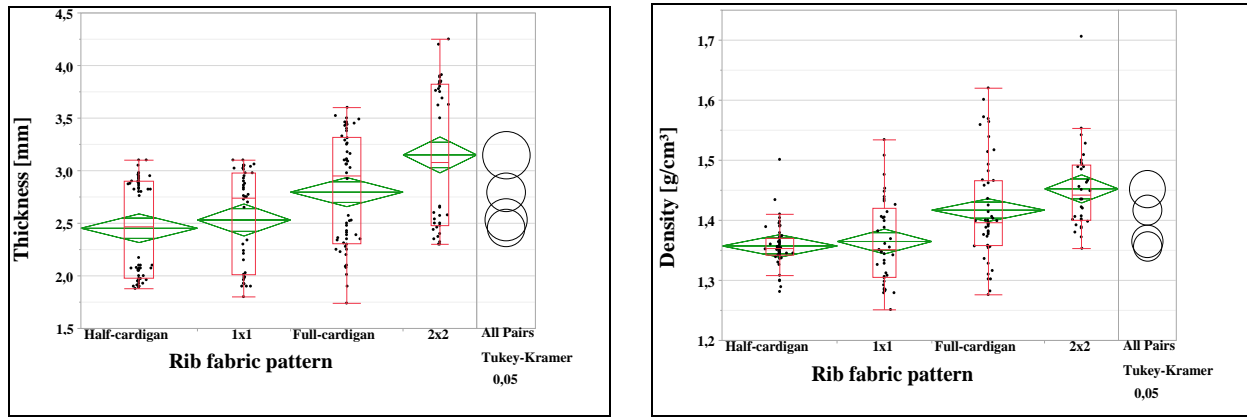**Figure 2.** The composite production via vacuum infusion (left), the composite panel specimens (right)

Figure 3. Effect of rib fabric pattern on thickness (left) and density (right) of the composite

Notes: The distance between top and bottom ends of green diamond represents the 95% confidence interval. Comparison circles (given on the right column) for means those are significantly different either do not intersect, or intersect slightly. The height of red box (known as interquartile range) is a quantitative indication of variation.

Table 2. Effect of rib fabric pattern on thickness and density of the composite

Property	Rib fabric pattern				n	Mean	SD	LL	UL	p-value
Thickness [mm]	2x2	A			38	3.15	0.70	2.92	3.38	< 0.0001
	Full-cardigan		B		58	2.80	0.54	2.66	2.94	
	1x1		B	C	48	2.53	0.46	2.40	2.67	
	Half-cardigan			C	60	2.45	0.46	2.33	2.57	
Density [g/cm³]	2x2	A			32	1.45	0.07	1.43	1.48	< 0.0001
	Full-cardigan	A			49	1.42	0.08	1.39	1.44	
	1x1		B		41	1.36	0.07	1.34	1.39	
	Half-cardigan		B		50	1.36	0.04	1.35	1.37	

Note: Sub-levels of a variable are classified by alphabetical capital letters (e.g. A, B, C). The sub-levels not connected by the same alphabetical capital letter are significantly different from each other at significance level of 0.05. n:number of observations, SD: standard deviation, LL: lower limit, UL: upper limit. Limits are based on a confidence level of 95%.

The effect of yarn composition on thickness and density of the composite samples were given in Figure 4 and Table 3. Replacing the third glass yarn ply with the aramid yarn ply (i.e. yarn hybridization) increased the thickness, while it decreased the density of composites. These can be related to higher yarn count (1500 denier ≈ 167 tex) and lower raw material density (ρ=1.44 g/cm³) of aramid yarn. The effect of yarn composition on thickness and density of the composite samples was statistically significant (p<0.05).
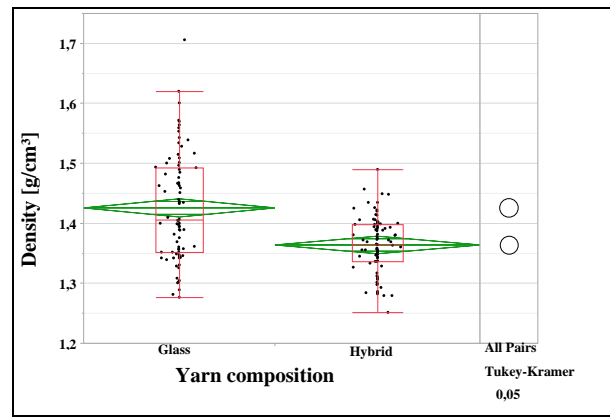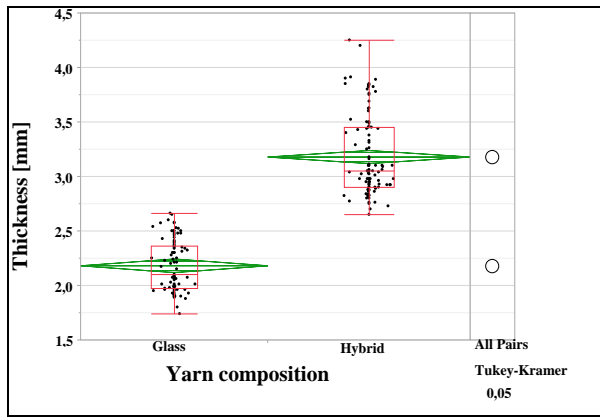
Figure 4. Effect of yarn composition on thickness (left) and density (right) of the composite samples

Table 3. Effect of yarn composition on thickness and density of the composite samples

Property	Yarn Composition			n	Mean	SD	LL	UL	p-value
Thickness	Hybrid	A		106	3.18	0.37	3.11	3.25	< 0.0001
[mm]	Glass		B	98	2.18	0.23	2.13	2.23	
Density	Hybrid	A		83	1.43	0.09	1.41	1.44	< 0.0001
[g/cm³]	Glass		B	89	1.36	0.05	1.35	1.37	

3.2 Tensile test results

The effect of rib fabric pattern on tensile modulus and strength of the composite samples were given in Figure 5 and Table 4. The 2x2 rib pattern composite showed the highest tensile modulus and strength. This can be related to physical properties of 2x2 rib pattern composite which has the highest thickness and density values. Similarly, inferior physical properties of half-cardigan rib pattern composite are responsible for the lowest tensile modulus and strength. Likewise, a positive correlation between physical properties (tightness) and tensile was detected [21]. The effect of rib fabric pattern on tensile modulus and strength of the composite samples was statistically significant ($p < 0.05$).
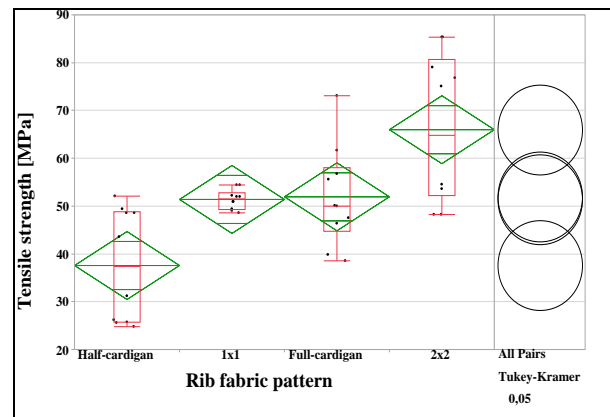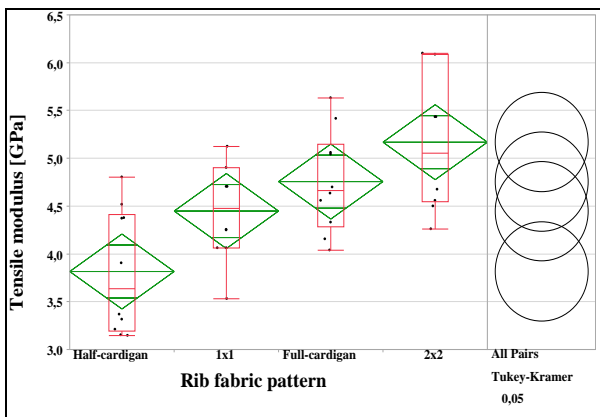
Figure 5. Effect of rib fabric pattern on tensile modulus (left) and strength (right) of the composite samples

Table 4. Effect of rib fabric pattern on tensile modulus and strength of the composite samples

Property	Rib fabric pattern				n	Mean	SD	LL	UL	p-value
Tensile Modulus [GPa]	2x2	A			10	5.17	0.74	4.64	5.70	0.0002
	Full-cardigan	A			10	4.76	0.53	4.38	5.13	
	1x1	A	B		10	4.45	0.50	4.09	4.80	
	Half-cardigan		B		10	3.82	0.65	3.35	4.28	
Tensile Stregth [MPa]	2x2	A			10	65.98	15.58	54.83	77.13	0.0002
	Full-cardigan		B		10	51.94	10.33	44.56	59.33	
	1x1		B		10	51.39	2.02	49.94	52.84	
	Half-cardigan			C	10	37.57	11.75	29.16	45.98	

The effect of yarn composition on tensile modulus and strength of the composite samples were given in Figure 6 and Table 5. Yarn hybridization generally decreased tensile modulus at statistically non-significant level (p = 0.1012), while it increased tensile strength at statistically significant level (p = 0.0006). Aramid yarns are more ductile than glass yarns, which plays role on lower tensile modulus. On the other hand, higher tensile strength of hybrid composites results from higher tensile strength of aramid yarn than that of glass yarn.

3.3 Flexural test results

The effect of rib fabric pattern on flexural modulus and strength of the composite samples were given in Figure 7 and Table 6. The full-cardigan rib pattern composite showed the highest flexural modulus and strength. The other fabric patterns' composites showed similar results. This significant differnce on flexural modulus and strength of the full-cardigan rib pattern composite can be related with presence of tuck stitches on both faces of that pattern. Because, tuck stiches increase fiber content per unit volume of knit fabrics [18-20]. The effect of rib fabric pattern on flexural modulus and strength of the composite samples was statistically significant (p<0.05).

The effect of yarn composition on flexural modulus and strength of the composite samples were given in Figure 8 and Table 7. Yarn hybridization decreased flexural modulus at statistically non-significant level, while it didn't change flexural strength. Lower flexural modulus of the hybrid composite is related to higher deformability of aramid yarns than glass yarns.
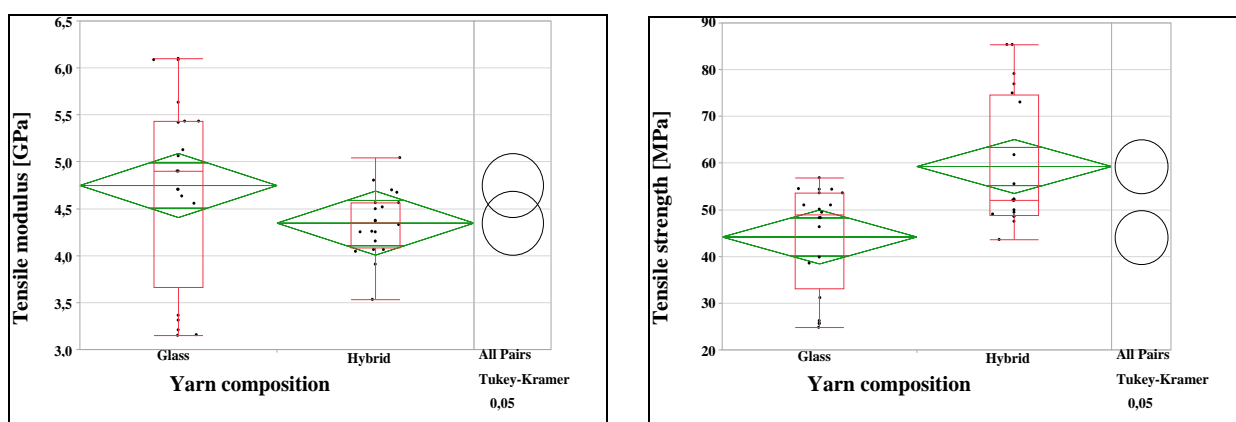
Figure 6. Effect of yarn composition on tensile modulus (left) and strength (right) of the composite samples
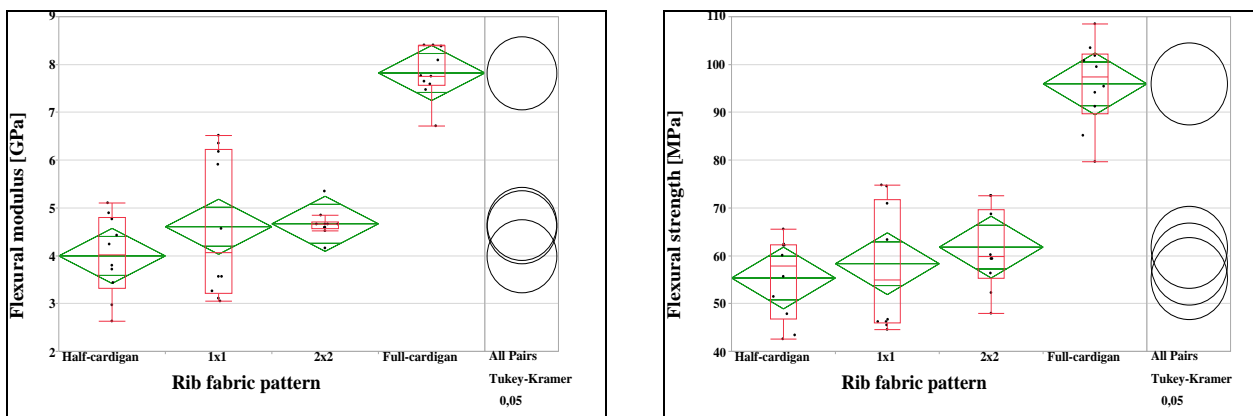
Figure 7. Effect of rib fabric pattern on flexural modulus (left) and strength (right) of the composite samples

Table 5. Effect of yarn composition on tensile modulus and strength of the composite samples

Property	Yarn composition		n	Mean	SD	LL	UL	p-value
Tensile Modulus [GPa]	Glass	A	20	4.75	1.01	4.28	5.22	0.1012
	Hybrid	A	20	4.35	0.34	4.19	4.51	
Tensile Stregth [MPa]	Glass	A	20	59.27	14.03	52.70	65.83	0.0006
	Hybrid	B	20	44.18	11.34	38.87	49.48	

Table 6. Effect of rib fabric pattern on flexural modulus and strength of the composite samples

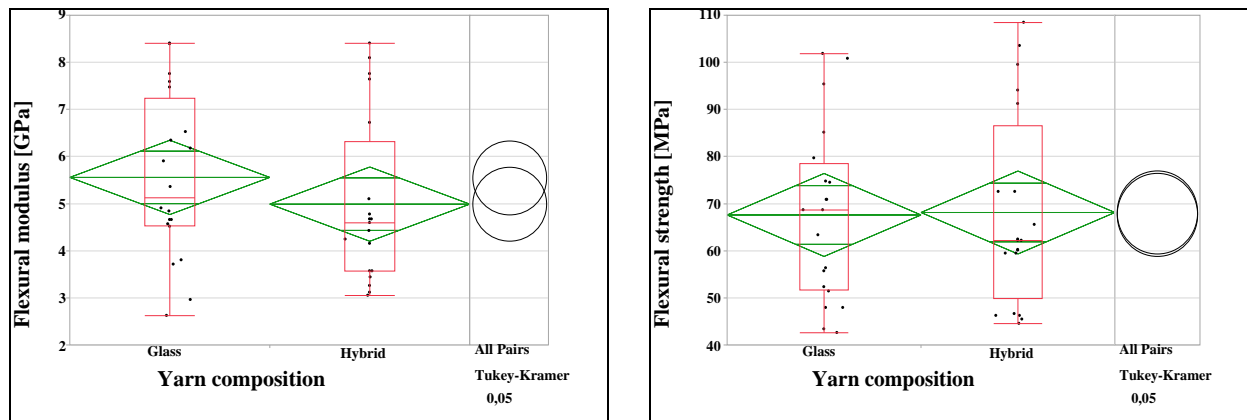| Property	Rib fabric pattern		n	Mean	SD	LL	UL	p-value
Flexural Modulus [GPa]	Full-cardigan	A	10	7.82	0.53	7.44	8.20	
	2x2	B	10	4.67	0.30	4.46	4.88	< 0.0001
	1x1	B	10	4.61	1.47	3.55	5.66	
	Half-cardigan	B	10	4.00	0.83	3.40	4.59	
Flexural Strength [MPa]	Full-cardigan	A	10	95.96	8.77	89.68	102.23	
	2x2	B	10	61.80	8.53	55.70	67.91	< 0.0001
	1x1	B	10	58.33	13.58	48.62	68.05	
	Half-cardigan	B	10	55.34	8.49	49.27	61.42	

Figure 8. Effect of yarn composition on flexural modulus (left) and strength (right) of the composite samples

Table 7. Effect of rib fabric pattern on flexural modulus and strength of the composite samples

Property	Yarn composition		n	Mean	SD	LL	UL	p-value
Flexural Modulus [GPa]	Glass	A	20	5.56	1.74	4.74	6.37	0.1547
	Hybrid	A	20	4.99	1.75	4.17	5.81	
Flexural Stregth [MPa]	Glass	A	20	67.60	18.34	59.01	76.18	0.4662
	Hybrid	A	20	68.12	20.52	58.52	77.72	

3.4 Impact test results

The effect of rib fabric pattern on maximum load and absorbed energy at maximum load of the composite samples were given in Figure 9 and Table 8. When all composite samples were evaluated, there was no statistically significant effect of rib fabric pattern on maximum load and absorbed energy. The data at the bottom legs of the box plots belong to glass composites, while those at the top legs of the box plots belong to hybrid composites on Figure 9. Thus, when glass and hybrid composites were considered separately, the rib fabric pattern showed significant effect on maximum load (p-values of 0.0006 and <0.0001, respectively). This can be related to higher physical properties (thickness and density) of 2x2 and full-cardigan rib pattern composites. Furthermore, the rib fabric pattern showed significant effect on absorbed energy for glass composites (p<0.0001), while it showed negligible effect for hybrid composites. The reason of non-significant effect of rib fabric pattern on absorbed energy for hybrid composites can be related to

superior ductility of aramid yarns. On the other hand rib fabric pattern played a significant role on absorbed energy for glass composites due to brittle nature of glass yarns.

The effect of yarn composition on maximum load and absorbed energy of the composite samples were given in Figure 10 and Table 9. Yarn hybridization increased maximum load and absorbed energy at statistically significant level. This result can be linked to higher tensile strength and ductility of aramid yarns as compared with glass yarns. The photographs of the composite specimens after the impact test were given in Figure 11.

To reveal the relationship between impact performance of the composites and bursting strength of the soft knitted reinforcements, the bursting strength of the soft fabrics were measured. The results were given in Table 10. Rib fabric pattern and yarn composition factors exhibited the similar effect on maxium impact load of the composites and bursting strength of the soft knitted fabrics. Rib fabric pattern modified the bursting strength of glass and hybrid

soft fabrics separately. 2x2 rib fabric pattern displays the highest bursting strength values. This may be related to the compact and thick fabric structure of 2x2 rib pattern. Similar to the impact performance of the composites, hybrid soft knitted fabrics showed higher bursting strength values than glass ones. This can be attributed to higher tensile strength of aramid yarns than glass yarns.
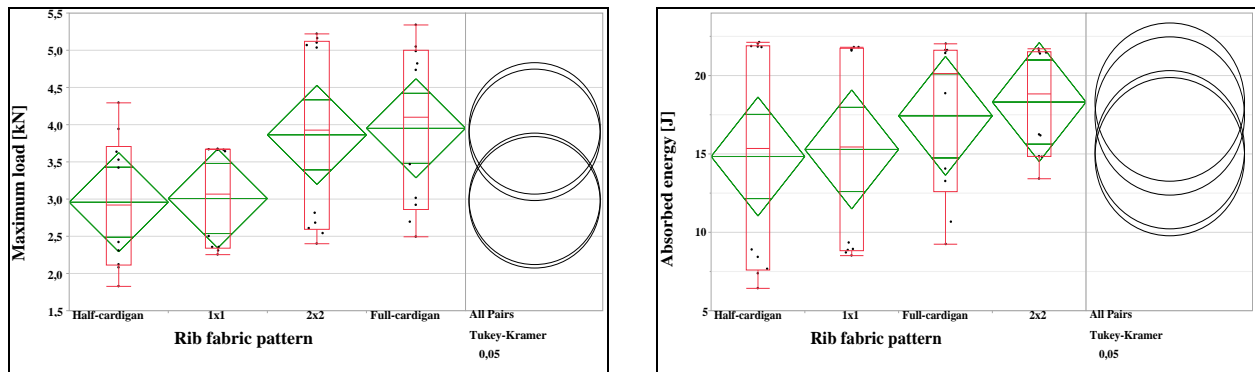
Figure 9. Effect of rib fabric pattern on maximum load (left) and absorbed energy (right) of the composite samples
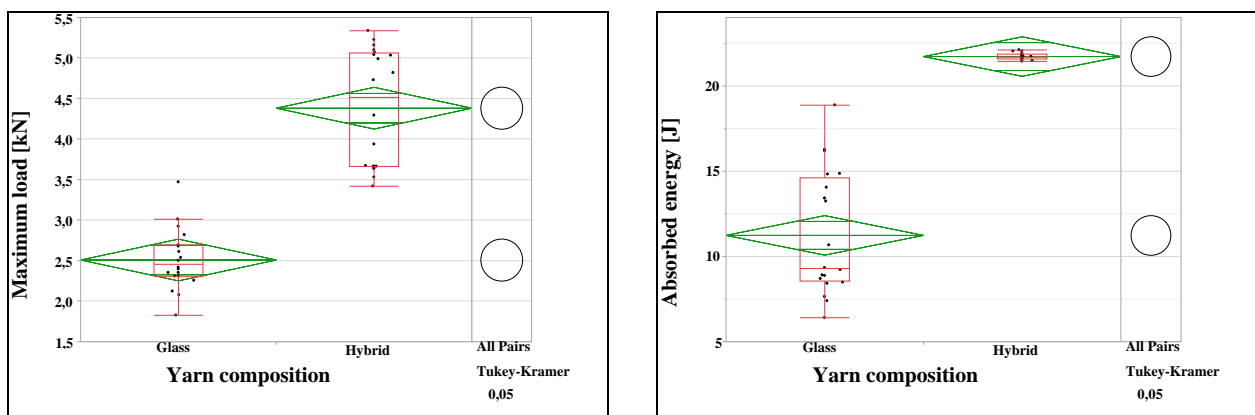
Figure 10. Effect of yarn composition on maximum load (left) and absorbed energy (right) of the composite samples

Table 8. Effect of rib fabric pattern on maximum load and absorbed energy of the composite samples

Property	Rib fabric pattern		n	Mean	SD	LL	UL	p-value
	Full-cardigan	A	10	3.95	1.13	3.15	4.76	
Maximum Load [kN]	2x2	A	10	3.86	1.33	2.91	4.81	0.0629
	1x1	A	10	3.01	0.69	2.51	3.50	
	Half-cardigan	A	10	2.96	0.90	2.32	3.60	
	2x2	A	10	18.32	3.48	15.83	20.81	
Absorbed Energy [J]	Full-cardigan	A	10	17.44	5.10	13.79	21.08	0.5039
	1x1	A	10	15.29	6.78	10.44	20.14	
	Half-cardigan	A	10	14.84	7.51	9.47	20.21	

Table 9. Effect of yarn composition on maximum load and absorbed energy of the composite samples

Property	Yarn composition			n	Mean	SD	LL	UL	p-value
Maximum Load [kN]	Hybrid	A		20	4.38	0.72	4.06	4.72	< 0.0001
	Glass		B	20	2.51	0.36	2.34	2.68	
Absorbed Energy [J]	Hybrid	A		20	21.71	0.20	21.62	21.81	< 0.0001
	Glass		B	20	11.23	3.61	9.54	12.92	
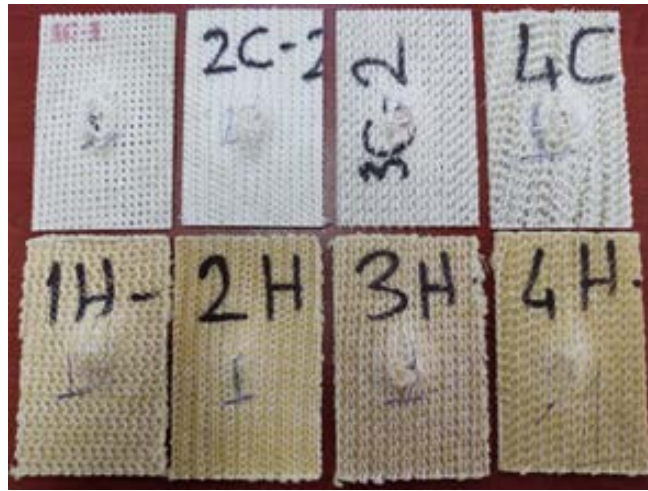
Figure 11. The photographs of the composite specimens after the impact test. a) 1x1 rib glass, b) 2x2 rib glass, c) half-cardigan rib glass, d) full-cardigan rib glass, e) 1x1 rib hybrid, b) 2x2 rib 1x1 rib hybrid, c) half-cardigan rib 1x1 rib hybrid, d) full-cardigan rib 1x1 rib hybrid

4. CONCLUSION

The effect of rib fabric pattern and yarn composition on physical and mechanical properties of composite samples was investigated in this study. The 2x2 rib pattern showed the highest thickness and density. Yarn hybridization increased the thickness, while it decreased the density of composites. The 2x2 rib pattern composite showed the highest tensile properties. Yarn hybridization generally decreased tensile modulus at statistically non-significant level, while it increased tensile strength at statistically significant level. The full-cardigan rib pattern composite showed the highest flexural modulus and strength. The other fabric patterns' composites showed similar flexural results. When glass and hybrid composites were considered separately, the rib fabric pattern exhibited significant effect on maximum load. The rib fabric pattern displayed also significant effect on absorbed energy for glass composites, while no significant effect was detected for hybrid composites. Yarn hybridization increased maximum load and absorbed energy at statistically significant level. The effects of rib fabric pattern and yarn composition on bursting strength of the soft knitted fabrics were similar to those of maxium impact load of the composites.

Table 10. Bursting strength test results of the soft knitted reinforcements

Yarn composition	Rib fabric pattern	Bursting strength [kPa]	Distension [mm]
Glass	2x2	1665	20,7
	Full-cardigan	1294	23
	1x1	1319	22
	Half-cardigan	1329	26
Hybrid	2x2	4308	21,4
	Full-cardigan	3824	22,4
	1x1	3401	21,8
	Half-cardigan	3688	22

Acknowledgement

REFERENCES

1. Callister WD, Rethwisch DG. 2018. *Materials science and engineering: an introduction* (Vol. 9). New York: Wiley.

2. Campbell F C. 2003. *Manufacturing processes for advanced composites*. Oxford: Elsevier.

3. Strong AB. 2008. *Fundamentals of composites manufacturing: materials, methods and applications*. Michigan: Society of manufacturing engineers.

4. Hearle JWS, Du GW. 1990. Forming rigid fibre assemblies: the interaction of textile technology and composites engineering. *Journal of the Textile Institute*, 81(4), 360-383.

5. Cox BN, Flanagan G. 1997. *Handbook of analytical methods for textile composites*. Virginia: NASA.

6. Dow MB, Dexter HB. 1997. *Development of stitched, braided and woven composite structures in the ACT program and at Langley Research Center*. Virginia: NASA.

7. Wambua PA, Anandjiwala R. 2011. A review of preforms for the composites industry. *Journal of Industrial Textiles*, 40(4), 310-333.

8. Pandita SD, Falconet D, Verpoest I. 2002. Impact properties of weft knitted fabric reinforced composites. *Composites Science and Technology*, 62(7-8), 1113-1123.

9. Khondker OA, Leong KH, Herszberg I, Hamada H. 2005. Impact and compression-after-impact performance of weft-knitted glass textile composites. *Composites Part A: Applied Science and Manufacturing*, 36(5), 638-648.

10. Tercan M, Asi O, Yüksekkaya ME, Aktaş A. 2007. Comparison of tensile properties of weft-knit 1× 1 rib glass/epoxy composites with a different location of layers. *Materials & Design*, 28(7), 2172-2176.

11. Gommers B, Verpoest I, Van Houtte P. 1996. Modelling the elastic properties of knitted-fabric-reinforced composites. *Composites Science and Technology*, 56(6), 685-694.

12. Pamuk G, Çeken F. 2008. Manufacturing of weft-knitted fabric reinforced composite materials: a review. *Materials and Manufacturing Processes*, 23(7), 635-640.

13. Padaki NV, Alagirusamy R, Deopura BL, Fangueiro R. 2010. Influence of preform interlacement on the low velocity impact behavior of multilayer textile composites. *Journal of Industrial Textiles*, 40(2), 171-185.

14. Ciobanu L. 2011. Development of 3D knitted fabrics for advanced composite materials. *In Advances in Composite Materials-Ecodesign and Analysis*. IntechOpen, 161-192.

15. Karaoglu I., Alpyildiz T. 2021. Impact performances of monoaxial knitted fabric composites. *Journal of Composite Materials*, 0021998320988877.

16. Araujo MD, Fangueiro R, Hong H. 2003. Modelling and simulation of the mechanical behaviour of weft-knitted fabrics for technical applications: part I: general considerations and experimental analyses. *AUTEX Research Journal*, 3, 111-123.

17. Soyaslan DD. 2020. Design and manufacturing of fabric reinforced electromagnetic shielding composite materials. *Tekstil ve Konfeksiyon*, 30(2), 92-98.

18. Alpyildiz T, Icten BM, Karakuzu R, Kurbak A. 2009. The effect of tuck stitches on the mechanical performance of knitted fabric reinforced composites. *Composite Structures*, 89(3), 391-398.

19. Pamuk G, Ceken F. 2013. Comparison of the mechanical behavior spacer knit cotton and flax fabric reinforced composites. *Industria Textila*, 64(1), 3-7.

20. Abounaim M, Hoffmann G, Diestel O, Cherif C. 2010. Thermoplastic composite from innovative flat knitted 3D multi-layer spacer fabric using hybrid yarn and the study of 2D mechanical properties. *Composites Science and Technology*, 70(2), 363-370.

21. Asi O, Aktaş A, Tercan M, Yüksekkaya ME. 2010. Effect of knitting tightness on mechanical properties of weft-knit glass fiber reinforced epoxy composites. *Journal of Reinforced Plastics and Composites*, 29(1), 86-93.

A Novel Industrial Application of CNN Approach: Real Time Fabric Inspection and Defect Classification on Circular Knitting Machine

Halil İbrahim Çelik[1*] [ID] 0000-0002-1145-6471
Lale Canan Dülger[2] [ID] 0000-0002-1167-1737
Burak Öztaş[3] [ID] 0000-0002-8789-155X
Mehmet Kertmen[4] [ID] 0000-0003-1661-7219
Elif Gültekin[1] [ID] 0000-0003-4910-4081

[1] Gaziantep University, Department of Textile Engineering, Gaziantep, Türkiye
[2] Izmir University of Economics, Department of Mechanical Engineering, Izmir, Türkiye
[3] Kahramanmaraş Sütçü Imam University, Department of Textile Engineering, Kahramanmaraş, Türkiye
[4] İskur Tekstil Enerji Tic. ve San. A.Ş. Kahramanmaraş, Türkiye

Corresponding Author: Halil İbrahim Çelik, hcelik@gantep.edu.tr

ABSTRACT

Fabric Automatic Visual Inspection (FAVI) system provides reliable performance on fabric defects inspection. This study presents a machine vision system developed to adapt in circular knitting machines where fabric defects can be automatically controlled and detected defects can be classified. The knitted fabric surface are detected during real-time manufacturing. For the classification process, three different transfer learning architectures (ResNet-50, AlexNet, GoogLeNet) have been applied. The five common knitted fabric defects were recognized with the artificial intelligence-based software and classified with an average success rate of 98% using ResNet-50 architecture. The success rates of the trained networks were compared.

1. INTRODUCTION

The knowledge of human brain, statistics and applied mathematics is needed to machine learning based on deep learning that has seen tremendous growth in its popularity and usefulness. Luckily these are achieved by using powerful computers, larger datasets and techniques used to train networks. Challenges and opportunities are ready to improve deep learning even further in coming years [1]. Dramatic improvements have been seen in computer vision; medical image analysis, text analysis, speech recognition, computer games, cyber security for example. The evolution of neural networks with more neurons, connecting layers/neurons in different way and automatic feature extraction are interpreted with deep learning resulting in more computing power indeed [2].

Developments in Industry 4.0 have incorporated concepts and technologies such as the internet of things, artificial intelligence, and smart factories into our lives. Especially as use of artificial intelligence and computer vision technologies together, different methods are developed using smart vision systems instead of production stages and quality control processes that are followed, controlled, and decided by humans. Considering the production process in

To cite this article: Çelik Hİ, Dülger LC, Öztaş B, Kertmen M, Gültekin E. 2022. A novel industrial application of cnn approach: real time fabric inspection and defect classification on circular knitting machine. *Tekstil ve Konfeksiyon*, 32(4), 344-352.

the textile sector, both in production stages and post-production quality evaluations are mostly decided by human monitoring and evaluation by following a labour-intensive method.

In the current technology, fabric defects are checked by the workers on the illuminated surface after production. The fabric structure can be composed with different methods such as knitting, weaving and the nonwoven texture property. Considering the knitting fabric production, common defects are seen such as hole/cracks, loops/drop stitches, lycra missing, knots [3-7]. These defect types are defined on the knitted fabric roll after production prosess. Improvements on defect detection technology reduces production cost by also improving product quality. Many attempts have been performed to automatically perform this process. Different systems and algorithm parameters must be used for each fabric formation method.

Many studies have been found using image processing techniques such as histogram-based, color-based, image segmentation-based, frequency domain operations, texture-based defect detection, sparse feature-based processing, image morphology, and deep learning. Deep learning methods are given and analysed with their characteristics and shortcomings [8]. Several research studies were performed to detect defects automatically in circular knitting machines. Some of them are taken to get a background. Saeidi et al. developed a visual inspection system for a circular knitting machine, which comprised a CMOS (Complimentary Metal Oxide Semiconductor) camera using the Garbor wavelet as the detection algorithm [9]. Hemdan et al. have achieved image analysis using a fabric evaluation system for knitted fabrics. Different texture recognition methods: thresholding analysis, radon transform, a discrete Fourier transform, and neural network are applied [10]. Marmaralı et al. have developed a system determining eight different knitting fabric defects; hole, broken needle, colored yarn, thick yarn, thin yarn, cloth fall out, vertical-horizontal lubricant stains on circular knitting machine [11]. Yundang et al. have proposed a system for automatic inspection using smart visual sensors. Defect detection rate is seen 98% on warp knitting machines during actual factory operation as well [12]. Şeker et al. have applied autoencoder deep learning algorithm to detect fabric defects [13]. Takeuchi et al. have offered a simple analysing system for vertical line defects by fixing a camera on the circular knitting machine [14]. Wang et al. have presented and compared defect detection method and deep-learning defect detection techniques. They have used the average brightness of Wale direction successive pixels [15]. Hanbay et al. have introduced a computer vision-based detection system for circular knitting fabrics using shearlet transform [16].

When the knitted fabric production capacity of Turkey is considered, the importance of an automatic fabric insepetion system for knitted fabric can be well understood.

The total annual production capacity of 949 circular knitting manufacturers operating in Turkey is 740.6 thousand tons. This corresponds to 3rd rank after China and India with a share of 3.8% [20]. Within the scope of the study, the most common defect types and the frequency of these defects were determined by interviewing with 10 different knitted fabric manufacturers. Table 1 summarizes the scale of the knitted fabric manufacturer according to gathered information. The annual rate of the most common types of defects in a knitted fabric enterprise is as shown in Table 1. It can be clearly revealed that approximately 27.4 tons of defective fabrics are produced in a year. This defective fabric amount will change according to the production capacity of the mill. The difference between raw fabric defects and 2nd quality sales is 40,000 Euros/Year for one knitted fabric enterprise. When the total capacity of Turkey with 949 circular knitting manufacturers is considered, it is estimated that 37.96 million Euros loss will occur annually. Minimizing this loss is very critical in terms of sustainability. These losses can be intervened quickly to prevent a loss of 40,000 Euros/Year in an operation.

Table 1. Annual amount of defective knitted fabrics

	Defect Types	Defective Fabric Amount (Kg/year)
1	Knots	908,4
2	Lycra missing	11.606,4
3	Drop stitches	10.522,8
4	Loops/Drop	4.057,8
5	Hole/cracks	301,8
	Total	**27.397,2**

The proposed study presents a machine vision system designed for circular knitting machines to inspect fabric defects during the knitting process. The design of the proposed FAVI system made the fabric inspection possible requiring no modifications to the circular knitting machine and without reducing the production efficiency. The computers in the factory can follow the automatic fabric control process. The knitted fabric surface is detected in real time during manufacturing. In many real-time studies in the literature, fabric defects have been detected using different image processing techniques and classified by artificial neural network methods. In this study, deep learning architectures, which offer more robust and effective solutions to pattern recognition and classification problems, are used. Since these network models are trained with at least one thousand data, they have very high accuracy rates. The growth of data and reaching more meaningful information from the data necessitate optimization of feature estimations. With a classical Neural Network model, the connections between neurons and layers and the learning parameters pose enormous computational difficulties. Therefore, deep learning algorithms can be used as an important solution to obtain faster and safer results in real-time industrial applications.

This study develops an innovative solution and test the performance of deep learning algorithms on a real-time fabric defect detection system.

2. MATERIAL AND METHOD

2.1 Material

Knitted single jersey elastic fabrics are normally produced by plating of lycra (spandex) combine with cotton yarn in a circular knitting machine. This type of fabrics and their cloths have a great response and gain their original size and shape due to physical extension by any part of human body. In the study, single jersey fabric was produced from 30/1 ring combed yarn with a density of 35 stitch/inch. Pilottelli circular knitting machine was used to build the vision system. Technical specifications of the industrial circular knitting machine were 30 inches cylinder diameter, 28 needles/inch number of feeder and 300 rpm production speed. Videos taken with common defects are classified for training. Classifications are performed for 5 defects; **double yarn, holes, drop stitches, oil lines,** and **lycra missing**. Recognizing difficulties of defects are changing according to their type. Image frames are taken on circular knitting machine with camera system in holder are given in Figure 1. The resolution of the image was set to 248 pixels/line, and the size of the image frame were selected as 2048x638 pixels. Since the difficulty level of the defects created in the circular knitting machine is different, the number of images of some defects could not be equalized. The class with the minimum number of defects considered to ensure that the number of images is equal in other defect types.

2.2 Machine vision system design

The machine vision system was designed in accordance with the circular knitting machine structure and operating system. The system consists of camera attachment unit, the lightening unit, an encoder, and a desktop computer. The camera system and the lighting unit should see the fabric surface properly. Appropriate locations were determined for the machine vision system so that it can be easily adapted on the circular knitting machine, does not interfere with the operation of the knitting machine, and does not affect the production performance.

Suitable apparatus and mechanical parts were designed for connecting the cameras to these positions. A camera holder designed to operate with the machine in Figure 2. This holder includes a lighting unit, an encoder and camera together with a holder. Lighting unit includes 12 LED's providing 6 V white light source. LED has placed on the circumference of fiberglass plate covering camera lens. Since the diameter of the camera holder apparatus is 6.5 cm, 12 LED light sources with a diameter of 0.8 cm were placed on the fiberglass plate at equal intervals. The number of light sources used are sufficient in terms of the sensitivity and resolution of industrial cameras being quite good. Morover uniform lighting is needed to get clear images with homogeneous light conditions. The image acquisition system captures high resolution and vibration free images. Thus, synchronization is necessary while taking video images of knitted fabric. For this aim, encoder pulses are being sent to camera input. "BASLER 105993 raL2048-48gm-basler racer" camera was mounted into the knitting machine. The sampling rate of the camera was determined as 51 kHz (51000 lines/sec). Images followed by BASLER GUI named PYLON and the image acqusion parameters adjusted. Having designed the machine vision system and its position in the circular knitting machine, a connection made with the computer in the quality control room. Communication between the circular knitting machine and the computer is provided by ethernet cable in the quality control room of the production mill.
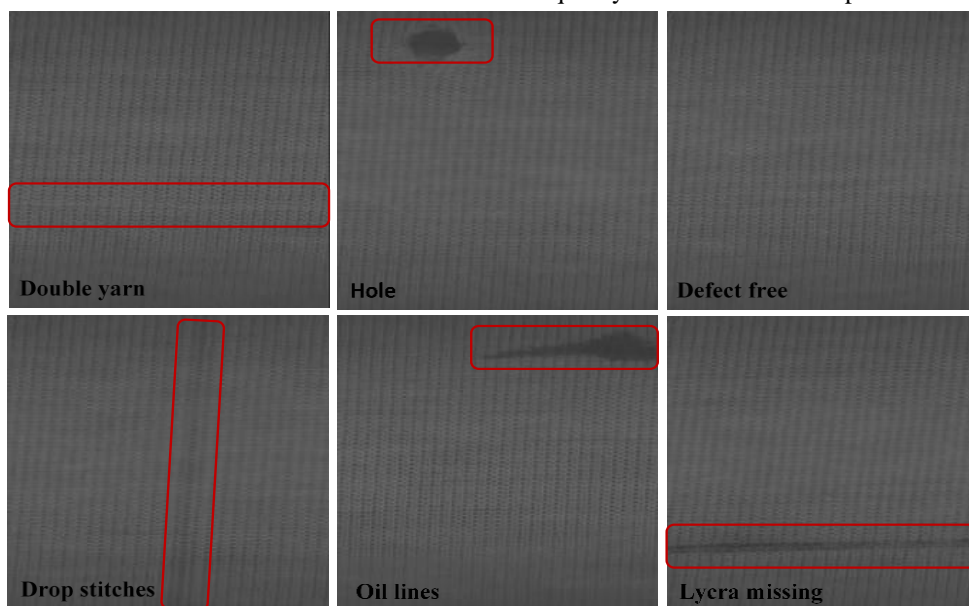

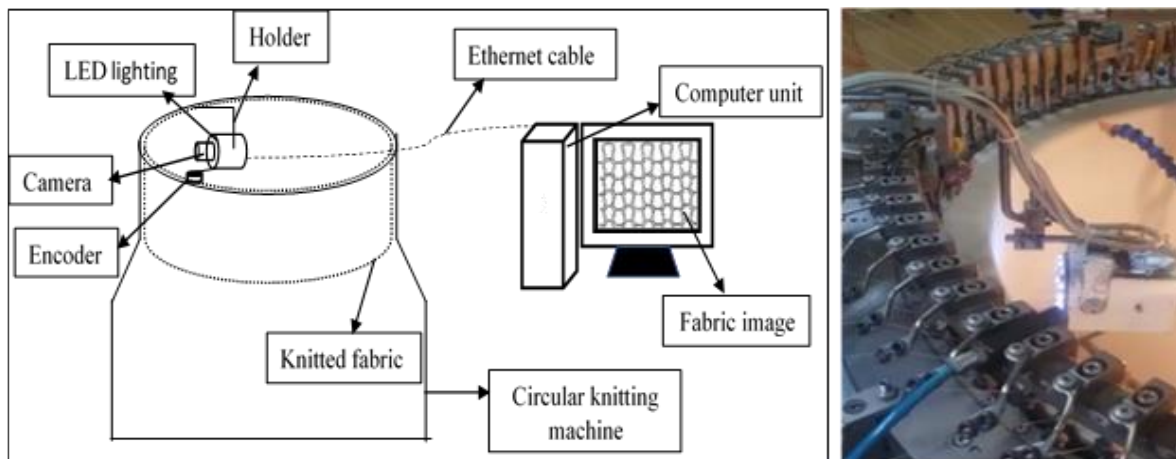**Figure 1.** Images taken by the machine vision system

Figure 2. Machine vision system-The circular knitting machine

2.3 Method - convolution neural networks (CNNs)

CNNs are a sub-branch of deep learning used in analyzing visual information. Deep learning goes to the neuroscientific perspective of classification problems. It addresses a more general principle of learning multiple composition levels that can be applied in machine learning frameworks [1]. CNNs take the neural network techniques of the previous generation. They then add advanced automatic feature extraction to make it easier to answer computationally difficult questions about complex data with great reliability in applications. Automatic feature extraction is another one of the great advantages that CNNs has over traditional machine learning algorithms [2]. The target of a CNN is to learn higher-order features in the data via convolutions. They are well suited to object recognition with images and consistently top image classification competitions. They can identify faces, individuals, street signs, vehicles, objects, and many other aspects of visual data. CNNs have been shown to learn general visually generic features on the first few layers and then gradually build up dataset-specific features on later layers. These early layer features are similar to Gabor filters and color blobs.

The system consists of image acquisition hardware and pattern recognition software. Image Acqusition Toolbox and Deep Learning Toolbox have studied in MATLAB®2019 in two stages. Initially, the image frames captured by using the machine vision system for offline training phase. The testing process then performed on the images taken while the knitting machine was running in real-time application. Total 250 defective images, with 50 image frames for each of the 5 different defect classes, were compiled for use in CNNs. Along with the determination of the defect classes, 1600 frames of defect-free fabric images were included in the data set so that the trained convolution neural network could distinguish the fabric without defect. Transfer learning architectures: ResNet-50, AlexNet and GoogLeNet networks were trained using with 1850 image

frames in total. While training networks; 70 % of database is utilized for training and remaining is for (30%) validation. The information obtained from the literature, it was observed that the most frequently changed parameters during transfer learning applications were "**Learning Rate**", "**Mini Batch Size**" and "**Number of Epoch**". Meanwhile, during training network, many different values applied for these parameters and the best network training result was obtained.

(i) ResNet
The original architecture of ResNet consists of 152 layers. ResNet has a deeper structure than previous architectures. ResNet, which has a different logic than its predecessors, where the network model is beginning to deepen; It is formed by adding the residual block to the model, which feeds residual values to the next layers. With this feature, ResNet ceases to be a classic model (Figure 3) [17].

ResNet-50 that is a smaller version of ResNet 152 used as a starting point for transfer learning. This model consists of 5 stages each with a convolution and identity block (Figure 4). Each convolution block has 3 convolution layers, and each identity block also has 3 convolution layers. The ResNet-50 has over 23 million trainable parameters.

The fc (fully connected) layer in the last layer in ResNet network has been changed to suit our own data. The parameters are taken during training network; Learning Rate=0,0001, Mini Batch Size=32 and Number of Epoch=50. The success percentage of the artificial neural network trained with the entered parameters was obtained as 96.58%.

(ii) AlexNet
AlexNet consists of eight layers, the first five of which are convolutional, and the last three are fully connected layers (Figure 5). Among these layers, there are also "pooling" and "activation" layers. The designed network used for classification with 1000 possible categories [19].
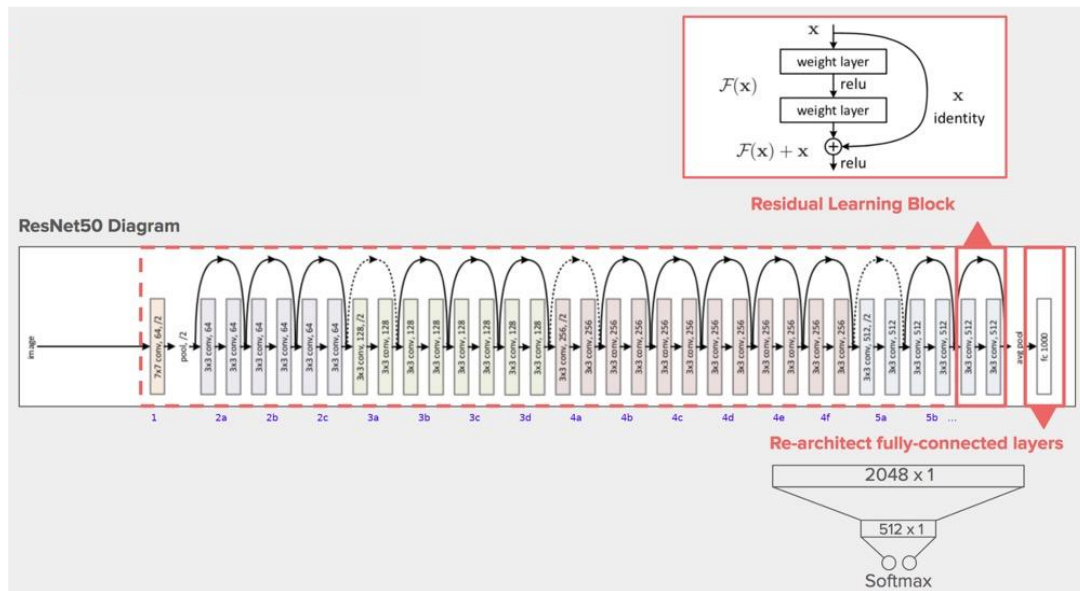
Figure 3. ResNet architecture [18]
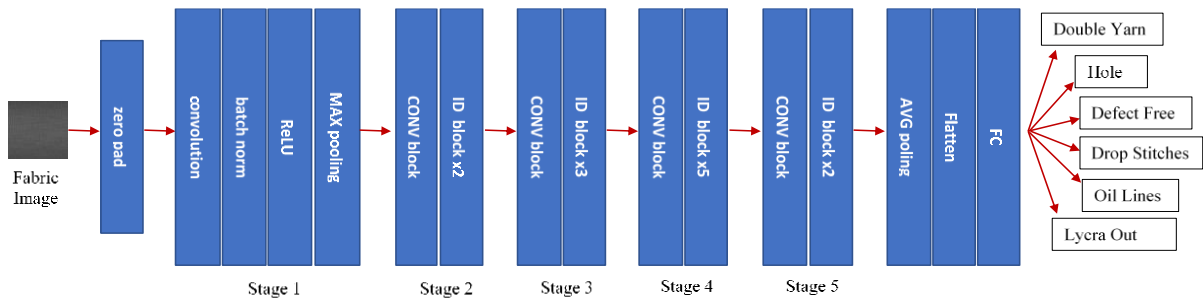
Figure 4. ResNet-50 architect
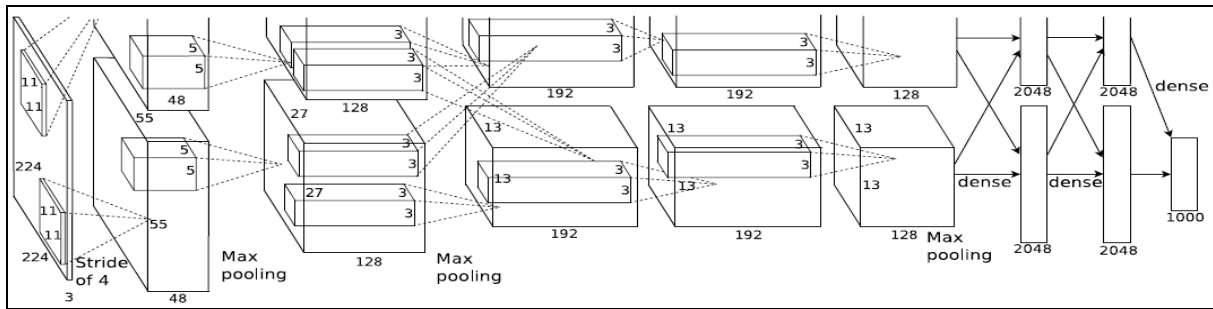
Figure 5. AlexNet Architecture [18]

AlexNet architecture was adapted to the dataset which used in knitted fabric defect control by changing the last three fully connected layers (fc6, fc7 and fc8) before training. By changing the output layer in the last, the training analysis stage was started. During the AlexNet network training, the training process parameter was used by entering Learning Rate=0.001, Mini Batch Size=32 value, and Number of Epoch=50. 40 iterations were performed in each Epoch with the number of images in the data set and the entered Mini Batch Size value. The success percentage of the artificial neural network trained with the entered parameters was obtained as 91.89%.

(iii) *__GoogLeNet__*

GoogLeNet consists of a complex structure created from 'Inception' modules (Figure 6). Unlike previous studies, the depth and width of the network prepared were increased while the calculation cost was kept low. Architecture consists of 22 layers. Architectural decisions based on the Hebbian principle and the intuition of multi-scale processing to optimize quality. It is different and difficult to understand from the network models mentioned so far [20].
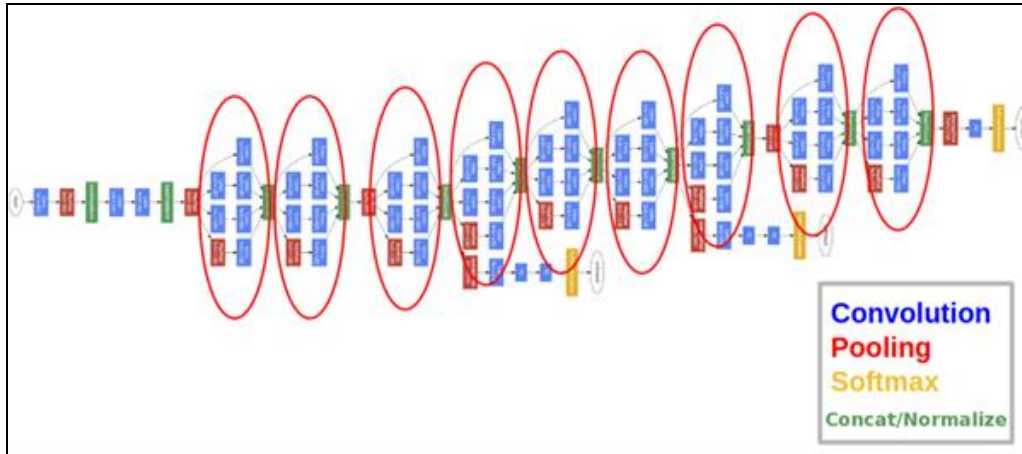
Figure 6. GoogLeNet architecture [19]

Before the model was trained, the output layer was changed by adapting the fully connected (fc) layer to our own data set. While training GoogLeNet network, the parameters are taken as Learning Rate= 0,001, Mini Batch Size=32 and Number of Epoch= 30. After 40 iterations were completed, the success rate with 94,23 % was obtained.

2.4 Confusion matrix

Cross Validation is a technique used in model selection. The error of a test performed is predicted in a machine learning model. After placing a model in training data, its performance is measured against each new validation set and then how the model performs when trying to predict new observations. Confusion matrix is a table used to measure the performance of a classification model on a set of test data for which actual values are known (Table 2). The confusion matrix gives very fruitful information about the predicted performance of the estimator or model that use in machine learning. The whole data set is randomly divided into two parts as training set and test set. The trainer is used to select the most suitable model parameters using cross validation, and the test set is used only to measure the performance (accuracy) of the most suitable model. Classification accuracy is evaluated by the percentage of data samples classified as correct by the algorithm. Actual values are true binary values "0" and"1" [22,23].

Table 2. Confusion matrix

		Predicted	
		Positive	Negative
Actual	**Positive**	True Positive (TP)	False Negative (FN)
	Negative	False Positive (FP)	True Negative (TN)

True Positives (TP) are the examples where the real data value is 1 and the predicted value is 1. True Negative (TN) refers the examples where the real value is 0 and the predicted value is 0. False Positive (FP) are the **e**xamples

where the real value is 0 and the predicted value is 1. False Negative (FN) are the examples where the real value is 1, and the predicted value is 0. In other words, if the output of the correctly predicted value is false, it will be FN. Accuracy Rate is a measure of how often the classifier method makes correct estimates. Predicted values are found by dividing the sum as in Equation 1. Precision is based on true positive values only out of all positive values. It is a measure of how accurately you are predicted (Equation 2). It takes a value between 0 and 1, it should be as high as possible **Recall (Sensitivity)** shows how successfully positive situations are predicted. The best value is 1, the worst value is 0 (Equation 3). **F-Score** is difficult to compare two models with low precision and high recall or vice versa. F-score helps to measure Recall and Precision at the same time.

$$\text{Accuracy} = (TP + TN)/(TP + TN + FP + FN) \qquad (1)$$

$$\text{Precision} = TP/(TP + FP) \qquad (2)$$

$$\text{Recall} = TP/(TP + FN) \qquad (3)$$

$$F - Score = 2 \times Recall \times \frac{Precision}{Recall} + Precision \qquad (4)$$

Having trained the CNN models, CM (confusion matrix) analysis was performed with 20 fabric images from each class for validation. A total of 120 fabric images used for testing. The images used for testing phase were taken during knitted fabric production in real time with the machine vision system placed on the circular knitting machine.

3. RESULTS AND DISCUSSION

3.1 The results of resnet-50 cnn algorithm

After creating a confusion matrix chart from the true labels and the predicted labels, TP and FP rates in the row summary were displayed as sensitivity and specificity. Also, specify column summary as displayed the positive predictive rates and false predictive rates as precision and

negative predictive value. Figure 7 shows CM (confusion matrix) of fabric defects on the circular knitting machine and the evaluation of the CNNs algorithm in six classes such as (1) double yarn, (2) hole, (3) defect free, (4) drop stitches, (5) oil lines and (6) lycra missing respectively.

According to the ResNet-50 analysis made on the obtained images, the success rate which called sensitivity for each class were given in Figure 7. An average accuracy of 98.31% were achieved. According to ResNet's classification results, there were actually 20 hole defects, but only 18 of these 20 defects were correctly predicted. One of the hole defects is classified as defect free and the other one hole defect is labeled as oil lines. The remaining images in classes double yarn, defect free, drop stitches, oil lines, and lycra missing are all classified with 100% accuracy as can be seen in the Figure 7. This ratio is a very good result for determining the defect class on the knitted fabric. When the knitted fabric defect, which are evaluated manually in the fabric production line by the experienced employees, the success rate is acceptable.
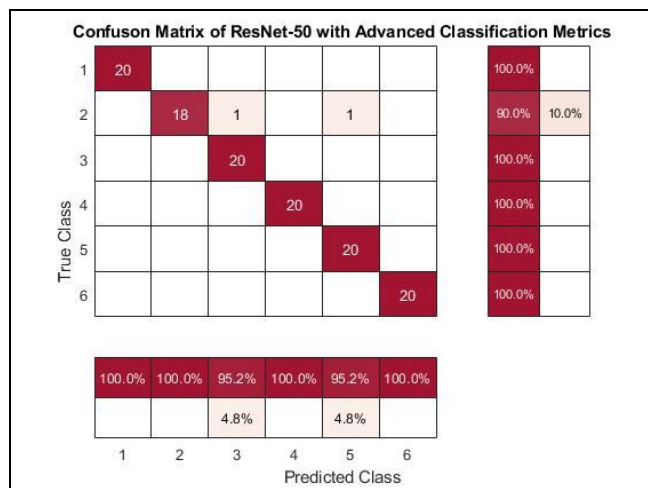

Figure 7. ResNet-50 classification results

3.2 The results of alexnet cnn algorithm

According to the AlexNet results the success rate for each class were obtained as Figure 8. An average accuracy of 95% were achieved. When AlexNet's classification results were examined, it can be observed that 20 of 18 double yarn defects were correctly predicted. One of the double yarn defects labeled as defect free and the other one as drop stitches. Looking at the hole defect, 2 of them were classified as defect free and 1 as a drop stitch. Finally, trained network classified one of the 20 oil lines as hole defects. Thus, defect free, drop stitches, and lycra missing classes labeled with 100% accuracy.

3.3 The results of googlenet cnn algorithm

According to the GoogLeNet results of the analysis made on the obtained images the success rate, which called sensitivity for each class were obtained (Figure 9). An average accuracy of 94.17% were achieved. When

GoogLeNet's classification results were examined, there were actually 20 hole defects, but only 18 of these 20 defects were correctly predicted. Two of the hole defects were predicted as as a defect free class. From the third row, it can be seen that one of the defect free class was classified as drop stitch and one as a hole defect. The last one, trained network classified one of the 20 oil lines as lycra missing and two of them were classified as hole defects.
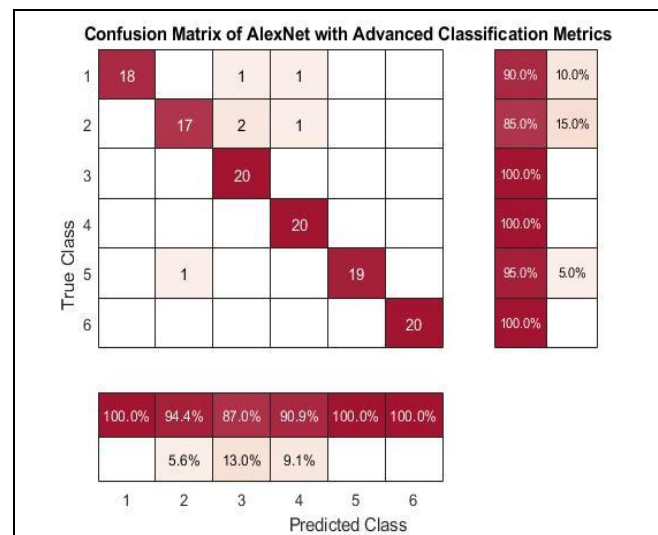
Figure 8. AlexNet classification results
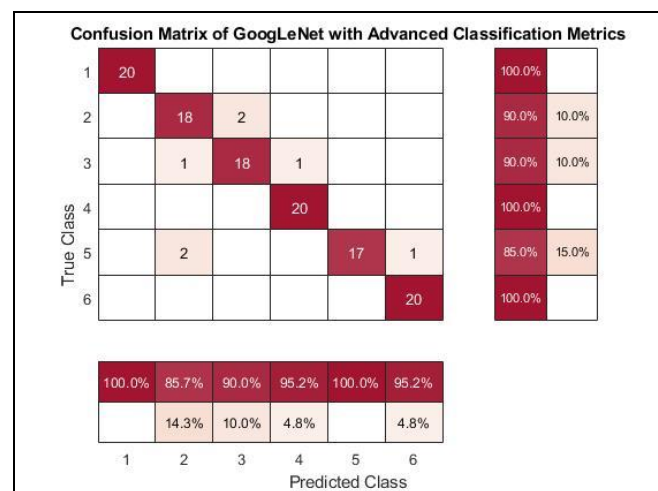
Figure 9. GoogLeNet classification results

All three of the CNNs architectures trained with transfer learning for real-time defect classification on the circular knitting machine were tested. According to the comparison of the methods (Figure 10), it was revealed that all of three method achieved high classification success rate. According to the average accuracy rates, ResNet-50 network achieved the highest success rate of these three architectures. According to F-score; double yarn defects were classified with the highest 100% success rate for two networks (ResNet-50 and GoogLeNet), while the lowest 94.5% was achieved using AlexNet. Hole defect is labeled with a 94.7%, 89.5%, 87.8% success rates respectively for the

three trained networks. A classification success rate was achieved between 90% and 97.5% for the defect free fabric. While ResNet-50 showed a 100% success rate in the drop stitches defect, the other two trained networks also achieved a success rate over 95%. In the oil lines class, an overall success rate of over 90% was observed with three networks. Finally, while the GoogLeNet network completed the classification process with a successs rate of 97.5%, other two the networks had a success rate of 100%. When the images obtained by the machine vision system placed on a circular knitting machine are evaluated, the classification obtained results are mostly acceptable. Consequently, using deep learning technique for real-time defect inspection is highly reliable and applicable for industrial application. All the deep learning architectures applied within the scope of the study showed a success of over 94%. Among these architectures, the highest success was obtained with ResNet50. It is theoretically thought that the success will increase as the number of layers increases in a network model. However, this is not the case in reality. Based on this, the ResNet model was created. According to the new created theory (ResNet), thanks to the residual value feed, the new output equation optimizes the learning error with the residual value from the two previous layers even if the current weight is 0. Thus, faster, and more reliable success rates are obtained by using residual values [17]. The ResNet50 model gives a better result due to its feedback feature.

4. CONCLUSION

The textile sector aims to produce fabrics with high quality standards together with high production capacity. Customer demands and expectations from the product are increasing and changing day by day. This situation makes competition conditions difficult. Textile enterprises get attention importance to technologies and developments. These will provide speed and flexibility in production, reduce costs, improve product quality, and improve their functions. When the defect detection studies are examined, it is seen that not only image filter applications are sufficient for real-time industrial applications, but also machine learning or deep learning methods are used together with different filter applications. Image processing methods are used in surface feature extraction, and defect detection and classification processes are performed by artificial intelligence methods (CNNs).

A machine vision system has been developed on circular knitting machines where fabric defects can be automatically controlled and detected defects can be classified. The five most common knitted fabric defects; double yarn, holes, drop stitches, oil lines, and lycra missing were detected and classified with the prepared CNN based artificial intelligence software with an average success rate of 98%. Although there are many studies on fabric defect detection by using image processing algorithms in the literature, any study has not been encountered that use CNNs technique with a machine vision system adaped on an industrial circular knitting machine. In this study, real-time knitted fabric inspection proces was achieved during the fabric production via a program user interface based on CNN algorithm. The use of such a machine vision system in knitted fabric enterprises will bring great economic gains to companies. When the analyzes are evaluated, the annual cost of defective fabrics sold as second quality is quite high. Therefore, the usega of this system is expected to increase the production of knitted fabric enterprises, while it is expected to significantly reduce the company reclamation due to defective fabrics.

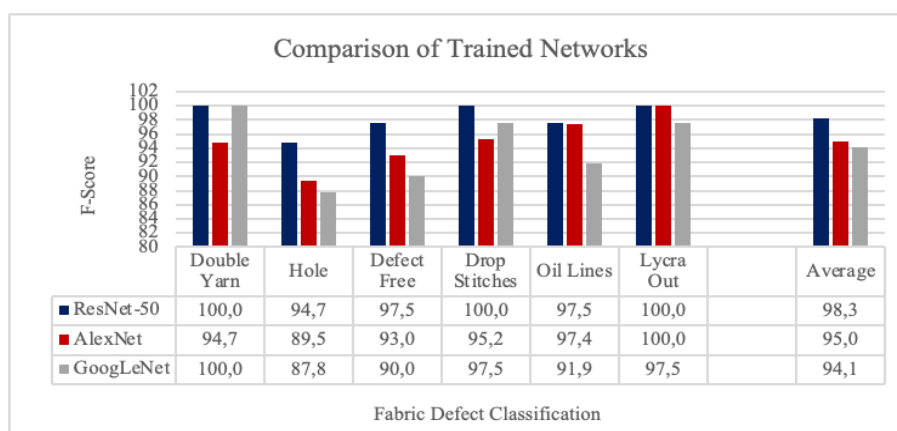|	Double Yarn	Hole	Defect Free	Drop Stitches	Oil Lines	Lycra Out		Average
ResNet-50	100,0	94,7	97,5	100,0	97,5	100,0		98,3
AlexNet	94,7	89,5	93,0	95,2	97,4	100,0		95,0
GoogLeNet	100,0	87,8	90,0	97,5	91,9	97,5		94,1

Figure 10. Comparison of the CNNs architectures

REFERENCES

1. Goodfellow I, Bengio Y, Courville A. 2016. *Deep learning (Vol. 1, No. 2)*. Place: MIT Press Cambridge.

2. J Patterson, A Gibson. 2017. *Deep Learning: A Practitioner's Approach*. Place: O'Reilly Books.

3. Çelik Hİ, Dülger LC, Topalbekiroğlu M. 2013. Development of a machine Vision System: real-time fabric defect detection and classification with neural networks. *The Journal of Textile Institute* 105(6), 575-585.

4. A Rasheed, B Zafar, A Rasheed, N. 2020. Fabric Defect Detection using Computer Vision Techniques: A Comprehensive Review. *Hindawi-Mathematical Problems in Engineering*.

5. Sun Y, Long H. 2011. Adaptive detection of weft‐knitted fabric defects based on machine vision system. *J. of the Textile Institute* 102(10), 823-836.

6. W Wang, J Jiang. 2018. Computer Vision Techniques for detecting fabric defects. *Applications of Computer Vision in Fashion and Textiles* 47-60, Woodhead Publishing.

7. J Yang, S Li, Z Wang. 2020. Using Deep Learning to Detect Defects in Manufacturing: A Comprehensive Survey and Current Challenges. *Materials* 13(24), 5755.

8. MA Taher, MM Rahman, MA Jahangir. 2016. Study on Different Types of Knitting Faults, Causes and Remedies of Knit Fabrics. *Int. J. of Textile Science* 5(6), 119-131.

9. RG Saeidi, M Latifi, SS Najar. 2005. Computer vision-aided fabric inspection system for on-circular knitting machine. *Textile Research Journal* 75(6), 492-497.

10. AT Hemdan, MS Aya Tallah. 2008. Online fabric defect detection and full control in a circular knitting machine. *AUTEX Research Journal* l.8(1), 21-29.

11. TK Torun, A Marmaralı. 2011. Online Fault Detection System for Circular Knitting Machines. *Tekstil Ve Konfeksiyon* 21(2), 164-170.

12. L Yundang, A Jingxuan, S Changqing. 2013. Online Fabric Defect Inspection using Smart Visual Sensors. *Sensors* 13, 4659-4673.

13. Şeker, KA Peker, AG Yüksek. 2016 May. Fabric defect detection using deep learning. In 24th Signal Processing and Communication Application Conf. IEEE 1437-1440.

14. S Takeuchi, K Nishioka, H Uematsu. 2018. Research into Development of the Defect Detection System for Knitted Fabric Produced by the Circular Knitting Machines by Image Analysis. *Journal of Textile Engineering* 64(2), 45-49.

15. X Wang, G Wu, Y Zhong. 2018. Fabric Identification Using Convolutional Neural Network. *Artificial Intelligence on Fashion and Textiles* 93-100.

16. K Hanbay, M.F Talu, Ö.F Özgüven. 2019. Real-Time Detection of Knitting Fabric Defects Using Shearlet Transform. *Tekstil ve Konfeksiyon* 29(1), 3-10.

17. K He, X Zhang, S Ren. 2016. Deep residual learning for image recognition. In Proceedings of the IEEE Conf. on Computer Vision and Pattern Recognition 770-778.

18. 2022, March. How to split resnet50 model from top as well as from bottom. Retrieved from https://stackoverflow.com/questions/54207410/how-to-split-resnet50-model-from-top-as-well-as-from-bottom

19. A Krizhevsky, I Sutskever, GE Hinton. 2012. Imagenet classification with deep convolutional neural networks. *Advances in neural information processing system* 25, 1097-1105.

20. C Szegedy, W Liu, Y Jia. 2015. Going deeper with convolutions. In Proceedings of the IEEE Conf. on Computer Vision and Pattern Recognition 1-9.

21. 2021, March. İstanbul Tekstil ve Hammaddeleri İhracatçıları Birliği 2021 March. Retrieved from http://www.ithib.org.trs

22. 2022, Confision Matrix. Retrived from https://en.wikipedia.org/wiki/Confusion_matrix

23. 2022, March. Confusionmat. Retrieved from https://www.mathworks.com/help/deeplearning/ref/confusionmat.html

Balancing The Shirt Production Line Under Different Operational Constraints Using An Integer Programming Model

Şeyda Topaloğlu Yıldız[1] 0000-0001-6827-126X
Gülseren Karabay[2] 0000-0002-1231-2816

[1]Dokuz Eylül University, Industrial Engineering Department, İzmir, Türkiye
[2]Dokuz Eylül University, Textile Engineering Department, İzmir, Türkiye

Corresponding Author: Şeyda Topaloğlu Yıldız, seyda.topaloglu@deu.edu.tr

ABSTRACT

Efficient use of capacity is significant to enable apparel businesses to work cost-effectively and provide timely service to their customers. The increase in assembly-line efficiency is associated with lower operating costs. Therefore, balancing assembly lines is mainly to manufacture products as profitable and quickly as possible. In this study, we consider a single-model assembly line balancing problem with workforce and machine constraints in the sewing department of an apparel company. We develop an integer programming (IP) model to optimally balance the shirt production line, considering parallel machines in each stage of the line and various operational constraints such as cycle time and precedence constraints, task machine eligibility, and the number of operators available. The IP model can either minimize the number of open workstations or both, minimize the number of open workstations and simultaneously assign tasks in subassembly parts close to each other. The model has been run under various scenarios using LINGO 15.0 optimization software. Additionally, we have balanced the shirt production line using the Ranked Positional Weight Method (RPWM) for comparison purposes. The IP model outperforms the RPWM results across all scenarios and finds 33 stations and 86.8% efficiency compared to 38 stations and 75.4% balance efficiency with the RPWM.

1. INTRODUCTION

Assembly lines are one of the most popular production methods among flow-through manufacturing systems. They are extensively used in the production of high-quality standard products. Simultaneously, assembly lines have become increasingly important for producing small quantities of custom products [1]. Increasing product variability and shorter life cycles have shifted from traditional production methods to assembly lines. Assembly lines are expected to produce products fast, efficiently, cost-effectively, and with the necessary quality [2]. The assembly line balancing problem (ALBP) consists of assigning tasks to an orderly sequence of stations so that the precedence relationships between the tasks are satisfied and some performance measures are optimized (e.g., minimize the balance delay or minimize the number of workstations) [3].

The apparel industry is a very labor-intensive industry. The efficient use of capacity is of the utmost importance for apparel companies to operate cost-effectively and provide timely service to their clients. Delivering orders on time is essential to improve the relationship with customers. Reducing operational costs and delivering orders on time are closely linked to improving line efficiency. Even though the quantities ordered have declined over the last two decades, the variety of models has increased, making the rapid creation of a balanced line another crucial issue. Thus, studies about the ALBP have increased in the apparel industry. Many researchers have conducted studies using

different heuristic methods and simulation modeling in the apparel industry. The real-case studies that solve the ALBP in the apparel industry are given below.

Kurşun and Kalaoğlu simulated a sweatshirt line and verified that the developed simulation model produced the same performance results as the existing system [4]. Kayar and Akalin examined the applicability of the Hoffman method to apparel assembly lines and compared it with the simulation model results [5], whereas Ünal et al. proposed a heuristic algorithm for line balancing and examined its effectiveness using simulation [6]. Ünal and Bilget created simulation models for three products using statistical task time distributions and implemented lean manufacturing principles. They developed a new algorithm to balance lines within a simulation application [7]. Ünal and Demirbas created an alternative production line to obtain more output with fewer operators using simulation [8]. Eryuruk et al.'s study compared the Ranked Positional Weight Method (RPWM) with the Probabilistic Line Balancing Technique (PLBT) and found that the RPWM's results were better [2]. Eryuruk et al. solved the ALBP via the PLBT to increase the line efficiency for a constant cycle time. They demonstrated that assigning tasks to stations with greater accuracy and obtaining reliable results is possible [9]. Güner et al. studied the applicability of five heuristic balancing methods and an improving method for a t-shirt production line. All the balancing methods achieved the same results, while the improving method increased the line's efficiency despite the increase in the number of stations [10]. Karabay examined two real practical line balancing techniques and compared their performance with the performance of the RPWM. The performance of these techniques was improved by using the precedence relations of tasks [11]. Ünal proposed a New Incremental Utilization Technique to address quality issues by grouping the same machinery and adjusting less circulating workflow for the ALBP [12]. Turkmen et al. developed a computer program that uses the Hoffman, Ranked Positional Weight, COMSOAL, and Kilbridge and Wester methods for the t-shirt and knitted pants ALBP [13]. Jirasirilerd et al. used a variable neighborhood adaptive search method to minimize cycle time for a simple ALBP in the garment industry, considering the number and types of machines used in each workstation [14].

Bongomi et al. improved a complex trouser assembly line efficiency using the RPWM and examined its applicability under two-line balancing scenarios (with and without resource constraints) [15]. The RPWM has recently drawn researchers' interest because of its capability of providing higher line efficiency than its other counterparts, such as the probabilistic line balancing technique, Hoffman method, and the Kilbridge and Wester method. The results indicated that the RPWM is appropriate if there is no constraint on the resource. However, it is ineffective for complicated clothing assembly lines with different machine types. Kayar and Akalın balanced the blouse manufacturing line using the RPWM, considering the operation durations obtained from the method study and the current operation times. They analyzed the effects of the method study on production volume and assembly-line efficiency to show the significance of the method study [16]. Ahmed et al. used the Largest Candidate Rule, the Kilbridge and Wester method, and the RPWM to reduce idle time, workstation number, and labor requirement. They found a new workflow to distribute the tasks across workstations and proposed an optimal layout to reduce idle time and workforce requirements [17]. Kayar and Akyalçın used the Ranked Positional Weight, Hoffman, COMSOAL, Moodie and Young, Kilbridge and Wester, Largest Candidate Rule, and Classical methods to balance the t-shirt production line [18]. A comparative analysis of these methods has been done, and the Classical method is evaluated as the most advantageous. In the study by Phan et al., five different heuristic assembly line balancing methods (RPWM, Probabilistic Line Balancing technique, Longest Task Time Method, Most Following Tasks Method, Organizing Synchronize the Work Stations Method) were used for t-shirt production in the Vietnam garment industry [19].

In most of the literature on the ALBP in the apparel industry, heuristic methods and simulation models have been used to balance single-model assembly lines to minimize the number of workstations. Mathematical models are used in only a few of them. Gürsoy initially created an IP model that minimizes the idle time per operator, then a new heuristic algorithm that reacts promptly to market demands and finds the minimum number of operators [20]. Gürsoy and Gürsoy found minimum idle time per worker for a given production rate using IP and catered to market demands using a genetic algorithm [21]. Xu et al. rearranged manufacturing tasks for apparel production to optimize one-piece flow assembly lines under certain conditions and minimize the number of workstations and the idle time of the assembly line. Their paper proposed a modified adaptive ant colony optimization method [22]. Ahmed and Ador reduced the cost, space, and cycle time for a mixed-model ALBP [23]. Their model ensures that the workstation time does not exceed the cycle time, precedence relations are satisfied, and only an allowed number of machines can be assigned to a workstation.

This study establishes a novel mathematical model that considers parallel workstations, manually performed and machine-requiring tasks, the available number of machine types and operators, and task assignment restrictions for the ALBP in the sewing department of a garment business. The mathematical model is developed to balance the shirt production line optimally, considering parallel machines in each stage of the line under the cycle time constraint. Seven different integer programming (IP) models were developed under various operating conditions. Helgeson and Birnie's RPWM has also been applied for comparison purposes [24]. We prefer RPWM in this study because when studies with heuristic line balancing methods are examined, this method is used in most studies, as seen in the literature above.

2. MATERIAL AND METHOD

2.1 Material

This study uses the proposed IP model and RPWM for the ALBP of an apparel company for shirt production. The computational results obtained from the two methods are compared with each other. The daily working time is 9 hours, and the targeted daily production rate is 750 pieces/day. The studied shirt model and its flowchart are shown in Figure 1, which has 20.617 min of assembly work, and the required cycle time is 0.72 min/piece.

2.2 Method- mathematical programming model

An IP model is developed to solve the ALBP of an apparel company. The model is generic in that it incorporates the assignment of workers and machinery necessary to perform tasks, accommodates parallel workstations, and minimizes the number of workers subject to a specified cycle time constraint. LINGO 15.0 Optimization software [25] was used to solve the proposed IP model optimally.

The basic assumptions considered when developing the IP model are as follows:

- The assembly line consists of a series of stages in which a workstation or parallel workstations are allowed.

- A workstation operates manually or requires a specific machine type to perform assigned tasks.

- Specific tasks are performed manually, while others can only be performed on a required machine type.
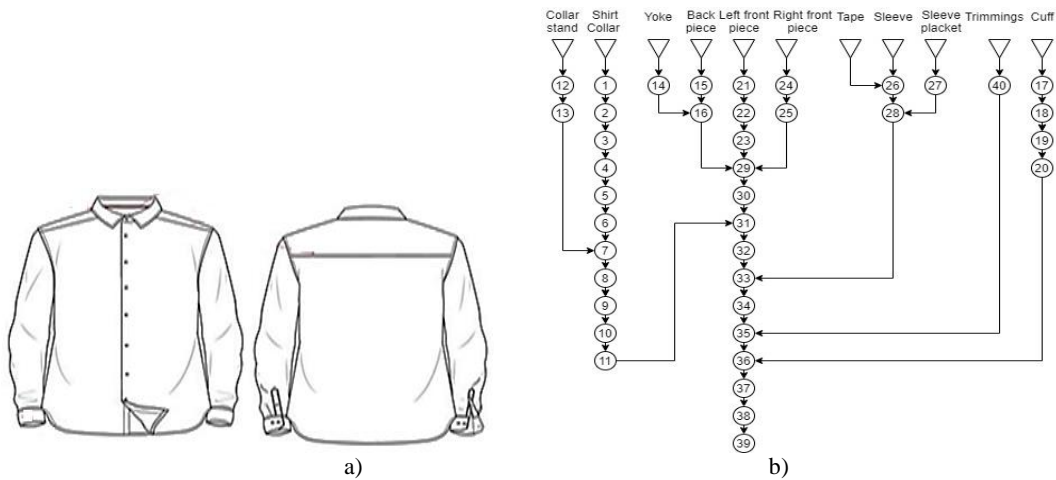
Figure 1. a) Shirt model **b)** Flow diagram of the shirt

- Only one product model is produced on the assembly line.
- The precedence relationships between the tasks are known.
- Task times are deterministic.
- The workpiece is moved manually between workstations.
- A worker operates each type of machine.
- The number of workers available is limited.
- The number of machines available from each type is limited.

Indices, Sets, Parameters

i	The index for the tasks, $i = 1, ..., N$
s	The index for the potential stages on the assembly line, $s = 1, ..., S$
m	The index for the machine type assigned to a stage on the assembly line, $m = 1, ..., M$ ($m = 1$ indicates the manual workstation type)
P	The set of task pairs (i, j) in precedence relations
PR_i	The set of tasks preceding task i
S_i	The set of tasks succeeding task i
B	The set of tasks assigned to the first station
A_{im}	1, if machine type m is capable of performing task i and 0, otherwise
t_i	The processing time of task i
E_i	The earliest stage number that task i can be assigned
L_i	The latest stage number that task i can be assigned
C	The cycle time
K	The maximum number of parallel workstations allowed in each stage
TW	The total number of workers available
TM_m	The total number of type m machines available

Decision Variables

x_{is}	1, if task i is assigned to stage s and 0, otherwise
y_{sm}	1, if manual workstation type or machine type m is assigned to stage s and 0, otherwise
z_{sm}	number of manual workstations or type m machines assigned to stage s

Objective Function and Constraints

$$Minimize \sum_{s=1}^{S} \sum_{m=1}^{M} z_{sm} \qquad (1)$$

Subject to:

$$\sum_{s=E_i}^{L_i} x_{is} = 1 \qquad \forall i \qquad (2)$$

$$\sum_{m=1}^{M} y_{sm} \leq 1 \qquad \forall s \qquad (3)$$

$$\sum_{s=1}^{S} s \cdot x_{js} - \sum_{s=1}^{S} s \cdot x_{is} \geq 0 \qquad \forall (i,j) \in P \qquad (4)$$

$$\sum_{i=1}^{N} x_{is} \cdot A_{im} \cdot t_i \leq C \cdot z_{sm} \qquad \forall s,m \qquad (5)$$

$$z_{sm} \leq TM_m \cdot y_{sm} \qquad \forall s,m | m > 1 \qquad (6)$$

$$z_{sm} \geq y_{sm} \qquad \forall s,m \qquad (7)$$

$$\sum_{s=1}^{S} \sum_{m=1}^{M} z_{sm} \leq TW \qquad (8)$$

$$z_{sm} \leq K \qquad \forall s,m \qquad (9)$$

$$\sum_{s=1}^{S} z_{sm} \leq TM_m \qquad \forall m | m > 1 \qquad (10)$$

$$x_{i1} = 1 \qquad \forall i \in B \qquad (11)$$

$$\sum_{m=1}^{M} y_{sm} \leq \sum_{m=1}^{M} y_{s+1,m} \qquad \forall s | s < S \qquad (12)$$

$$x_{is}, y_{sm} \in \{0,1\} \qquad \forall i,s \qquad (13)$$

$$z_{sm} \geq 0 \text{ and integer} \qquad \forall s,m \qquad (14)$$

The objective function (1) minimizes the number of machines and manual workstations used, thus minimizing the overall number of workers on the assembly line. Constraint (2) ensures that each task is assigned to only one stage. Constraint (3) assigns at most one type of machine to a stage. All precedence relations among tasks are satisfied by Constraint (4), where task i is an immediate predecessor of task j. Constraint (5) ensures that the total duration of tasks assigned to a stage does not exceed the cycle time multiplied by the number of workstations. Under Constraint (6), the maximum number of type m machines assigned to a

stage does not exceed the number available. This constraint also ensures that the variable z_{sm} is greater than zero only when the variable y_{sm} is set to 1. Constraint (7) imposes that z_{sm} is always positive when y_{sm} is set to 1. Constraints (6) and (7) together provide the necessary relation between the z_{sm} and y_{sm} variables. Constraint (8) ensures that the number of workers on the assembly line should not exceed the number of workers available, whereas Constraint (9) limits the number of parallel workstations in a stage. With Constraint (10), the number of machines from each type allocated to the assembly line should not exceed the available number. Constraint (11) assigns the specified tasks to the first stage of the assembly line. According to Constraint (12), the stages are opened in ascending order. Constraint (13) indicates the binary variables, while Constraint (14) indicates the integer variables.

The lower bound on the number of stages that should be opened, LB, can be estimated as follows:

$$LB = \left\lceil \frac{\sum_{i=1}^{N} t_i}{C.K} \right\rceil^{+} \qquad (15)$$

$$E_i = \left\lceil \frac{t_i + \sum_{j \in PR_i} t_j}{C.K} \right\rceil^{+} \qquad i = 1,...,N \qquad (16)$$

$$L_i = LB + 1 - \left\lceil \frac{t_i + \sum_{j \in S_i} t_j}{C.K} \right\rceil^{+} \qquad i = 1,...,N \qquad (17)$$

Ranked Positional Weight Method

The RPWM was developed by Helgeson and Birnie [24] and is commonly used in ALBPs. According to this method, each task has a positional weight calculated by summing its processing time and all processing times of the subsequent tasks. The steps of the RPWM are as follows:

1. The precedence diagram is created.

2. The positional weight value is calculated for each task.

3. The tasks are ranked in descending order of their positional weight.

4. The task with the greatest positional weight is selected as the next task to assign if its predecessor tasks are already assigned.

5. The selected task is assigned to the current open workstation. If the total workstation time exceeds the cycle time, the next task in the descending positional weight order is assigned as long as it does not violate the precedence relations. If no task can be assigned, a new station opens.

6. Steps 4 and 5 continue to be repeated until all tasks are assigned to stations.

3. RESULTS AND DISCUSSION

3.1 Balancing the line with the ranked positional weight method

The positional weights of all tasks required to sew the shirt model were calculated and ranked in ascending order. For each task, the task time, the type of machine required, all predecessor tasks, and the positional weight value (PWV) are given in Table 1. Some tasks are performed manually, referred to as "manual tasks," while some require specific machine types to process, called "machine tasks."

The daily working time of the company is 9 h. The required production rate for shirts is 750 pieces/day, resulting in a cycle time (C) of 0.72 minutes/piece. The tasks are allocated to the stations sequentially, starting with the highest positional weight and not exceeding the cycle time. The ordering of tasks depends on the type of machine needed and whether the preceding tasks are completed. Also, since some tasks have processing times exceeding the cycle time, it is necessary to open duplicate stations arranged in parallel to achieve the desired production quantity.

For example, tasks are assigned to Station 1 as follows: Task 1 has the highest positional weight at 14.256, and it is a preparatory operation performed on the fusing machine with a standard time of 0.106 min. Tasks 12, 17, and 21 are also preparatory tasks performed on the same machine, with no predecessor tasks required to be completed. Hence, although their positional weights are not the highest, they are also assigned to Station 1.

Table 1. Information on shirt production tasks and their positional weight values in descending order

Task no.	Task name	Machine type	Task time (min.)	Predecessor tasks	PWV
1	Fusing interlining to collar	Interlining Fusing press	0.106	-	14.25
2	Runstithcing collar	Lockstitch machine	0.7	1	14.15
3	Collar tip trimming and turning	Collar tip trimming and turning machine	0.3	2	13.45
4	Collar ironing	Collar press	0.25	3	13.15
5	Topstitching collar	Lockstitch machine	0.6	4	12.9
12	Fusing interlining to the collar stand	Interlining Fusing press	0.106	-	12.36
6	Collar edge trimming	Manual	0.22	5	12.3
13	Baste interlining at collar stand, fused	Lockstitch machine	0.156	12	12.25
7	Attaching collar stand and upper collar	Lockstitch machine	0.8	6,13	12.1
14	Attaching a label to yoke	Lockstitch machine	0.4	-	12.05
15	Attaching yoke to back and simultaneously lay two pleats manually	5 Thread Overlock	0.305	-	11.65
24	Sewing right placket	Lockstitch machine	0.31	-	11.46
21	Fusing interlining to left front placket	Interlining Fusing press	0.206	-	11.48
16	Topstitching back yoke	Lockstitch machine	0.35	14,15	11.35
8	Turning collar stand	Manual	0.35	7	11.3
22	Attaching placket to the left front	Lockstitch machine	0.13	21	11.28
23	Marking button hole positions	Manual	0.15	22	11.15
25	Marking button positions	Manual	0.15	24	11.15
29	Joining shoulders	5 Thread Overlock	0.5	16,23,25	11
9	Stitching through collar stand	Lockstitch machine	0.7	8	10.95
30	Topstitching shoulders	Lockstitch machine	0.6	29	10.5
10	Cutting of extensions of collar stand	Manual	0.2	9	10.25
11	Marking collar stand	Manual	0.15	10	10.05
31	Attaching collar	Lockstitch machine	0.85	11,30	9.9
26	Attaching sleeve tape	Lockstitch machine	0.4	-	9.1
32	Counterstitcing collar	Lockstitch machine	1.1	31	9.05
27	Sleeve placket pressing	Sleeve placket press	0.14	-	8.84
28	Attaching sleeve placket	Lockstitch machine	0.75	26,27	8.7
33	Attaching sleeves	5 Thread Overlock	1.05	32,28	7.95
34	Topstitching sleeves	Lockstitch machine	0.95	33	6.9
17	Fusing interlining to cuff	Interlining Fusing press	0.203	-	6.418
18	Runstitching two cuffs	Lockstitch machine	0.395	17	6.215
35	Side and sleeve close seaming and attaching trimming	5 Thread Overlock	1.2	34,40	5.95
40	Cutting trimmings	Manual	0.04	-	5.95
19	Cuff turning ironing	Cuff press	0.42	18	5.82
20	Topstitching cuffs	Lockstitch machine	0.65	19	5.4
36	Attaching cuffs	Lockstitch machine	1.15	35,20	4.75
37	Hemming	Lockstitch machine	0.9	36	3.6
38	Opening buttonholes	Buttonhole machine	1.5	37	2.7
39	Sewing buttons	Button sewing machine	1.3	38	1.3

Total task time of Station 1 =
0.106+0.106+0.206+0.203=0.621 min, Remaining time
(Idle time) = 0.72-0.621=0.099 min

Table 2 shows the assignment of tasks to the stations
according to the RPWM. Here, manual and machine tasks
can be assigned to the same station. With an exception,
tasks 3 and 4 can be performed consecutively by the same
worker to prepare the collar, although they require different

machine types, as tasks 27 and 28. The machine type
abbreviations used in Table 2 are as follows: 5 Thread
Overlock (5TO), Lockstitch Machine (LSM), Buttonhole
Machine (BM), Button Sewing Machine (BSM), Interlining
Fusing Press (IP), Cuff Press (CUP), Collar Press (COP),
Collar Tip Cutting and Turning Machine (CTCM), Sleeve
Placket Press (SPP), and Manual (MN).

Table 2. Assigning shirt operations to stations

Station no.	Assigned Task no.	Machine type	PWV	Predecessor tasks	Task time (min.)	Cumulative time (min.)	Idle time (min.)
Fusing							
1	1	IP	14.256	-	0.106	0.621	0.099
	12		12.362	-	0.106		
	21		11.486	-	0.206		
	17		6.418	-	0.203		
Collar preparation							
2	2	LSM	14.15	1	0.7	0.7	0.02
3	3	CTCM	13.45	2	0.3	0.55	0.17
	4	COP	13.15	3	0.25		
4 5	5	LSM	12.9	4	0.6	0.956	0.48
	6	MN	12.3	5	0.2		
	13	LSM	12.256	12	0.156		
6 7	7	LSM	12.1	6,13	0.8	1.15	0.29
	8	MN	11.3	7	0.35		
8 9	9	LSM	10.95	8	0.7	1.05	0.39
	10	MN	10.25	9	0.2		
	11	MN	10.05	10	0.15		
Front and back preparation							
10	14	LSM	12.055	-	0.4	0.4	0.32
11	15	5TO	11.655	14	0.305	0.305	0.415
12	16	LSM	11.35	14,15	0.35	0.48	0.24
	22	LSM	11.28	21	0.13		
13	23	MN	11.15	22	0.15	0.61	0.11
	24	LSM	11.46	23	0.31		
	25	MN	11.15	24	0.15		
Cuff preparation							
14	18	LSM	6.215	17	0.395	0.395	0.325
15	19	CUP	5.82	18	0.42	0.42	0.3
16	20	LSM	5.4	19	0.65	0.65	0.07
Sleeve preparation							
17	26	LSM	9.1	-	0.4	0.4	0.32
18 -19	27	SPP	8.84	-	0.14	0.89	0.55
	28	LSM	8.7	26,27	0.75		
Assembly							
20	29	5TO	11	16,23,25	0.5	0.5	0.22
21	30	LSM	10.5	29	0.6	0.6	0.12
22-23-24	31	LSM	9.9	11,30	0.85	1.95	0.21
	32	LSM	9.05	31	1.1		
25 - 26	33	5TO	7.95	32,28	1.05	1.05	0.39
27 - 28	34	LSM	6.9	33	0.95	0.99	0.45
	40	MN	5.95		0.04		
29 - 30	35	5TO	5.95	34,40	1.2	1.2	0.24
31 - 32	36	LSM	4.75	35,20	1.15	1.15	0.29
33 - 34	37	LSM	3.6	36	0.9	0.9	0.54
35 - 36	38	BM	2.7	37	1.4	1.4	0.04
37 - 38	39	BSM	1.3	38	1.3	1.3	0.14

The fact that there are tasks that cannot be assigned to the same station and that the unit times of the jobs are distributed over a wide range prevent the station times from being well balanced. Thirty-eight stations were opened to complete all task assignments using the RPWM under the determined conditions. Accordingly, the balance efficiency is 75.4%.

$$E\,(\%) = (sum\ of\ task\ times)/(cycle\ time \times number\ of\ workstations\,)$$

$$E\,(\%) = \frac{20.617\ min}{0.72\ min \times 38\ workstations} = 75.4\%$$

3.2 Balancing the line with the proposed mathematical model

The proposed IP model was modified, resulting in different versions to apply to the ALBP of shirt production under various operating conditions. The optimal results obtained using these models are presented in Tables 3 to 9.

The models have the following characteristics that differ from the original IP model in Section 2.2.

Model 1 (Original Model): Manual and machine tasks cannot be assigned to the same workstation. Also, there is no limit to the number of tasks assigned to a station, and the interlining operations with task numbers 1, 12, 17, and 21 are to be assigned to the first stage. Accordingly, the solution of Model 1 is given in Table 3.

Model 2: Manual tasks can be allocated to the same workstation with machine tasks. This operational flexibility is reflected in the proposed model by replacing Constraint (5) with Constraints (5a) -(5b) given below. Also, there is no limit to the number of tasks assigned to a station, as in Model 1. Accordingly, the solution of Model 2 is given in Table 4.

$$\sum_{i=1}^{N} x_{is} \cdot t_i \le C \cdot z_{sm} \qquad \forall\ s,m \tag{5a}$$

$$A_{im} \cdot x_{is} \le y_{sm} \qquad \forall i,s,m \mid m > 1 \tag{5b}$$

Model 3: It is the same as Model 2. Besides, tasks 3 and 4 and 27 and 28, although requiring different machine types, can be assigned to the same station. Equation (18) must be added to the model for these task pairs. The solution of Model 3 is given in Table 5.

$$x_{is} - x_{js} = 0 \qquad \forall\ (i,j) \in \{(3,4),(27,28)\} \tag{18}$$

Model 4: It is the same as Model 3, except that a maximum of three tasks can be assigned to a station. This limitation does not apply to the interlining operations corresponding to task numbers 1,12,17, and 21, respectively, assigned to the first stage of the assembly line. The solution of Model 4 is given in Table 6.

Model 5: It is the same as Model 4, except that a maximum of two tasks can be assigned to a station instead of three. The solution of Model 5 is given in Table 7.

Model 6: It is the same as Model 4. The objective of this model is different from the other models, as given in Equation 19. Whereas the original model only minimizes the number of stations, i.e., the number of operators working on the assembly line, this model prioritizes the assignment of relevant tasks, such as tasks processed on the same piece of the shirt, to the same station where possible or nearby stations to minimize excessive transportation of such parts between workstations and the parameter w_2 indicates the importance weight of this objective. After then, it tries to minimize the number of stations for which the parameter w_1 specifies the importance weight of this objective. Here $w_1 = 1$ and $w_2 = 10$. The model requires Equation (20) as an additional constraint to determine whether task pairs that belong to the same piece of the shirt and in a precedence relation $((i,j) \in Derived\,)$ are assigned to a different stage. The variable dev_{ij} takes a value greater than zero when tasks in pair (i,j) is assigned to different stages and takes 0 when assigned to the same stage. The solution of Model 6 is given in Table 8.

$$Minimize\ w_1 \sum_{s=1}^{S} \sum_{m=1}^{M} z_{sm} + w_2 \sum_{(i,j)\in Derived} dev_{ij} \tag{19}$$

$$dev_{ij} = \sum_{s=1}^{S} s.x_{js} - \sum_{s=1}^{S} s.x_{is} \qquad \forall\ (i,j) \in Derived \tag{20}$$

Model 7: It is the same as Model 6. However, this time, the model's objective prioritizes minimizing the number of stations and then tries to assign relevant tasks closely. Here $w_1 = 10$ and $w_2 = 1$. This model consists of 1417 constraints and 1313 variables. The LINGO code for Model 7 is given in the Appendix, and the solution of Model 7 is given in Table 9.

In all models, interlining processes are gathered in a single station in accordance with the real case. Generally, workers perform manual tasks such as regulation, turning, and cutting in stations reserved for manual tasks only. As indicated, Model 1 uses separate stations for manual tasks, and the Model 1 solution consists of 36 stations, with three having only manual tasks performed. According to Model 2, manual tasks can be assigned to the same station together with machine tasks. With this flexibility, Model 2 reduces the number of stations needed to carry out the tasks from 36 to 34. Instead of assigning manual tasks to separate stations, assigning them to the same station with other machine tasks reduces remaining idle time at the stations and provides more efficient use of total station processing time.

In Model 3, binary tasks 3 and 4 and 27 and 28 are assigned to the same stations, although performed on different machine types. This assignment is allowed since they are already processed successively in the company. This reduces the number of stations needed to perform the tasks to 32, compared to 34 stations using Model 2. However, since there is no limit to the number of tasks assigned to a station, some stations have been assigned four tasks.

Although several different task allocations to a station help make the line more efficient, it can cause disruptions in the workflow and raise quality problems in practice.

Table 3. The solution of Model 1

Station no.	Machine type	Assigned task no.	Total task time	Avg. station time
1	LSM	24, 26	0.71	0.71
2	IP	1,12,17,21	0.62	0.62
3	LSM	2	0.7	0.7
4	LSM	13,18,22	0.68	0.68
5	LSM	14	0.4	0.4
6	CTCM	3	0.3	0.3
7	COP	4	0.25	0.25
8	LSM	5	0.6	0.6
9	MN	6,23,25	0.5	0.5
10	5TO	15	0.31	0.31
11,12	LSM	7,16	1.15	0.58
13	5TO	29	0.5	0.5
14	MN	8	0.35	0.35
15,16	LSM	9,30	1.3	0.65
17	MN	10,11,27,40	0.53	0.53
18	CUP	19	0.42	0.42
19,20,21,22	LSM	28,31,32	2.7	0.68
23,24	5TO	33	1.05	0.53
25,26	LSM	34	0.95	0.48
27,28	5TO	35	1.20	0.6
29	LSM	20	0.65	0.65
30,31,32	LSM	36,37	2.05	0.68
33,34	BM	38	1.40	0.7
35,36	BSM	39	1.30	0.65

Table 4. The solution of Model 2

Station No.	Machine type	Assigned task no.	Total task time	Avg. station time
1	IP	1,12, 17,21	0.62	0.62
2,3	LSM	2,13,22,26	1.39	0.69
4	LSM	14,24	0.71	0.71
5	5TO, MN	15,25	0.46	0.23
6	LSM	16	0.35	0.35
7	5TO, MN	23,29,40	0.69	0.69
8	CTCM	3	0.3	0.3
9	COP	4	0.25	0.25
10	LSM	5	0.6	0.6
11,12	LSM, MN	6,7,18	1.39	0.70
13	SPP, MN	8,27	0.49	0.49
14,15,16	LSM	9,28,30	2.05	0.68
17	CUP, MN	10,19	0.62	0.62
18,19,20	LSM, MN	11,31,32	2.1	0.7
21,22	5TO	33	1.05	0.53
23,24,25	LSM	20,34	1.6	0.53
26,27	5TO	35	1.2	0.6
28,29,30	LSM	36,37	2.05	0.68
31,32	BM	38	1.4	0.7
33,34	BSM	39	1.3	0.65

Table 5. The solution of Model 3

Station no.	Machine type	Assigned task no.	Total task time	Avg. station time
1	IP, MN	1,12,17,21,40	0.66	0.66
2,3	LSM, MN	2,22,24,25	1.29	0.65
4	CTCM, COP, MN	3,4,23	0.70	0.70
5,6,7	LSM	5,6,7,13,14	2.16	0.72
8	5TO	8,15	0.66	0.66
9,10	LSM	9,16	1.05	0.53
11	5TO	10,29	0.70	0.70
12,13,14	LSM, SPP	26,27,28,30	1.89	0.63
15,16,17	LSM	11,31,32	2.10	0.70
18,19	5TO	33	1.05	0.53
20,21	LSM	18,34	1.35	0.67
22	CUP	19	0.42	0.42
23	LSM	20	0.65	0.65
24,25	5TO	35	1.20	0.60
26,27,28	LSM	36,37	2.05	0.68
29,30	BM	38	1.40	0.70
31,32	BSM	39	1.30	0.65

In Model 4, the maximum number of tasks assigned to the stations is limited to three, thus increasing the number of stations required to perform the tasks from 32 stations found using Model 3 to 33. According to this model solution, successive tasks requiring the same machine type are mostly assigned to the same station. The sum of task times at the stations is quite well-balanced. Station 15, where only manual tasks are assigned, has the highest idle time among other stations. The stations involving manual and machine tasks are relatively better balanced.

In Model 5, when the maximum number of tasks assigned to a station is limited to two, the number of open workstations increases to 35 from 33 stations found using Model 4. The similarity between the average station times is distorted compared to Model 4 since the stations cannot be sufficiently balanced due to the task number limitation and the tasks' wide range of operation times.

Table 6. The solution of Model 4

Station no.	Machine type	Assigned task no.	Total task time	Avg. station time
1	IP	1,12,17,2	0.62	0.62
2	LSM	2	0.70	0.70
3	CTCM, COP	3,4	0.55	0.55
4	LSM	5	0.60	0.60
5	LSM	13,14,22	0.69	0.69
6,7	LSM, MN	6,7,18	1.40	0.70
8	5TO, MN	8,15	0.66	0.66
9	LSM	9	0.70	0.70
10	CUP, MN	10,19	0.62	0.62
11,12	LSM, SPP	26,27,28	1.29	0.65
13	LSM	20	0.65	0.65
14	LSM	16,24	0.66	0.66
15	MN	23,25,40	0.34	0.34
16	5TO, MN	11,29	0.65	0.65
17	LSM	30	0.60	0.60
18,19,20	LSM	31,32	1.95	0.65
21, 22	5TO	33	1.05	0.53
23,24	LSM	34	0.95	0.48
25,26	5TO	35	1.20	0.60
27,28,29	LSM	36,37	2.05	0.68
30,31	BM	38	1.40	0.70
32,33	BSM	39	1.30	0.65

Table 7. The solution of Model 5

Station No.	Machine type	Assigned task no.	Total task time	Avg. station time
1	IP	1,12,17,21	0.621	0.621
2	LSM	14,24	0.71	0.71
3	LSM	2	0.7	0.7
4	CTCM, COP	3,4	0.55	0.55
5	LSM	5	0.6	0.6
6	LSM, MN	6,13	0.356	0.356
7	LSM	18	0.395	0.395
8	LSM	22,26	0.53	0.53
9,10	LSM, MN	7,25	0.95	0.48
11	5TO, MN	8,15	0.66	0.66
12	LSM	9	0.70	0.70
13	LSM, MN	10,16	0.55	0.55
14	5TO, MN	23,29	0.65	0.65
15	LSM	30	0.60	0.60
16	CUP, MN	11,19	0.57	0.57
17,18	LSM, SPP	27,28	0.89	0.45
19, 20, 21	LSM	31,32	1.95	0.65
22,23	5TO, MN	33,40	1.09	0.55
24	LSM	20	0.65	0.65
25,26	LSM	34	0.95	0.48
27,28	5TO	35	1.20	0.60
29,30,31	LSM	36,37	2.05	0.68
32,33	BM	38	1.40	0.70
34,35	BSM	39	1.30	0.65

Models 6 and 7 were run with opposite priorities in fulfilling the objectives. In Model 6, the priority is to assign the jobs close to each other according to their precedence relations. Thirty-five stations have been used to allocate the tasks. The average processing times of stations 13, 14, and 15 are well below the cycle time. Since the tasks at these stations require different machines and must be performed in sequence, they have been assigned to separate stations consecutively. Thus, these stations are not working efficiently enough.

On the other hand, the movement of different workpieces of the shirt between stations has been reduced by successively assigning tasks to stations 3, 7, 9, 10, 11, 12, 16, and 17. Model 7 prioritizes the number of stations needed to complete the assembly work and assigns 33 stations. In this model, except for station 14, the average processing times of the stations are in a narrower range. Since the priority is to minimize the number of stations, only the appropriate consecutive tasks are assigned to the same station. Unlike Model 6, sequential manual tasks 8, 10, and 11 are assigned to different stations for more efficient balancing instead of being assigned to the same station.

Models 4 and 7 require a minimum of 33 stations to allocate all tasks. Since Model 7 tries assigning close tasks together as the second criterion, three consecutive tasks have been assigned one after the other to stations 3, 8, and 9. With this assignment, less work will have to be moved between stations than in Model 4. Therefore, Model 7 presents the most appropriate solution to this line-balancing problem.

Model 3 has the highest value of 89.5% in terms of efficiency. However, in this model, there are two stations with five tasks allocated and one station with four tasks. Model 7 is more appropriate in this regard since assigning many tasks to a station can disrupt the workflow. The assembly line layout for the solution of Model 7 is given in Figure 2. The RPWM has performed worse than all the models considering the balance efficiency, as illustrated in Table 10.

When considering all these models, Model 7 is thought to be more suitable regarding the layout of the machines, although it does not have the highest efficiency. In Model 7, the predecessors of tasks 13, 18, and 22 at station 2 are performed at station 1, where the interlining operation is performed. These tasks are not difficult concerning their level of practicality. In this respect, a similar interpretation can be made for tasks at station 3. As in many shirt businesses, tasks 3 and 4 of station 7 are carried out successively by the same worker. It is also observed that several manual tasks are assigned to stations, and tasks such as collar fitting (task no. 31) and sleeve fitting (task no. 33), which have a high degree of difficulty, are not assigned together.

According to these different scenarios considered by the models, assigning manual and machine tasks together contributes greatly to achieving workstation times close to the cycle time and ensuring a smooth workflow. Similar practices are also done in assigning and organizing tasks in modular production plants where the operators are initially assigned to perform tasks carried out with the sewing machine, and then they are assigned to manual tasks to fill the leisure time after these tasks are completed. It may be assumed that machine operators can also carry out manual tasks.

Table 8. The solution of Model 6

Station no.	Machine type	Assigned task no.	Total task time	Avg. station time
1	IP	1,12,17,21	0.621	0.621
2	LSM	13,18,22	0.681	0.681
3	LSM, MN	23,24,25	0.61	0.61
4	CUP	19	0.42	0.42
5,6	LSM	2,20	1.35	0.68
7	CTCM, COP	3,4	0.55	0.55
8	LSM	5	0.6	0.6
9,10	LSM, MN	6,7,8	1.35	0.675
11,12	LSM, MN	9,10,11	1.05	0.525
13	LSM	14	0.4	0.4
14	5TO	15	0.305	0.305
15	LSM	16	0.35	0.35
16,17	LSM, SPP	26,27,28	1.29	0.645
18	5TO, MN	29,40	0.54	0.54
19	LSM	30	0.6	0.6
20,21,22	LSM	31,32	1.95	0.65
23,24	LSM	33	1.05	0.525
25,26	LSM	34	0.95	0.475
27,28	5TO	35	1.2	0.6
29,30,31	LSM	36,37	2.05	0.68
32,33	BM	38	1.4	0.7
34,35	BSM	39	1.3	0.65

Table 9. The solution of Model 7

Station no.	Machine type	Assigned task no.	Total task time	Avg. station time
1	IP	1,12,17,21	0.621	0.621
2	LSM	13,18,22	0.681	0.681
3	LSM, MN	23,24,25	0.61	0.61
4	CUP	19	0.42	0.42
5	LSM	20	0.65	0.65
6	LSM	2	0.7	0.7
7	CTCM, COP	3,4	0.55	0.55
8,9	LSM, SPP	26,27,28	1.29	0.645
10	LSM	5	0.6	0.6
11,12	LSM, MN	6,7,14	1.35	0.675
13	5TO, MN	8,15	0.655	0.655
14	LSM	16	0.35	0.35
15	LSM	9	0.7	0.7
16	5TO, MN	10,29	0.7	0.7
17	LSM, MN	30,40	0.64	0.64
18,19,20	LSM, MN	11,31,32	2.1	0.7
21,22	5TO	33	1.05	0.525
23,24	LSM	34	0.95	0.475
25,26	5TO	35	1.2	0.6
27,28,29	LSM	36,37	2.05	0.68
30,31	BM	38	1.4	0.7
32,33	BSM	39	1.3	0.65

Table 10. Line efficiency values of all solutions

Models	Number of workstations	Efficiency %
Model 1	36	79.5
Model 2	34	84.2
Model 3	32	89.5
Model 4	33	86.8
Model 5	35	81.9
Model 6	35	81.9
Model 7	33	86.8
RPWM	38	75.4

Regarding the applicability of the proposed models in the factory environment, some other factors may need to be considered. In the business environment, task times may fluctuate within a given range, and workers may not be eligible to operate all machines and perform all tasks. On the other hand, it should be noted that, with the recent increase in model diversity, the changing competitive conditions have increased businesses' expectations for more workers to perform different tasks and use different machinery, and the companies have started training their workers subsequently.

4. CONCLUSION

In the literature on assembly line balancing, heuristic line balancing methods and simulation models have been widely used to balance single-model assembly lines. This paper has developed a unique balancing model for assembly lines that incorporates labor and machine constraints, parallel workstations, and task assignment restrictions to achieve the highest line efficiency using optimum labor and machinery for a fixed cycle time. In the first phase of the application, line balancing is performed using the RPWM. In the second phase, seven IP models are developed and implemented under various scenarios, and the results of their solutions are compared.

The line efficiency of the shirt sewing line is 75.4% for the RPWM, and the most appropriate IP model (Model 7) has resulted in 86.8% efficiency. Production speed is critical in the apparel industry. Setting up and balancing an assembly line takes time. With the developed IP model, establishing the line and assigning tasks can be found optimally quickly. Especially in multi-process models, the IP model with the given constraints can quickly create different line designs, and the most efficient design can be reached quickly.
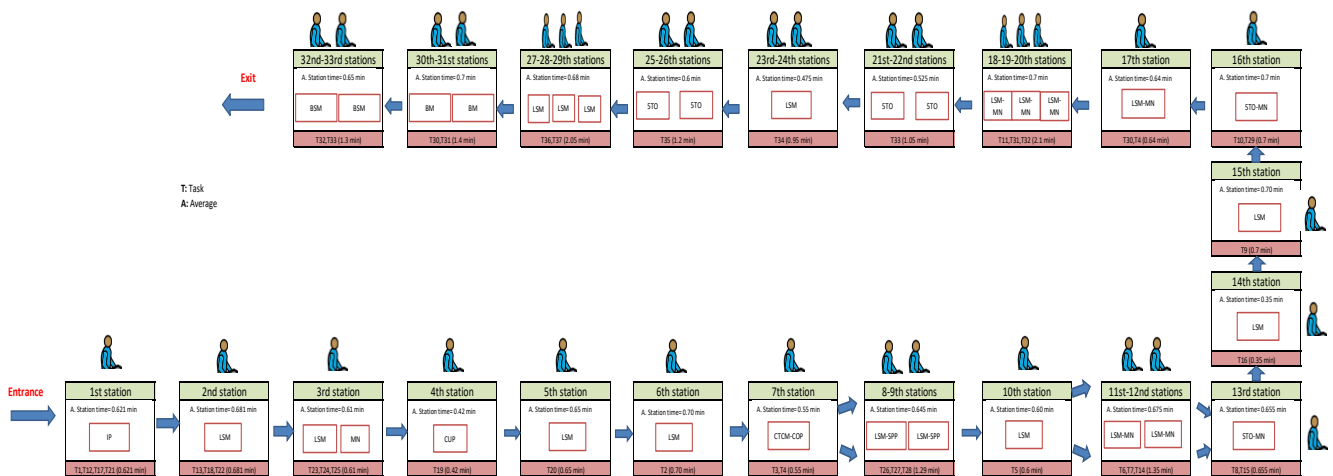

Figure 2. The layout of the assembly line for the Model 7 solution

In this research, different mathematical models were created; it has been seen that instead of doing the manual tasks at separate stations, their assignment with machine-operated tasks ensures that the station times are comparatively better balanced. Moreover, when there is no limitation on the number of tasks assigned to stations, the overall number of stations required to complete all tasks reduces, and the line efficiency increases; however, this way of the assignment of tasks is hard to implement within the enterprise since it increases the risk of poor product quality.

The proposed IP model can be run under different operating constraints. For this reason, companies can practically use the model to find the most suitable balancing solution. For future research, the model can be extended for mixed-model ALBPs. Also, it can be modified to include the limitation that the workers can only use certain machine types.

REFERENCES

1. Cercioglu H, Ozcan U, Gokcen H, Toklu B. 2009. Paralel Montaj Hattı Dengeleme Problemleri İçin Bir Tavlama Benzetimi Yaklaşımı. *Gazi Üniversitesi Mühendislik ve Mimarlık Fakültesi Dergisi* 24(2), 331-341.

2. Eryuruk SH, Kalaoglu F, Baskak M. 2008. Assembly Line Balancing in a Clothing Company. *Fibres & Textiles in Eastern Europe* 16(1), 93-98.

3. Kriengkorakot N, Pianthong N. 2007. The Assembly Line Balancing Problem: Review Articles, *KKU Engineering Journal* 34(2), 133-140.

4. Kursun S, Kalaoglu F. 2010. Line Balancing by Simulation in a Sewing Line. *Tekstil ve Konfeksiyon* 20(3), 257-261.

5. Kayar M, Akalin M. 2016. Comparing Heuristic and Simulation Methods Applied to the Apparel Assembly Line Balancing Problem. *Fibres & Textiles in Eastern Europe* 24(2), 131-137.

6. Unal C, Tunali S, Güner M. 2009. Evaluation of Alternative Line Configurations in Apparel Industry Using Simulation. *Textile Research Journal* 79(10), 908-916.

7. Unal C, Bilget S. 2021. Examination of Lean Manufacturing Systems by Simulation Technique in Apparel Industry. *The Journal of the Textile Institute* 112(3), 377-387.

8. Unal C, Demirbas ZA. 2018. Creating an Alternative Production Line by Using a Simulation Technique in Duvet Cover Production. *Fibres & Textiles in Eastern Europe* 26(4), 8-12.

9. Eryuruk SH, Kalaoglu F, Baskak M. 2011. Assembly Line Balancing by Using Statistical Method in Clothing Production. *Tekstil ve Konfeksiyon* 21(1), 65-71.

10. Guner M, Yucel O, Unal C. 2013. Applicability of Different Line Balancing Methods in the Production of Apparel. *Tekstil ve Konfeksiyon* 23(1), 77-84.

11. Karabay G. 2014. A Comparative Study on Designing of a Clothing Assembly Line. *Textile and Apparel* 24(1), 124-133.

12. Unal C. 2013. A New Line Balancing Algorithm for Manufacturing Cell Transformation in Apparel Industry. *Industria Textila* 64(3), 155-162.

13. Turkmen A, Yesil Y, Kayar M. 2016. Heuristic Production Line Balancing Problem Solution with MATLAB Software programming. *International Journal of Clothing Science and Technology* 28(6), 750-779.

14. Jirasirilerd G, Pitakaso R, Sethanan K, Kaewman S, Sirirak W, Kosacka-Olejnik M. 2020. Simple Assembly Line Balancing Problem Type 2 by Variable Neighborhood Strategy Adaptive Search: A Case Study Garment Industry. *Journal of Open Innovation:Technology, Market and Complexity* 6(21), 1-21.

15. Bongomin O, Mwasiagi JI, Nganyi EO, Nibikora I. 2020. Improvement of Garment Assembly Line Efficiency Using Line Balancing Technique. *Engineering Reports* 2, 1-18.

16. Kayar M, Akalin M. 2014. A Research on the Effect of Method Study on Production Volume and Assembly Line Efficiency. *Tekstil ve Konfeksiyon* 24(2), 228-239.

17. Ahmed T, Sakib N, Hridoy RM, Shams AT. 2020. Application of Line Balancing Heuristics for Achieving an Effective Layout: A Case Study. *International Journal of Research in Industrial Engineering* 9(2), 114–129.

18. Kayar M, Akyalçin ÖC. Applying Different Heuristic Assembly Line Balancing Methods in the Apparel Industry and their Comparison. *Fibres & Textiles in Eastern Europe* 2014; 22, 6(108): 8-19.

19. Phan, TT, Le, TMA, Phan, DN, Tran, NS. (2022). Researching the Optimal Method of Balancing the Sewing Line with T-Shirt Product in the Garment Industry in Vietnam. ECS Transactions, 107(1), 7869.

20. Gursoy A. 2012. An Integer Model and a Heuristic Algorithm for the Flexible Line Balancing Problem. *Tekstil ve Konfeksiyon* 22(1), 58-63.

21. Gursoy A, Gursoy N. 2015. On the Flexibility Constrained Line Balancing Problem in Lean Manufacturing. *Tekstil ve Konfeksiyon* 25(4), 345-351.

22. Xu H, Xu B, Yan J. 2019. Balancing Apparel Assembly Lines Through Adaptive Ant Colony Optimization. *Textile Research Journal* 89(18), 3677–3691.

23. Ahmed N, Ador MSH. 2020. Multi-Objective Mixed Model Assembly Line Balancing Using Mixed Integer Linear Programming. *American Journal of Industrial Engineering* 7(1), 14-25.

24. Helgeson WP, Birnie DP. 1961. Assembly Line Balancing Using the Ranked Positional Weight Technique. *Journal of Industrial Engineering*, 12(6), 384-398.

25. LINGO. 2015. *The Modeling Language and Optimizer*. Chicago, Illinois: LINDO Systems Inc.

APPENDIX

The LINGO program for the IP model of Model 7 is given below. The constraint numbers are the same as in the manuscript for an easy follow-up.

Sets:

Tasks/1..40/:t;

Stages/1..24/;

Precedences(Tasks,Tasks)/1 2, 2 3, 3 4, 4 5, 5 6, 6 7, 13 7, 7 8, 8 9, 9 10, 10 11, 12 13, 14 15, 14 16, 15 16, 17 18, 18 19, 19 20, 21 22, 22 23, 24 25, 26 28, 27 28,16 29, 23 29, 25 29, 29 30, 11 31, 30 31, 31 32, 32 33, 28 33, 33 34, 34 35, 40 35, 35 36, 20 36, 36 37, 37 38, 38 39/;

MachineType/Manuel,Pres,Duz, Yum, 5Ip, Mup, Im, Dm/:TM;

Derived(Tasks,Tasks)/1 2, 2 3, 3 4, 4 5, 5 6, 6 7, 7 8, 8 9, 9 10, 10 11, 12 13, 14 15, 14 16, 15 16, 17 18, 18 19, 19 20, 21 22, 22 23, 23 24, 24 25, 26 28, 27 28,29 30, 30 31, 31 32, 32 33, 33 34, 34 35, 35 36, 36 37, 37 38, 38 39/: dev;

Stages_MachineType(Stages,MachineType):z,y;

Tasks_Stages(Tasks,Stages):x;

Tasks_MachineType(Tasks,MachineType):A;

Together/1,12,17,21/;

Endsets

Data:
C=0.72;
t=0.106, 0.7, 0.3, 0.25, 0.6, 0.2, 0.8, 0.35, 0.7, 0.2, 0.15, 0.106, 0.156, 0.4, 0.305, 0.35, 0.203, 0.395, 0.42, 0.65, 0.206, 0.13, 0.15, 0.31, 0.15, 0.4, 0.14,
0.75, 0.5, 0.6, 0.85, 1.1, 1.05, 0.95, 1.2, 1.15, 0.9, 1.4, 1.3, 0.04;
TM=0,1,28,1,7,1,2,2; TW=38; K=3;
A=0 1 0 0 0 0 0 0
 0 0 1 0 0 0 0 0
 0 0 0 1 0 0 0 0
 0 0 0 1 0 0 0 0
 0 0 1 0 0 0 0 0
 1 0 0 0 0 0 0 0
 0 0 1 0 0 0 0 0
 1 0 0 0 0 0 0 0
 0 0 1 0 0 0 0 0
 1 0 0 0 0 0 0 0
 1 0 0 0 0 0 0 0
 0 1 0 0 0 0 0 0
 0 0 1 0 0 0 0 0
 0 0 1 0 0 0 0 0
 0 0 0 0 1 0 0 0
 0 0 1 0 0 0 0 0
 0 1 0 0 0 0 0 0
 0 0 1 0 0 0 0 0
 0 0 0 0 0 1 0 0
 0 0 1 0 0 0 0 0
 0 1 0 0 0 0 0 0
 0 0 1 0 0 0 0 0
 1 0 0 0 0 0 0 0
 0 0 1 0 0 0 0 0
 1 0 0 0 0 0 0 0
 0 0 1 0 0 0 0 0
 0 0 1 0 0 0 0 0
 0 0 1 0 0 0 0 0
 0 0 0 0 1 0 0 0
 0 0 1 0 0 0 0 0
 0 0 1 0 0 0 0 0
 0 0 1 0 0 0 0 0
 0 0 0 0 1 0 0 0
 0 0 1 0 0 0 0 0
 0 0 0 0 1 0 0 0
 0 0 1 0 0 0 0 0
 0 0 1 0 0 0 0 0
 0 0 0 0 0 0 1 0
 0 0 0 0 0 0 0 1
 1 0 0 0 0 0 0 0;

Enddata
!Objective function(1): Minimize the total number of open workstations;
!min=@sum(Stages_MachineType(s,m):z(s,m));

!Model 7 Objective Function (Equation 19);

min=10*@sum(Stages_MachineType(s,m):z(s,m)) + @sum(Derived(i,j):dev(i,j)) ;

!Constraint(2): Each task must be assigned to a stage;
@for(Tasks(i):@sum(Stages(s):x(i,s))=1);

!Constraint(3): At most one machine type can be assigned to a stage;
@for(Stages(s):@sum(MachineType(m):y(s,m))<=1);

!Constraint(4): Precedence relations among the tasks are provided;
@for(Precedences(i,j):@sum(Stages(s):s*x(j,s))-@sum(Stages(s):s*x(i,s))>= 0);

!Constraint(5): The sum of the processing times of the tasks assigned to a stage must not exceed the cycle time multiplied by the number of open workstations;
!@for(Stages_MachineType(s,m):@sum(Tasks(i)|A(i,m) #EQ# 1 :x(i,s)*t(i))<=C*z(s,m));

!Constraint(5a);
@for(Stages(s):@sum(Tasks(i):x(i,s)*t(i))<= @sum(MachineType(m):C*z(s,m)));

!Constraint(5b);
@for(Stages_MachineType(s,m) | m #gt# 1 :@for(Tasks(i)|A(i,m) #EQ# 1 :x(i,s)<= y(s,m)));

!Constraint(6): The number of machines of a certain type assigned to a stage can only be positive when the same machine type is assigned to the stage.
@for(Stages_MachineType(s,m)| m #GT#1: z(s,m)<=TM(m)*y(s,m));

!Constraint(7): The relation between z(s,m) and y(s,m) variables is provided;
@for(Stages_MachineType(s,m):z(s,m)>=y(s,m));

!Constraint(8): The number of workers assigned to work on the assembly line should not exceed the number of workers available;
@sum(Stages_MachineType(s,m): z(s,m))<= TW;

!Constraint(9): The number of parallel stations allowed in a stage should not exceed the specified number;
@for(Stages(s)| s #ne# 1: @sum(Tasks(i): x(i,s)) <=3;);
@for(Stages(s)| s #eq# 1: @sum(Tasks(i): x(i,s)) <=4);

!Constraint(10): The number of machines allocated to the assembly line of each type should not exceed the available number;
@for(MachineType(m) | m #GT# 1: @sum(Stages(s):z(s,m))<=TM(m));

!Constraint(11): The specified tasks are assigned to the first stage at the beginning;
x(1,1)=1;
x(12,1)=1;
x(17,1)=1;
x(21,1)=1;

!Constraint(12):;
@for(Stages(s) | s #LT# 24:@sum(MachineType(m):y(s,m))>=@sum(MachineType(m):y(s+1,m)));

!Constraint(13): Binary Constraints;
@for(Tasks_Stages(i,s):@bin(x(i,s)));
@for(Stages_MachineType(s,m):@bin(y(s,m)));

!Constraint(14): Integer Constraints;
@for(Stages_MachineType(s,m):@gin(z(s,m)));

!Constraint(18): The task pairs that must be assigned to the same workstation are specified;
@for(Stages(s): x(27,s)-x(28,s)=0);
@for(Stages(s): x(3,s)-x(4,s)=0);

!Equation(20);
@for(Derived(i,j): dev(i,j)=@sum(stages(s): s*x(j,s))- @sum(stages(s): s*x(i,s)));

Biologically Degummed and Chemically Treated Okra Bast Fibers-Reinforced Poly(Vinyl Alcohol) Composites

Gazi Md Arifuzzaman Khan[1] ID 0000-0002-4233-9868
Nazire Deniz Yılmaz[2] ID 0000-0002-8605-774X

[1]Department of Applied Chemistry and Chemical Engineering, Islamic University, Kushtia, Bangladesh
[2]Department of Textile Engineering, Faculty of Engineering, Uşak University, Uşak, Türkiye

Corresponding Author: Nazire Deniz Yılmaz, naziredyilmaz@gmail.com

ABSTRACT

This paper focuses on preparation of poly(vinyl alcohol) (PVA)-based composite films reinforced with okra bast fibers at different percentages of 5, 10, 20% via solution casting method. Fibers obtained from different sections of okra plants were biologically degummed and scoured with Na_2CO_3. Selected fibers were bleached, treated with maleic anhydride or grafted with vinyl acetate. Mechanical, physical and biodegradational properties of the composites were investigated. The tensile strength of the produced composites ranges between 33.8 and 55.1 MPa, elasticity modulus from 1.8 to 2.6 GPa, elongation rate at break varies in 2.8-10%. Chemical treatments led to improved mechanical performance whereas increased fiber content reduces tensile strength, stiffness and elongation, as well as water absorption. Fiber addition significantly affected biodegradation in a complicated way: by decelerating mass loss but accelerating deterioration of mechanical properties.

1. INTRODUCTION

Biopolymers and biocomposites have gained notable consideration over the last few decades. The main advantages of biopolymers are their biodegradability and the reduction of carbon dioxide emissions. Polyvinyl alcohol (PVA), is a kind of biodegradable and water-soluble polymer that can be utilized in an array of applications such as agricultural mulch films, biodegradable packaging, food coating, fuel cells, paper covering, textile sizing agents, etc. [1-3]. Due to its excellent processability and biocompatibility, it has found use in blends and composites with various natural polymers including starch, chitosan, cellulose, fibroin, or lignocellulosic fillers [4]. The hydrophilic PVA is compatible with lignocellulose fibers. –OH groups of natural fibers can link to the –OH groups of PVA via hydrogen bonds [5].

Lignocellulosic fibers are renewable and abundantly available materials on the globe composed mainly of cellulose, lignin, and hemicellulose. Those fibers can be obtained from traditional fiber crops as well as from agro-residual sources. Recently, agro-residual fiber sources get a priority to scientists because those crops serve two purposes simultaneously: food production and fiber production. Some agro-residual fibers obtained from agricultural residues such as okra stem [6], coir [7], banana fruit and bunch stems [8], corn husk [9], cotton straw [10], pineapple leaf [11], enset [12] etc. have proven their potential as a raw material in textiles and composites industries. Due to bearing high cellulose content, high tensile strength, stiffness, and aspect ratio; okra bast fiber has been used to make a composite with a variety of polymers viz. polypropylene [13], epoxy [14], light density polythylene (LDPE) [15], etc. The composites of PVA and okra fiber may also have the prospective to produce materials with excellent mechanical properties and promising performance.

The performance of PVA/lignocellulose fibers composites depends on processing methods, quality of filler, filler distribution, compatibility of filler and matrix, etc. Though both PVA and cellulose contain hydroxyl groups, their composites provide poor moisture resistance which reduces mechanical properties by destroying the bond between filler and matrix. Again, direct incorporation of virgin lignocellulose fibers into the PVA matrix may not always give good mechanical properties. In most cases, the –OH groups of cellulose involve either intra- or intermolecular hydrogen bonds with each other. Therefore, those cellulose molecules are not willing to react with matrix molecules, which is necessary for the mechanical strength of the composites. The strength of the composite can be improved in two ways: (i) by using cross-linking agents which increase their compatibility and (ii) by chemical treatments of fiber. For long-term durability of these composites, researchers have proposed many chemical modifications such as alkali treatment [16], plasma treatment [17], and surface modifications using silanes [18], maleic anhydride [19], vinyl monomers [20], etc. to decrease their moisture affinity.

Cinelli et al. [21] produced composites of PVA reinforced with other agro-residual materials that are obtained from corn-based ethanol production, i.e. corn fiber and corn starch, and some plasticizers including glycerol and pentaerythritol via injection molding. The corn fibers were from pericarp sections of the corn kernels. They reported tensile strength around 8 MPa, elengation rate between 400-600%, and Young's modulus in the range of 36-100 MPa. They found that mechanical properties were sustained upon soaking for 30 minutes in water and in a medium at at 50% relative humidity and 23 ºC for 1 year.

Imam et al. [22] developed cast films of PVA-based composites including cornstarch, orange fibers; and hexamethoxymethylmelamine (HMMM) as a crosslinking agent, as well as urea and glycerol as plasticizers. Orange fibers were lignocellulosic fibers obtained from remnants of orange juice production. They studied the thermal behavior, biodegradation, water permeability chemical structures of the composites.

Ching et al [23] produced PVA composites reinforced with empty fruit bunch fibers at 0,5-3 % loading percentages via casting evaporation. Empty fruit bunch fibers were obtained from oil palms. The researchers reported increased tensile strength and elasticity modulus at 1% fiber addition. The mechanical properties further increased with thermal treatment at 50 ºC for 6 h. They reported a tensile strength range from 8.25 to around 15 MPa, elasticity modulus between around 10 MPa and around 35 MPa. They reported enhanced mechanical properties with reduced fiber size.

Ali et al. [24] produced kenaf fiber-reinforced PVA composites via solution casting at fiber loading percentages 2,5,10,15, and 20%. They applied chemical treatments on the fiber which resulted in better tensile properties. Fiber addition as well as chemical treatments led to better flexural performance. The attained tensile strength values range between app. 9-18 MPa, elasticity modulus app. 36-65 MPa, and elongation rate app. 50-280%.

Parvin et al. [25] developed fibrillated cellulose fiber-reinforced PVA composites. They reported increment in tensile strength and elasticity modulus, together with decrease in elongation rate and maximum yield force in the composites upon addition of fibrillated cellulose fibers in PVA. The paper also ascribed the impact of *p*-phynelenediamine treatments of fibrillated cellulose fibers.

In the present investigation, fibers were obtained from different sections of okra stem via biological degumming and and scoured with Na_2CO_3 to prepare finer fibers by removing non-cellulosic matters. Selected okra bast fibers were then bleached, treated with maleic anhydride or vinyl acetate prior to composite preparation. The prepared composites were characterized in terms of their mechanical, physical and biodegradational properties. The effects of plant location where the fibers were extracted, and the effects of chemical treatments of okra fiber on the properties of their PVA film composites have been thoroughly investigated.

2. MATERIAL AND METHOD

2.1 Material

Okra stems were collected from a local agricultural farm in Denizli providence, Turkey. Maleic anhydride and vinyl acetate monomers were purchased from Sigma-Aldrich. Polyvinyl alcohol 72000 powder (98% hydrolyzed) was supplied from Merck, Germany. Solvents and reagents used in the investigation were analytical reagent grade.

2.2 Method

Okra bast fiber extraction and chemical treatments have been conducted as explained in the previous study [9] and is summarily described as follows:

Okra stems were divided into three different parts: upper, middle and bottom portions and kept separately in plastic bottles for water retting for 2 weeks. Then, the retted fibers were washed by running water and dried in ambient air. Following this, the fibers were scoured in 3.5g/L Na_2CO_3 and 6.5g/L soap solution at 70 °C for 30 min at a fiber to liquor ratio of 1:50 (w/v).

Some of the scoured bast fibers were alkalized in a 10 g/L NaOH solution at a fiber to liquor ratio of 1:50 (w/v) for 3 h at room temperature. Then the fibers were washed thoroughly and neutralized in a dilute acidic solution.

Another portion of the scoured fibers were bleached with 0.7 wt% sodium chlorite ($NaClO_2$) solution for 90 min at 85-95ºC at a fiber to liquor ratio of 1:50 (w/v). Throughout the process pH was maintained at 4 by using a buffer

mixture of pH 4 (acetic acid-sodium acetate) at a buffer solution to chlorite solution proportion of 1:10. After completion of bleaching, the fibers were washed thoroughly with distilled water and then treated with 0.2% (w/v) sodium meta-bi-sulfite ($Na_2S_2O_5$) solution for 20 min at a fiber to liquor ratio of (w/v). Finally, the fibers were filtered and washed thoroughly with distilled water, and dried in ambient air.

Some of the bleached fibers were treated 1% maleic anhydride (MA) in toluene at 65°C for 2h. After completing reaction, fibers were refluxed 3 times by acetone and finally dried in an electric oven.

The grafting reaction of vinyl acetate (VA) on a portion of bleached okra bast fibers was carried in N, N Dimethylformamide (DMF) at 95°C. 50 wt% VA monomer and 5 wt% pyridine were taken on the basis of fibers weight. The reaction was continued for 3 h in water bath and then refluxed by acetone. After washing several times by acetone, fibers were dried in an oven.

As reported in the previous study [9], alkalization led to decrease in linear density, tensile modulus and tenacity and increase in moisture content and breaking elongation of fibers. Effect of alkalization was more pronounced in comparison to other fiber treatments. The properties of water retted and scoured fibers can be given as linear density (10.24, 9.97, 6.97 tex), moisture content (6.79, 5.38, 6.25%), initial modulus (1557, 1823, 1876 cN/tex), breaking tenacity (28.78, 32.70, 31.22 cN/tex) and breaking elongation (1.99, 2.02, 2.03%) in the order top, middle and bottom, respectively. Those of alkalized, bleached, maleic anhydride-treated and vinyl acetate-grafted fibers are listed as linear density (8.26, 9.53, 9.04 and 10.24 tex), moisture content (7.11, 3.82, 5.44 and 3.62%), initial modulus (1044, 1862, 1784 and 1677 cN/tex), breaking tenacity (29.14,

40.69, 24.85 and 32.65 cN/tex) and breaking elongation (3.86, 2.23, 1.54 and 2.20 %), respectively [9].

Preparation of okra bast reinforced PVA composites can be explained as follows: Okra bast fibers were cut into the possible smallest size by scissors and then smashed in a ceramic mortar. PVA was dissolved in distilled water with continuous stirring using a magnetic stirrer for 1-1.5 h at a temperature around 80°C to prepare a PVA aqueous solution. The PVA and water ratio was maintained as 1:20. Pre-calculated amounts (5, 10, 20 wt% fiber with respect to PVA) of fibers were then added to the PVA solution (Table 1). The stirring was performed at the same temperature for a further 30 min. The final mixtures were then cast on a wooden mold. The films were kept to dry at room temperature for 1-2 days and then taken off from the mold. The films were dried at room temperature for a few weeks to evaporate the remaining water. Neat PVA film was also prepared in the same fashion but without the addition of fiber as the reference sample. Before characterization, composites were sized and dried in an oven at 80 °C for 2.5h.

Before characterization (in terms of density, mechanical properties and moisture content properties), the samples were conditioned at 21°C and 65% relative humidity for at least 24 h.

Densities of the composites have been determined by measuring the dimensions of the samples using a mechanical caliper and obtaining their mass by using a precision scale and calculated according to the formula below:

$$\rho = m/V, \tag{1}$$

where ρ is the density in (g/cm^3), m represents mass (g) and V stands for volume in cm^3.

Table 1. Processing parameters for okra fiber-reinforced PVA composites

Sample	Fiber location	Treatment#1	Treatment#2	Fiber content (wt%)	PVA content (wt%)	Thickness (mm)
PVA	-	-	-	0	100	0.30
5wrtop	Water retted top portion	-	-	5	95	0.32
10wrtop	Water retted top portion	-	-	10	90	0.35
20wrtop	Water retted top portion	-	-	20	80	0.35
5wrmop	Water retted middle portion	-	-	5	95	0.31
10wrmop	Water retted middle portion	-	-	10	90	0.32
20wrmop	Water retted middle portion	-	-	20	80	0.40
5wrbop	Water retted bottom portion	-	-	5	95	0.31
10wrbop	Water retted bottom portion	-	-	10	90	0.34
20wrbop	Water retted bottom portion	-	-	20	80	0.32
5atop	Mixed	Alkalization	-	5	95	0.30
10atop	Mixed	Alkalization	-	10	90	0.35
20atop	Mixed	Alkalization	-	20	80	0.38
5blop	Mixed	Bleached	-	5	95	0.30
10blop	Mixed	Bleached	-	10	90	0.32
20blop	Mixed	Bleached	-	20	80	0.40
5matop	Mixed	Bleached	Maleic anhydride	5	95	0.30
10matop	Mixed	Bleached	Maleic anhydride	10	90	0.30
20matop	Mixed	Bleached	Maleic anhydride	20	80	0.33
5vatop	Mixed	Bleached	Vinyl acetate	5	95	0.30
10vatop	Mixed	Bleached	Vinyl acetate	10	90	0.33
20vatop	Mixed	Bleached	Vinyl acetate	20	80	0.38

The tensile properties of neat PVA and composite samples were evaluated by tensile tests, performed, as prescribed by ASTM D 638, on rectangular samples 100mm×10mm. The test was carried out by using Tinius Olsen H10KT[(R)] Tester, US with QMat for Textiles[(R)] software, and the initial grip separation was 50 mm long. The load was measured by using a 500 N cell, and applied in displacement control with a crosshead speed of 5mm/min. The measurements were performed at room temperature and at least 7 samples for each formulation were tested.

The water absorption behavior was measured as per ASTM D570-98 (2010). Specimens for each sample composite were in dimensions of 100 mm×10 mm×(0.24-0.48) mm. The specimens were dried in an oven at 80°C for 2.5 h prior to testing. The specimens were weighed before being soaked in water. The specimens were immersed in water at room temperature (approximately 25°C). After 24 h, 48 h, and 72 h, specimens were taken out of the water and weighed once mositure on the surface moisture was dried with tissue paper. The moisture absorption was determined according to Eq (2):

Water absorption % = [(W-W_0) /W_0] ×100,   (2)

where W_o and W is the initial weight and the weight after water absorption, respectively.

Soil degradation test has been carried out according to soil burial degradation experiment explained in [26]. Accordingly, the composite samples were cut into 100 mm×10 mm rectangular specimens. Degradability test was carried out in a plastic container (44×30×23 cm^3) containing farmland soil having pH 7 by maintaining high relative humidity (90-95%) via sprinkling water at room temperature (25±5°C) daily. The specimens were dug out from the farmland soil after 14 days, and then washed and dried in air for 3 days and thereafter at 80°C for 2.5h in an oven. Biodegradability was measured by determining weight loss and deterioration in tensile properties of composite samples. Three specimens were tested for tensile properties of each biodegradation sample. Weight loss was calculated as follows:

Weight loss % = [(W_0-W) /W_0] ×100,   (3)

where W_o and W is the initial weight and the weight after soil degradation, respectively.

The findings were statistically interpreted by applying analysis of variance (ANOVA) test with α at 0.05 significance level.

Scanning electron microscopy (SEM) of fracture surfaces of okra bast fiber-reinforced PVA composites were obtained via use of a Zeiss EVO LS 10 scanning electron microscope, at 20 kV voltage and ×100 and ×300 magnification conditions. Composites were gold coated at a thickness of 5 nm via use of a Cressington auto 108 model sputter coater.

3. RESULTS AND DISCUSSION

3.1 Density

Density of neat PVA was measured as 0.85 g/cm^3. Density of poyl(vinyl alcohol) is reported to be 1.19- 1.31 g/cm^3 in the literature [27], whereas the bulk density of PVA is reported as low as 0.40-0.67 g/cm^3 [28]. The measured density falls between the density and bulk density of PVA. The bulk density depends on the crystalinity and packing density of the polymer and is lower than that of a single polymer chain [29]. In the composites, it is seen that addition of fibers led to slight decrease in composite density, as shown in Figure 1. Significant effect of fiber loading and fiber treatments on composite density has been detected (p values 1.27 ×10^{-13} and 0.01, respectively). Additionally, the location in the okra plant where the fibers were extracted also had significant effect on density (p value 0.0001).

3.2 Mechanical properties

Mechanical properties of composites are of prime importance and determine in which applications they can be utilized [30]. Increase in tensile strength was observed upon 5% loading of (wt) maleic anhydrite- and vinyl acetate-treated okra bast fibers (Fig 2). Findings of modulus of elasticity also agree with tensile strength data (Fig 3). On the other hand, elongation at break substantially decreased with fiber addition. The tensile strength and elasticity modulus values of the current study are greater than those of cellulosic fiber-reinforced PVA composites reported in the literaure [21], [22], [24].
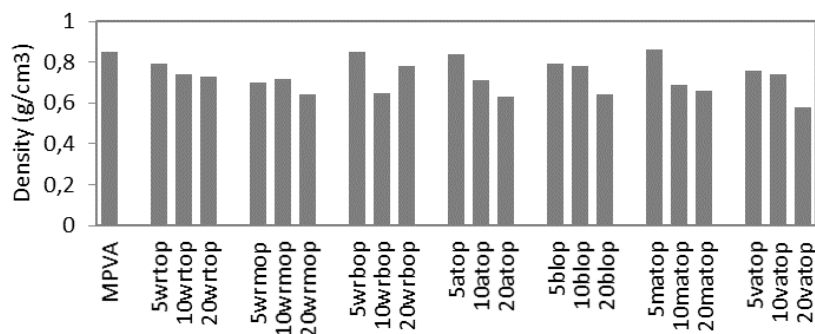

Figure 1. Measured density of 100% PVA and the okra bast fiber-reinforced PVA composites

Fiber loading and fiber treatments were found to have significant effect on tensile strength, while the part of plant, where the fibers were extracted, was not (p values $1.09×10^{-6}$, $7.8×10^{-4}$, and 0.19, respectively). For all batches tensile strength is in descending order for 5%>10%>20% fiber loading. Fiber loading at rates lower than 5% can be tried for future research. Rahman et al. [31] reported increased mechanical strength and stiffness of PVA-based composites until a loading of 9% crystalline cellulose of jute and reduction in mechanical performance for higher loading percentages due to possible agglomeration. Ali et al. [24] reported decreased tensile strength of PVA composites with increase in reinforcing kenaf fiber percentage. In the current study chemically treated okra bast fibers tend to result in higher strength in comparison to scoured okra bast fibers. Similarly, Ali et al. [24] reported improved strength from chemically treated kenaf fiber-reinforced PVA composites. The section of the plant where the fibers were extracted was not found to have significant effect on tensile strength. The reason for this may be the fact the differences in mechanical properties among fibers obtained from different parts of the plant are lower than those among differently treated fibers. In the previous study [9], increased breaking was reported increased tenacity upon bleaching and reduced breaking tenacity for alkalization and maleic anhydride treatment for okra bast fibers. Maleic abhydride-treated

fibers showed the lowest tenacity and breaking alongation among differently treated fibers, whereas maleic anhydride-treated okra fiber-reinforced composite films show the greatest strength among studied composite films. Tensile findings of the composites and fibers can be interpreted as the surface chemistry of the fibers, and in turn compatibility with the matrix, are reflected more in the strength of the produced composites than differences in fiber tenacity.

In elongation at break testing, three factors were found to have significant effects (p values $3.19×10^{-5}$, $1.08×10^{-4}$, and $1.73×10^{-6}$, respectively). Breaking elongation rate has been recorded as 97% for neat PVA. In general, increasing fiber loading results in decrease in elongation as seen in Fig 3. This is due to the fact that okra bast fibers show much more brittle nature with lower elongation rates in comparison to PVA. Similarly, Santi et al [32] reported decreased elongation break based on increased cellulose fiber load, Ching et al [23] on increased empty bunch fiber percentage, Ali et al. [24] on higher kenaf fiber content, and Cinelli et al [21] upon addition of corn fibers in PVA composites. The cellulosic fibers restrict mobility of PVA macromolecules as reflected in elongation reduction. Even though alkalized fiber showed nearly twice the elongation of other fibers, this phenomenon cannot be observed in the composite films.
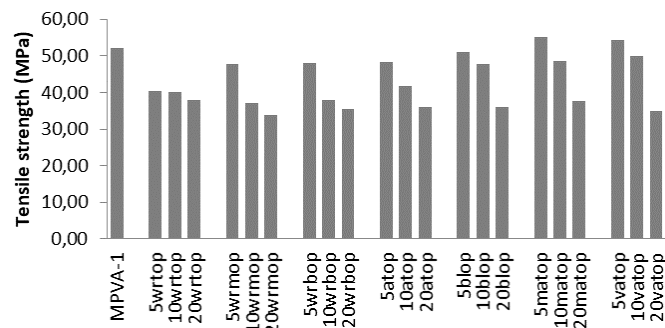
Figure 2. Maximum tensile strength (MPa) values of 100% PVA and the okra bast fiber-reinforced PVA composites
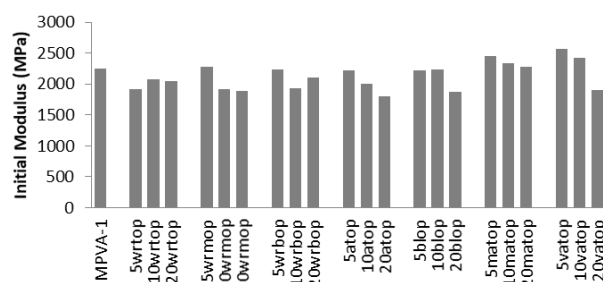
Figure 3. Modulus of elasticity (MPa) of 100% PVA and the okra bast fiber-reinforced PVA composites
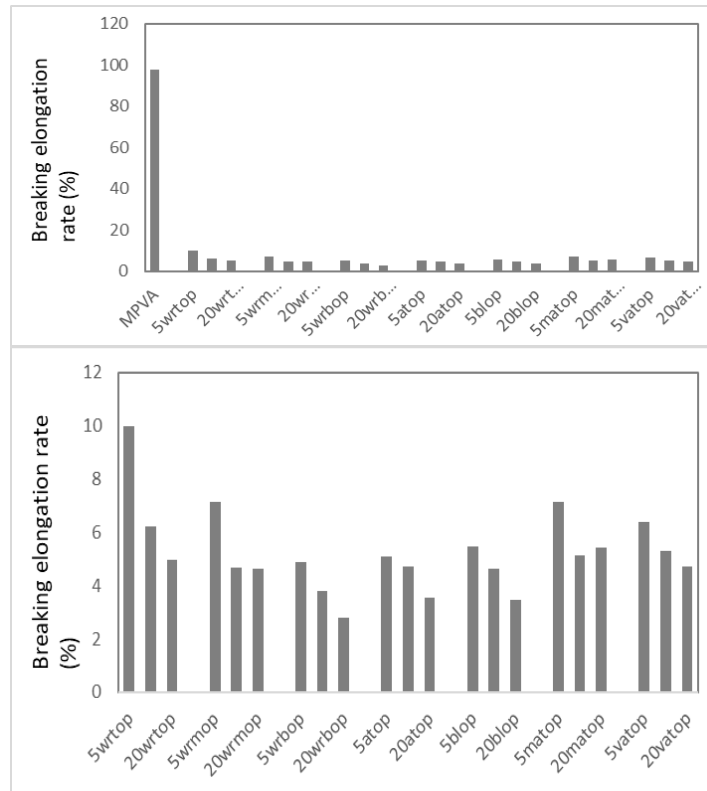
Figure 4. Comparison of elongation at break percentages of (a) 100% PVA and the okra bast fiber-reinforced PVA composites, (b) only the okra bast fiber-reinforced PVA composites (%)

3.3 Water absorption

When water absorption behavior of okra bast fiber-reinforced PVA composites are investigated, it is seen that addition of okra bast fiber systemically reduces water absorption with increased fiber loading (Fig 5). This is due to the fact that water absorption of okra bast fibers are lower than that of PVA. No significant effect of immersion time could be obtained in the test duration range (p value 0.78). Water absorption rate was significantly affected by fiber loading, whereas no significant effect of fiber treatments or plant part of fiber extraction was detected (p values 0.0001-0.002, 0.39-0.58, 0.16-0.29, respectively). Most of the time, water absorption decreases with increase

in fiber loading. This hints water absorption can be controlled via addition of different percentages of fibers. Similarly, Ali et al. [24] also reported decreased moisture uptake with increased kenaf fiber load in PVA composites in humid environment. In the durations the test concluded, no mass loss due to the water solubility of PVA was observed. Cinelli et al. [21] reported 19% water uptake upon 30 minute water soaking. They did not provide data for longer durations. For further research, water absorption of okra bast fiber-reinforced PVA composites can be investigated at shorter and longer durations to monitor water absorption behavior.
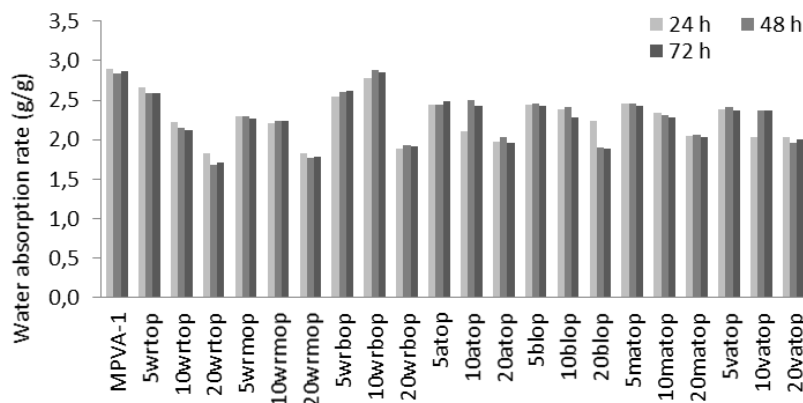
Figure 5. Water absorption rates of 100% PVA and the okra bast fiber-reinforced PVA composites (g/g)

3.4 Biodegradation

Neat PVA and selected composite samples with promising mechanical properties were subjected to biodegradation in soil. A universal effect of okra bast fiber addition on biodegradation of composites as reflected in weight loss and deterioration of tensile properties, has not been detected. When weight loss due to biodegradation is investigated, it is seen that fiber loading has significant effect, whereas fiber treatment does not (p values 0.02, and 0.11, respectively). It is seen that, other than bleached fibers, all okra bast fibers resulted in decrease in weight loss of PVA composites (Fig 6). This result hints that okra bast fibers can be utilized to control PVA degradation. Okra bast fibers may form backbones which maintain integrity of the composite films. Among differently treated fibers, alkalized fiber-reinforced composites show the least weight loss. Alkalization separates extracellulosic materials from the fibers, which may in turn act as diminishing nutrition of biodegrading organisms and slowing weight loss. 14-day soil degradation resulted in 5.00-9.65% weight loss in the studied composites. Imam et al. [22] reported 41-57% weight loss for 120-day soil burial testing which is a much longer duration compared to the current study.

It is seen that biodegradation process has significant effect on tensile strength (Fig 7) and modulus of elasticity (Fig 8) of composites, whereas not on elongation at break (p values 1.82×10^{-6}, 7.25×10^{-17} and 0.80, respectively). On the other hand, soil degradation substantially decreases ductility of neat PVA with a 70% reduction in breaking elongation, while generally increasing elongation of fiber-reinforced composites (Fig 9). Fiber-reinforcement led to increased strength and modulus deterioration, where the effect is dramatic in case of strength loss. The results may be linked to the interaction between PVA and the okra bast fibers. The okra bast fibers may form channels for biodegrading effects to take action. Together with maintaining integrity, the cellulose chains may face scissions which negatively affect mechanical properties. Imam et al. [22] also reported none to negative effect of lignocellulosic fiber loading on PVA composite weight loss upon soil burial. On the other hand, they found positive effect of CO_2 production during soil burial which reflects the rate of biodegradation. Tan et al. [33] proposes that presence of lignocellulosic fibers forms nutrition to PVA-biodegrading microorganisms (reported to be 55 species), hence, accelerating biodegradation process. The findings show that the studied composite films exhibit biodegradable structure. Longer-duration biodegradation tests with measurements at selected intervals may be conducted for future research to obtain better understanding of the biodegradation behavior of okra bast fiber-reinforced PVA composite films.
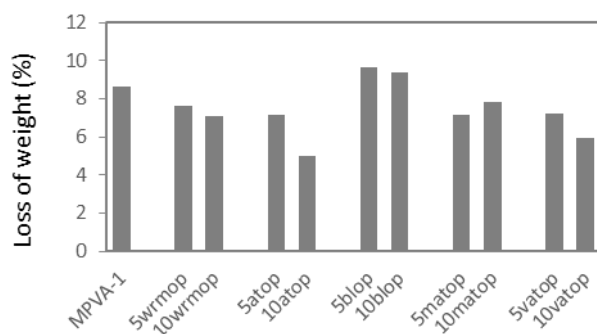
Figure 6. Weight loss of neat PVA polymer and the okra bast fiber-reinforced PVA composites in soil due to biodegradation
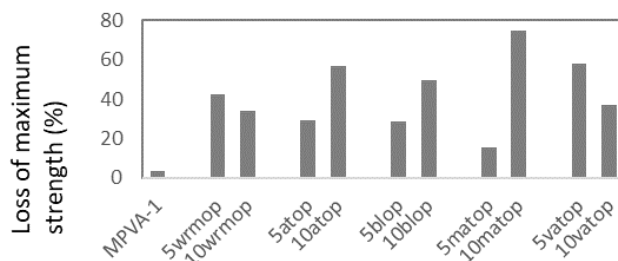

Figure 7. Loss of maximum strength due to biodegradation of neat PVA polymer and the okra bast fiber-reinforced PVA composites in soil (%)
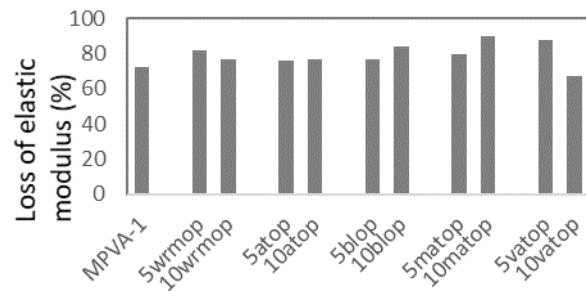
Figure 8. Elasticity modulus loss due to biodegradation of neat PVA polymer and the okra bast fiber-reinforced PVA composites in soil (%)
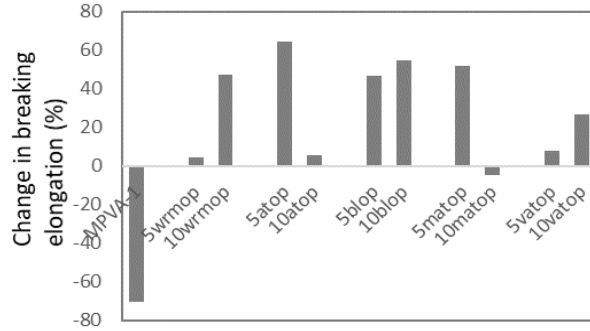

Figure 9. Change in breaking elongation rate due to biodegradation of neat PVA polymer and the okra bast fiber-reinforced PVA composites in soil (%)

3.5 Morphology

In Figure 10, fracture surfaces of okra bast fiber-reinforced PVA composites are presented. In the images, it is seen that fibers tend to lie parallel or perpendicular to the fracture plane. Fiber-rich and fiber-poor regions can be detected. Fiber pull-out observed in fracture surface reflects the potential to increase mechanical properties via improving fiber-matrix interface bonding.
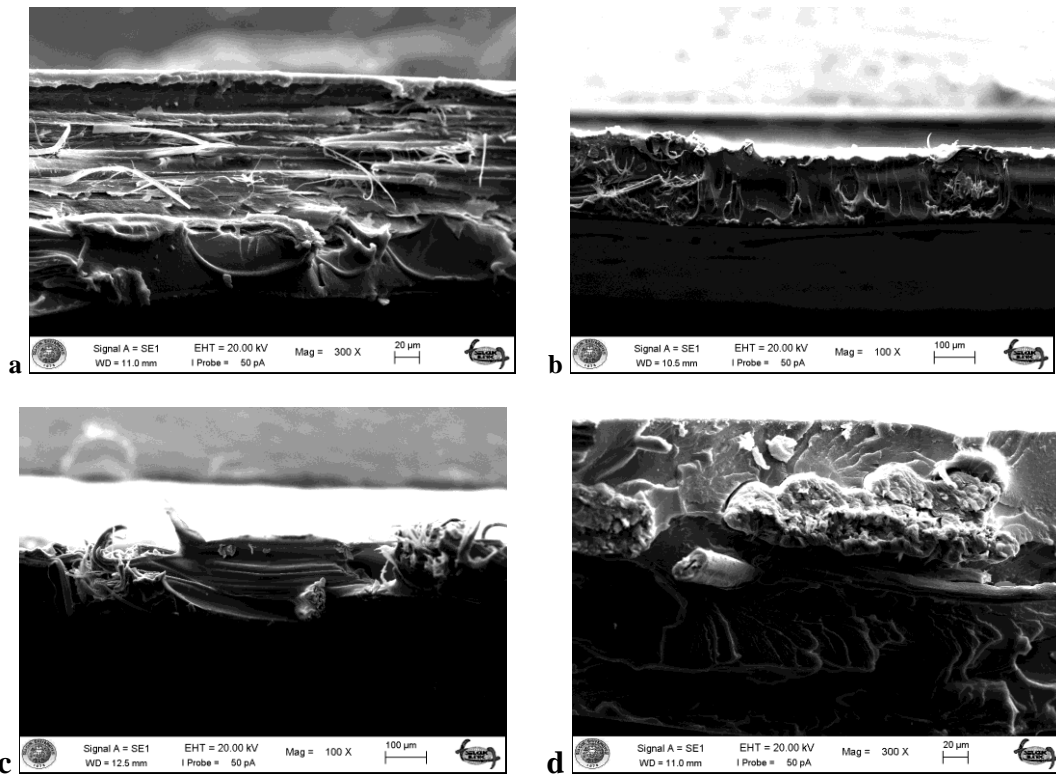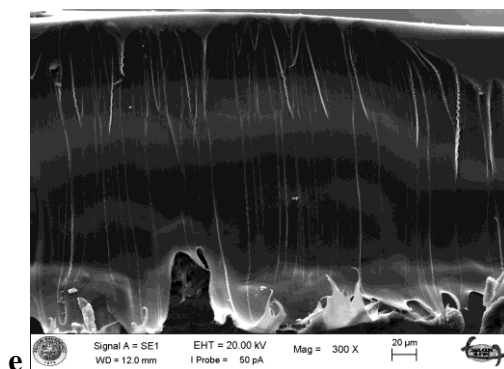
Figure 10. SEM images of (a) 5wrmop, (b) 10wrmop, (c) 20wrmop, d) 5matop, (e) 5vatop

4. CONCLUSION

In this study, poly(vinyl alcohol) (PVA)-based composite films were obtained via solution casting and reinforced with different percentages of okra bast fibers subjected to different chemical treaments. Mechanical, physical and biodegradational properties of the composites were investigated. The tensile strength, elasticity modulus and elongation at break values of obtained composites range between 33.8 - 55.1 MPa, 1.8 - 2.6 GPa, and 2.8-10%, respectively. Chemical treatments led to improved mechanical performance whereas increased fiber content reduces tensile strength, stiffness and elongation, as well as water absorption. Among different treatments, maleic anhydride- and vinyl acetate- treated fiber-reinforced composites reported the highest tensile strength and modulus. Surface chemistry of fibers affect the tensile properties of the composite films more than the tensile properties of the fibers. Okra bast fiber addition significantly affected biodegradation in a complicated way: by decelerating mass loss but accelerating deterioration of mechanical properties. Okra bast fiber-reinforced PVA composite films show biodegradable nature for potential use in packaging and agricultural applications.

REFERENCES

1. Jain N, Singh VK, and Chauhan S. 2007. A review on mechanical and water absorption properties of polyvinyl alcohol based composites/films. *Journal of Mechanical Behavior of Materials* 26(5–6), 213–222, doi: 10.1515/jmbm-2017-0027.

2. Hassan CM, Peppas NA. 2000. Structure and Applications of Poly(vinyl alcohol) Hydrogels Produced by Conventional Crosslinking or by Freezing/Thawing Methods. *Biopolymers · PVA Hydrogels, Anionic Polym. Nanocomposites*, 37–65, doi: 10.1007/3-540-46414-X_2.

3. Cengiz Çallıoğlu F. 2014. The effect of glyoxal cross-linker and NaCl salt addition on the roller electrospinning of poly(vinyl) nanofibers. *Tekstil ve Konfeksiyon* 24(1,) 15–20.

4. Wang L, Periyasami G, Aldalbahi A, Fogliano V. 2021. The antimicrobial activity of silver nanoparticles biocomposite films depends on the silver ions release behaviour. *Food Chemistry* 359(2021), 129859, doi: https://doi.org/10.1016/j.foodchem.2021.129859.

5. Xu S., Jiang M, Lu Q, Gao S, Feng J, Wang X, He X, Chen K, Li Y, Ouyang P. 2020. Properties of Polyvinyl Alcohol Films Composited With Hemicellulose and Nanocellulose Extracted From Artemisia selengensis Straw. *Frontiers in Bioengineering and Biotechnology* 8(August), 1–11, doi: 10.3389/fbioe.2020.00980.

6. Khan GMA, Yilmaz ND, and Yilmaz K. 2022. Effects of Alkalization on Physical and Mechanical Properties of Biologically Degummed Okra Bast and Corn Husk Fibers. *Journal of Natural Fibers* 19(3), 1126–1136, doi: 10.1080/15440478.2020.1798840.

7. Biswas S, Ahsan Q, Cenna A, Hasan M, Hassan A. 2013. Physical and mechanical properties of jute, bamboo and coir natural fiber. *Fibers and Polymers* 14(10), 1762–1767, doi: 10.1007/s12221-013-1762-3.

8. Yilmaz ND, Sulak M, Yilmaz K, Khan GMA. 2017. Effect of chemical treatments on physico-chemical properties of fibers from banana fruit and bunch stems. *Indian Journal of Fibre and Textile Research* 42(1), 111–117.

9. Khan GMA, Yilmaz ND, Yilmaz K. 2020. Effects of chemical treatments and degumming methods on physical and mechanical properties of okra bast and corn husk fibers. *Journal of the Textile Institute* 111(10), 1418–1435, doi: 10.1080/00405000.2019.1702492.

10. Li L, Sheng G, Wang Q. 2015. Parameters optimization for degumming of cotton-straw bast fiber. *Tekstil ve Konfeksiyon* 25(2), 135–139.

11. Alam MS, Khan GMA, Razzaque SMA. 2009. Estimation of Main Constituents of Ananus comosus (Pineapple) Leaf Fiber and Its Photo-Oxidative Degradation. *Journal of Natural Fibers* 6(2), 138–150.

12. Temesgen AG, Eren R, Aykut Y, Süvari F. 2021. Evaluation of Enset fabric reinforced green composite as sound absorber structure. *Tekstil ve Konfeksiyon* 31(2), 73–81, doi: 10.32710/TEKSTILVEKONFEKSIYON.688371.

13. Masudur Rahman ANM, Alimuzzaman S, Khan RA, Hossen J. 2018. Evaluating the performance of gamma irradiated okra fiber reinforced polypropylene (PP) composites: comparative study with jute/PP, *Fashion and Textiles* 5(28), 1-17, doi: 10.1186/s40691-018-0148-y.

14. Potluri R, James Paul K, Abdul Kalam S, Prasanthi P. 2017. Mechanical Properties Characterization of Okra Fiber Based Green Composites & Hybrid Laminates. *Materials Today Proceedings* 4(2), 2893–2902, doi: 10.1016/j.matpr.2017.02.170.

15. Rai S, Hosssain M, Hossain F. 2012. Evaluation of okra [Abelmoscltus esculentus (Moench) L.] as bast fibre crop. *Journal of Crop and Weed* 8(1), 101–104.

16. Khan GMA, Shaheruzzaman M, Rahman MH, Abdur Razzaque, Islam MS, Alam MS. 2009. Surface modification of okra bast fiber and its physico-chemical characteristcs. *Fibers and Polymers* 10(1), 65–70, doi: 10.1007/s12221-009-0065-1.

17. Bledzki AK, Reihmane S, Gassan J. 1996. Properties and modification methods for vegetable fibers for natural fiber composites. *Journal of Applied Polymer Sciencs* 59(8), 1329–1336, doi: 10.1002/(SICI)1097-4628(19960222)59:8<1329::AID-APP17>3.0.CO;2-0.

18. Huda MS, Drzal LT, Mohanty AK, Misra M. 2008. Effect of chemical modifications of the pineapple leaf fiber surfaces on the interfacial and mechanical properties of laminated biocomposites. *Composite Interfaces* 15(2–3), 169–191, doi: 10.1163/156855408783810920.

19. El-Sabbagh A. 2014. Effect of coupling agent on natural fibre in natural fibre/polypropylene composites on mechanical and thermal behaviour. *Composites Part B: Engineering* 57, 126–135, doi: 10.1016/j.compositesb.2013.09.047.

20. Mondal IHM, Khan GMA. 2008. Effect of acrylic monomers grafting onto jute constituents with potassium persulphate initiator catalysed by Fe (II). *Cellulose Chemistry and Technology* 42(1), 9–16.

21. Cinelli P, Chiellini E, Lawton JW, Imam SH. 2006. Properties of Injection Molded Composites Containing Corn Fiber and Poly(Vinyl Alcohol). *Journal of Polymer Research* 13, 107–113, doi: 10.1007/s10965-005-9012-z.

22. Imam SH, Cinelli P, Gordon SH, Chiellini E. 2005. Characterization of Biodegradable Composite Films Prepared from Blends of Poly(Vinyl Alcohol), Cornstarch, and Lignocellulosic Fiber. *Journal of Polymers and the Environment* 13(1), 47–55, doi: 10.1007/s10924-004-1215-6.

23. Ching KS, Ealid M, Ching YC, Haniff M, Khalid M, Beg MTH. 2014. Preparation and characterisation of polyvinyl alcohol/oil palm empty fruit bunch fibre composite. *Materials Research Innovations* 18(sup6), S6-364-S6-367, doi: 10.1179/1432891714Z.0000000001008.

24. Ershad Ali M, Kuan Yong C, Chee Ching Y, Hock Chuah C, Liou N-S. 2015. Effect of Single and Double Stage Chemically Treated Kenaf Fibers on Mechanical Properties of Polyvinyl Alcohol Film. *BioResources* 10(1), 822–838.

25. Parvin A, Alam MS, Gafur MA, Khan GMA. 2022. Synthesis of p-phenylenediamine treated fibrillated cellulose fiber and its application in poly(vinyl alcohol) composites. *Journal of Natural Fibers* 19(16), 14694-14705. Doi: 10.1080/15440478.2022.2068726

26. Laxmeshwar SS, Madhu Kumar DJ, Viveka S, Nagaraja GK. 2012. Preparation and Properties of Biodegradable Film Composites Using Modified Cellulose Fibre-Reinforced with PVA. *ISRN Polymer Science* 2012, 1–8, doi: 10.5402/2012/ 154314.

27. "Polyvinyl alcohol CH2CHOH - PubChem." https://pubchem.ncbi. nlm.nih.gov/compound/Polyvinyl-alcohol#section=Density (accessed Feb. 11, 2022).

28. "Polyvinyl alcohol CAS 9002-89-5 | 114266." https://www. merckmillipore.com/TR/tr/product/Polyvinyl-alcohol, MDA_CHEM-114266 (accessed Feb. 11, 2022).

29. "Polymer Density." http://www.polymerdatabase.com/polymer physics/Polymer Density.html (accessed Feb. 11, 2022).

30. Khan GMA, Yilmaz ND, Yilmaz K. 2017. Okra bast fiber as potential reinforcement element of biocomposites: Can it be the flax of the future?. In VK Thakur, MR Kessler (Ed), Kumar *Handbook of Composites from Renewable Materials vol. 4*., Hoboken, MA, USA: Wiley Scrivener, 379–405.

31. Rahman MM, Afrin S, Haque P. 2014. Characterization of crystalline cellulose of jute reinforced poly (vinyl alcohol) (PVA) biocomposite film for potential biomedical applications. *Progress in Biomaterials* 3(1), 1–9, doi: 10.1007/S40204-014-0023-X.

32. Santi R, Cigada A, Del Curto B, Farè S. 2019. Modulable properties of PVA/cellulose fiber composites," *Journal of Applied Biomateriaşs and Functional Materials* 17(1), 1-7, doi: 10.1177/2280800019831224.

33. Tan BK, Ching YC, Poh SC, Abdullah LC, Gan SN. 2015. A Review of Natural Fiber Reinforced Poly(Vinyl Alcohol) Based Composites: Application and Opportunity. *Polymers* 7(11), 2205-2222, doi: 10.3390/POLYM7111509.

Numerical Calculation of Influencing Parameters on the Seam Allowances of Textile Materials During Ultrasonic Welding

Alexander Reich 0000-0003-4277-4488
Yordan Kyosev 0000-0003-3376-1423

TU Dresden, ITM, Hohe Straße 6, 01127 Dresden, Germany

Corresponding Author: Alexander Reich, Alexander.Reich@tu-dresden.de

ABSTRACT

The ultrasonic welding process allows economically efficient and safe for the workers waterproof joining of textile materials and is applied in the production of various technical textiles, protective clothing, and other types of textile products. In this latest research work, a flexible, textile-based heating element is produced by the connection of waterproof laminated textiles using ultrasonic technique. This novel product allows completely new options for the design of flexible heating and cooling elements for rooms and various other applications but requires high quality seams. This work starts with the theoretical background about the heating of the textile until reaching the welding temperature within the welding zone. The heat flow through the volume of the welded textiles is investigated numerically using Finite Element Method software. The simulation is performed for different sizes and configurations of the seam allowances, so that options between overlapping only in the pressed area without side allowance (no free allowance), small allowance, and larger allowance are simulated. These simulations demonstrate different distributions of the temperature in the seam cross-section at the different configurations, because of the different amounts of textile material around the welding place.

1. INTRODUCTION

In the metal manufacturing and processing industry, software solutions for the simulation of thermal, form-fitting and material-fitting joining processes are in use [1]. In these thermal simulations, heat conduction is represented by means of partial differential equations. The diffusion equations for the homogeneous multidimensional case is:

$$\frac{\partial}{\partial t} u(\vec{x}, t) - a\Delta u(\vec{x}, t) = 0 \tag{1}$$

Dabei gilt: $u(\vec{x}, t)$ Temperature u at time t at the point $\vec{x}$

$a, a > 0$ Thermal conductivity of the material

The initial and boundary conditions for the use of this equation are that the material to be considered has homogeneous properties and distributions. This is usually fulfilled for metallic and armorphous plastics materials.

Such simulation-based tools have so far only been used to a limited extent in the textile and ready-made clothing industry. The reasons for this are the complex micro- and macroscopic structure of textiles and the wide-ranging property profiles of the plastics used [2]. In addition, textiles are generally considered heterogeneous materials, which have direction-dependent properties that require special and more complex calculation operations. Thus, the results already obtained from the metal manufacturing and processing industry cannot be easily transferred to the textile and ready-made clothing industry, which is why the use of these simulation-supported tools has been slow.

1.1 The Ultrasonic Welding Process

By means of the ultrasonic welding process, different materials to be welded can be joined in a compressed and permanent manner with a frequency oscillating between the sonar line and the counterpart in the ultrasonic frequency range and with a suitable static pressure. Ultrasound physically belongs to the mechanical vibrations and is located between the audible sound and the hypersonic. Ultrasonic waves can have frequencies between 10,000 and 100,000,000 Hz with an intensity of $1W/m^2$ to $1x10^{-12}W/m^2$ (see Figure 1).

The oscillation effect of the frequency generator and the sound absorption of the materials convert the oscillation energy into heat. The following illustration shows the mechanical principle of ultrasonic welding. [3]
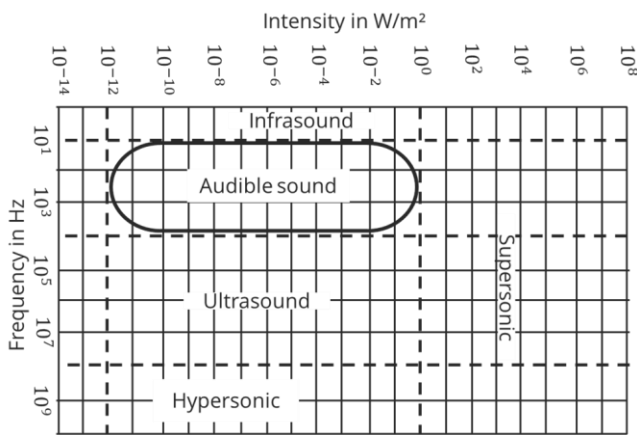
Figure 1. Classification of mechanical vibrations according to intensity and frequency range [3]

The damping constants K (Sono/M1, M1/M2, M2/Anvil) of the material are changed by the contact pressure P of the welding system. According to [4], the damping behavior of polymers is linearly dependent in small and medium stress amplitudes. However, they exhibit a frequency-dependent behavior in this respect [5]. Furthermore, the damping constants K (Sono/M1, M1/M2, M2/Anvil) are additionally modified by the surface properties of the respective materials. In practice, it has proven useful to roughen the corresponding welds during preparation in order to increase the static friction between the material partners. In this mechanical system, the sonotrode delivers constant vibration energy to the system, which is defined as follows (see Eq. (2)):

$$W = \frac{1}{2}m(2\pi fA)^2 \tag{2}$$

Where W the vibration energy of the sonotrode is, m is the mass of the sonotrode, f is the frequenz of the sonotrode and A is the contact area of the sonotrode. Figure 3 shows several possible designs for weld patterns that affect the resulting contact area between the anvil and the weld material. In addition, the arrangement of the textile sheet structures and the welding arrangement used have an influence on the resulting properties of the joining seam (see Figure 4). The resulting contact area, while maintaining identical process parameters, influences the heat transfer as well as the maximum local joining temperature in the welding materials [6]. It was clearly shown [6] that the resulting heat transfers in the weld material show positive and negative influences due to the variation of the resulting contact area, which are directly dependent on the used process parameters.

Figure 2. Mechanical representation of the ultrasonic welding process

The abbreviations in the figure indicate: M1 - the first textile material, M2 - the second textile material, K - damping constant between the involved partners and P - pressure of the welding machine.
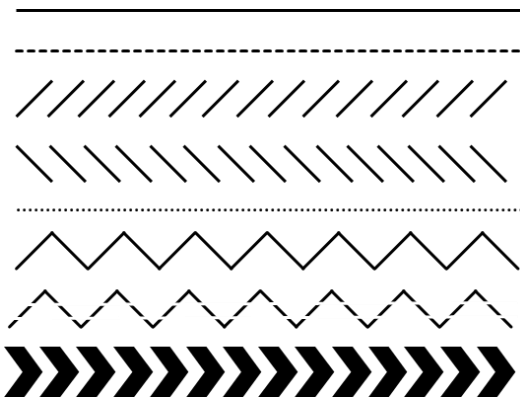
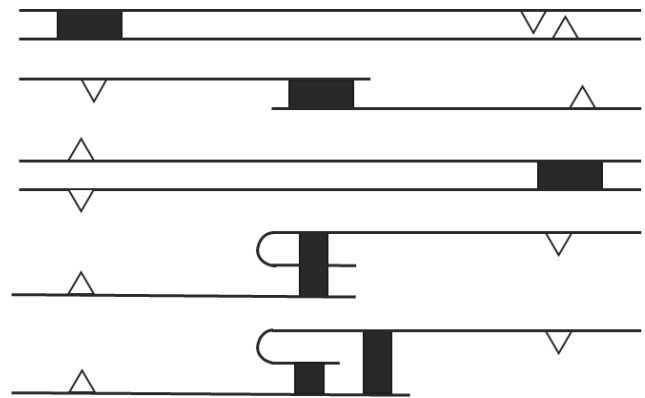**Figure 3.** Ultrasonic welds in different designs [3]

Figure 4. Arrangement of textile fabrics [3]

Ultrasonic welding can be performed both intermittently and continuously. Especially the continuous process is cost efficient and productive and has a wide applicability for technical textiles. Regardless of the process used, a phase change and cross-linking takes place in the joining partners to be cross-linked during ultrasonic joining. These processes are shown schematically in Figure 4.

Based on these thermal-physical interlinking processes, a schematic representation of the welding process can be derived (see the energy-time diagram in figure 5). For comparison, the temperature-distance pairs for continuous ultrasonic welding processes with different energy input (50% to 80%) are shown (see figure 6 with a feed rate of 150 mm/min). It can be clearly seen that the temperature profile is similar.

For the actual manufacturing process, three parameters are of particular importance. These are the applied welding energy (in the form of frequency and amplitude) from the sonotrode, the applied welding pressure, and the dwell time at the joint from the anvil. These three parameters differ for each used textile. Thus, before the actual production of the textile products, extensive, cost-intensive and time-consuming investigations must be undertaken in order to create optimal parameter windows.

1.2 Description of the Mechanical and Thermal Properties

Various textile semi-finished products are available for the use of textiles in technical applications. These can differ in terms of their material, their make-up and their finish. The following table lists the possible options for various selection aspects that can be considered for use in technical applications.
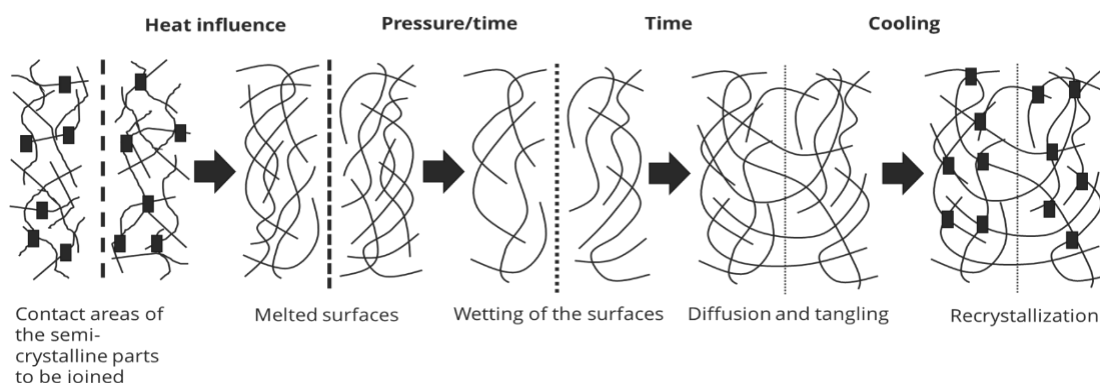
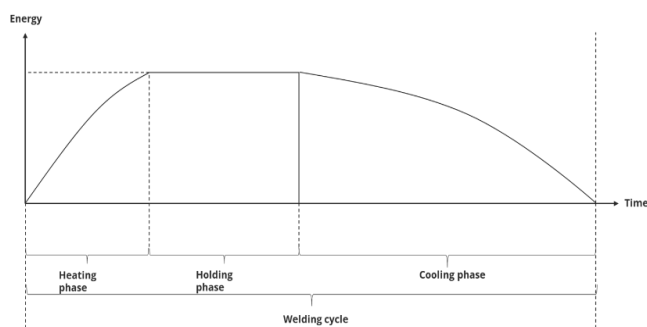**Figure 4.** Melting and cross-linking process in the ultrasonic welding process [7]

Figure 5. Energy/time curve of the ultrasonic welding process [7]
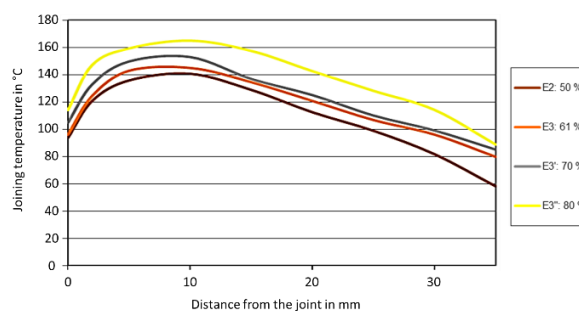

Figure 6. Temperature profile at the seam outlet as a function of the welding energy [6]

Table 1. Selection options for the textile materials [8]

Origin of the textile raw material	Of natural or synthetic origin
Textile classification according to type of plastic	Thermomers, elastomers, duromers
Filament cross-section geometry (selection)	Circular, rectangular, triangular, hollow filament
Textile sheet forming process	Weaving, knitting, braiding, winding, fleece laying
Classification of textile sheet formations (selection)	twill weave, single thread knitted fabric, felt nonwoven fabric
Use of additional coatings	coating on one or both sides
Additional finishing materials (selection)	Dyes, surface finishes, UV stabilisers
Textile running direction used	Warp direction, weft direction, diagonal direction

These different options have a noticeable influence on the usage properties of the textiles and can even give them additional properties such as electrical conductivity or temperature-dependent colour properties. In particular, the used material or combination of materials and the geometric structure of the fibres, filaments and yarns significantly influences the thermal properties of the textiles used later. Figure 1 shows a comparison of different filament cross-sections for the material viscose.

For the numerical consideration of these fibres, the cross-sectional area and the fibre length can be considered constant for the comparability of the thermal properties. Thus, only the fibre geometry would have an influence on the thermal properties. The following table (see table 2) shows the geometry-related shifts of the thermal values for kidney-shaped, star-shaped and hollow fibres in comparison to a round fibre. In addition, the corresponding heat flows and temperature intervals are constant for the calculations.

It is clear from Table 2 that the thermal properties can be greatly changed by specifically varying the fibre and filament geometry. In particular, the use of star-shaped cross-sections leads to a high heat transfer coefficient compared to round cross-sections. In addition, the thermal properties, similar to the mechanical properties, of the textile fibres would have to be split into their x, y and z coordinates, as different internal structures are present due to the manufacturing process of the fibres/filaments. With regard to this influence of the cross-section, the manufacturing parameters in the thermal joining of textiles in particular must be adapted.

2. MATERIAL AND METHOD

2.1 Description of the Material

Various textile semi-finished products are available for the use of textiles in technical applications. These can differ in terms of their material, their make-up and their finish. These different options have a noticeable influence on the usage properties of the textiles and can even give them additional properties such as electrical conductivity or temperature-dependent colour properties. For the numerical calculation of the seam allowance during the ultrasonic welding process, the selection was narrowed down to the following textile (see Table 1). In order to guarantee the media-tight design of the weld seam, a one-sided coating of the backing material is provided.

2.2 Model Development and Mesh Creation

For the numerical calculation of the heat propagation in the SolidWorks software, two corresponding model are generated for the investigation. The models are arranged in such a way that they resemble a lap seam or a flat seam. For the actual simulations, the initial models are created with four different seam widths to show the thermal influence of the transfer seam widths on the heat propagation during the ultrasonic welding process. The initial models "lap seam" and "flat seam" for the numerical calculation are shown in figure 8 and 9.
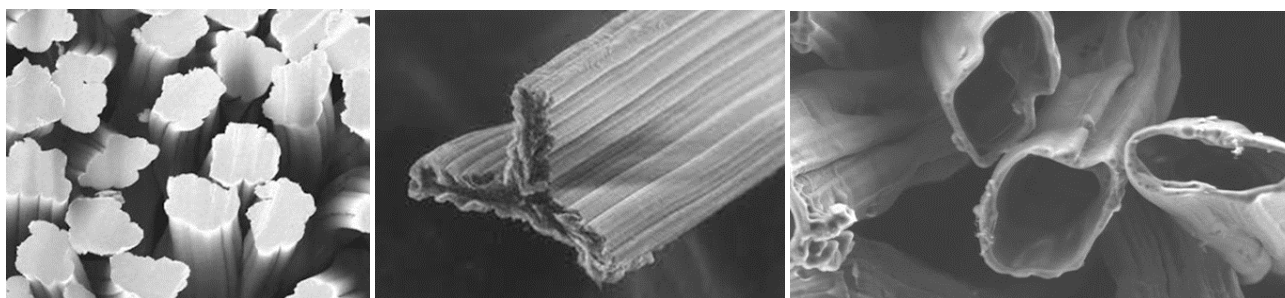

Figure 7. Viscose in kidney-shaped form (left) [9]; in star-shaped form (centre) [10] and as void fibre (right) [11]

Table 2. Comparative thermal quantities for different fibre geometries

	Sheath area in mm²	Heat capacity in %	Heat transfer coefficient in %
Round-shaped	6.33	100	100
Kidney-shaped	6.77	100	107
Star-shaped	65.32	100	1032
Hollow fibre	27.04	77	427

Table 3. Description of the construction of the textile material used

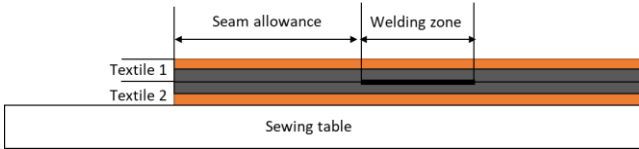|	Description
Base material	Polyamide 6.6 (PA)
Coating material	Thermoplastic Polyurethane (TPU)
Thickness	0.2 mm (base material), 0.2 mm (coating material)

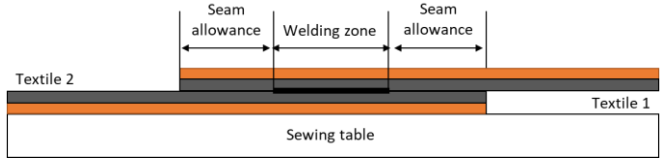**Figure 8.** Model arrangement "Lap seam" for the numerical calculation

Figure 9. Model arrangement "Flat seam" for the numerical calculation

The welding zone has a width of 3 mm in the numerical calculation, which is positioned centrally between textile 1 and textile 2. The total height of textile 1 and 2 is 0.4 mm. The weld width is set to 0 mm, 1 mm, 2 mm and 5 mm in the numerical calculation to investigate the heat propagation to the textile edge. Furthermore, the various components have been given thermal material parameters for the numerical calculation. These are presented in Table 4.

It should be mentioned that the thermal parameters shown in Table 4 refer to conventional plastics and not to partially stretched textile fibre materials. Due to the different production methods, the thermal and mechanical parameters of the textiles may differ, which is why this must be taken into account in the final considerations. Furthermore, it is assumed for the numerical calculations that the various plastic-based textile fibre materials are homogeneous materials with identical characteristics in the x, y and z directions. This assumption must be made at the

moment, as the differences due to production and geometry cannot yet be completely transferred into the simulation.

For the generation of the numerical mesh, as a basic requirement for the thermal calculations, the SolidWorks software provides various solvers. These solvers use various mathematical algorithms to transfer the created components into a suitable mesh. The three solvers provided by the software are shown below in Table 5 with their areas of application.

For a suitable selection of the necessary solver, it must first be examined how detailed the necessary simulation network for the thermal calculations must be for the representation. The resulting meshes for different element sizes (from 0.1 mm to 0.05 mm) are given below in Figure 10. It can be seen that as the element size decreases, the number of nodes in the mesh increases dramatically, which increases the accuracy of the simulation as well as the calculation time.

Table 4. Thermal properties of the used materials [12]

	Thermal conductivity in W/(mK)	Specific thermal capacity in J/(kgK)
Table material (Epoxy resin)	0,188	1100
Textil 1/2: base material (PA)	0,233	1601
Textil 1/2: base material (PE)	0,461	1796
Textil 1/2: Coating material (TPU)	0,2618	1900
Textil 1/2: Coating material (PVC)	0,147	1355

Table 5. Properties of the different SolidWorks solvers [12]

Direct Sparse Solver	FFEPlus	Intel Direct Sparse
Suited for multi-area contact problems	Suited for solving problems with more 100.000 dots	Suited for solving problems with less than 25.000 dots
Suited for multi-material problems		
Needs the most RAM of the computer		

Mesh size: max. 1 mm
       min. 0,05 mm
Total node: 1649
Total elements: 760

Mesh size: max. 0,5 mm
       min. 0,025 mm
Total node: 5689
Total elements: 2720

Mesh size: max. 0,1 mm
       min. 0,005 mm
Total node: 21064
Total elements: 10282

Mesh size: max. 0,05 mm
       min. 0,0025 mm
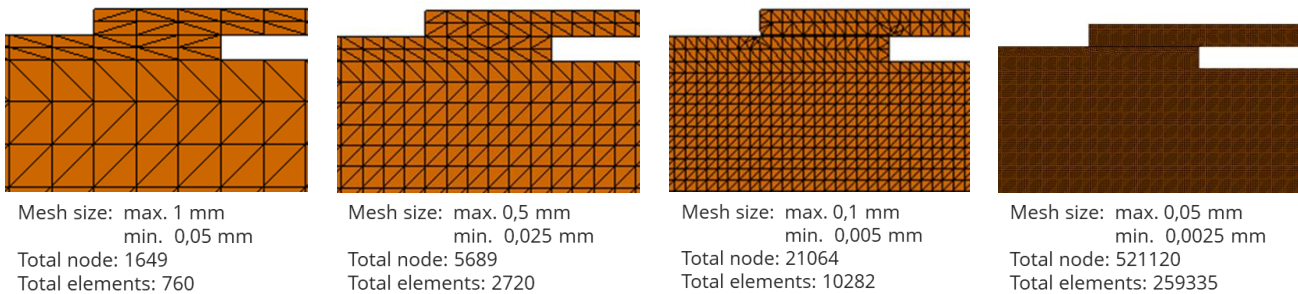Total node: 521120
Total elements: 259335

Figure 10. Diffrent mesh sizes for the thermal calculation

For the final selection of the element sizes for the mesh, the individual CAD elements must be considered more closely. In particular, the joint seam, which serves as the heat source in the calculation, as well as the transitions between the carrier and coating materials were examined more closely. It was found that up to an element size of 0.1 mm, the zones under consideration can only be insufficiently represented. Therefore, an element size of maximum 0.05 mm was chosen for the mesh generation. Figure 11 shows the generated mesh around the joining zone for the element size.
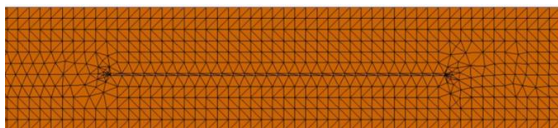
Figure 11. Detailed view of the meshed welding zone

Furthermore, in the numerical model, thermal propagation takes place over different geometries along the cross-section. In addition, for the investigation of coated textiles it is necessary to use different material parameters for the calculation. Therefore, the choice of the solver was made for the "Direct Sparse Solver" to represent the thermal propagation.

After creating the numerical mesh, the corresponding heat sources and transitions must be implemented in the model. For the positioning of the thermal energy source, it is assumed that it is located between the two textiles and has a constant temperature of 130 °C (403.15 K) with a width of 3 mm. This is a simplified assumption for the numerical calculation, as the conversion of mechanical energy (vibration energy of the horn) into thermal energy depends on the textile material and the vibrations used. This complex, non-linear process cannot be calculated numerically at this time. Figures 11 and 12 show the initial temperatures for the plastic layers (substrate and coating material) and the heat source in the centre of the joining zone.
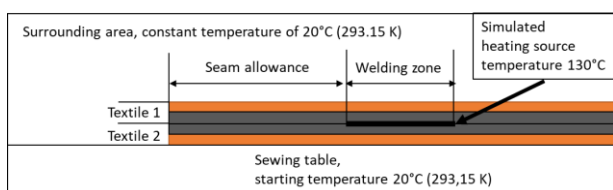
Furthermore, forced convections have been implemented in the models to represent the heat transfer to the environment. These additional heat transfers are shown in figures 13 and 14 for the models.

With these conditions and configurations, this numerical analysis is performed and the static equilibrium of the temperature distribution is determined. For the current numerical calculation, only the middle plane of the weld is calculated. The 3D effects of the rounding are not yet considered.

2.3 Simulation

Using the previously defined mesh models and the corresponding initial conditions, various numerical calculations can be carried out. These are presented in this publication:

- Variation of the seam width on the heat propagation behaviour for cut-off and flat seams.
- Variation of material pairings using the example of polyester with a PVC coating as a cut seam and flat seam (seam width 0 mm and 5 mm for lap and flat seam)
- Variation of the joining temperature between 100°C, 120°C, 140°C and 160°C as a cut seam with the material combination nylon with a TPU coating (seam width 2 mm for lap seam)

The results of the first numerical calculations are shown in the figures below.

The two different simulations in Figures 14 and 15 show that for seam distances less than 5 mm, the heated and melted area is too close to the ultrasonic joining seam. If the distance to the ultrasonic joining seam is greater than 5 mm, the plastic layers remain in their solid phase and do not melt as a result of the joining process.

Figure 11. Thermal sources for numerical calculation in the model "lap seam"
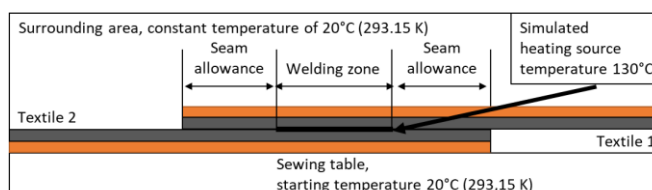

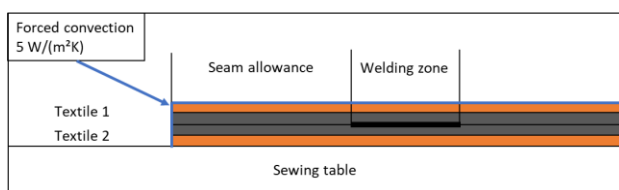**Figure 12.** Thermal sources for numerical calculation in the model "flat seam"

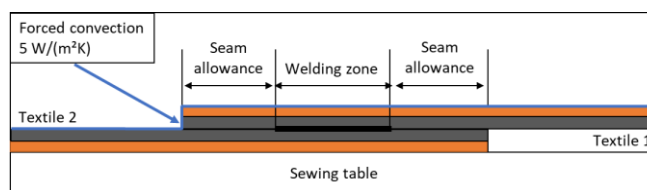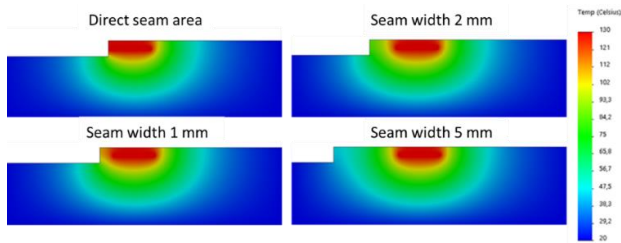**Figure 13.** Thermal sources for numerical calculation around the model "lap seam"

Figure 14. Thermal sources for numerical calculation around the model "flat seam"

Figure 14. Thermal influence of the transfer width on the cooling behaviour of the textile plastic (stationary heat propagation; ambient temperature 20°, material combination TPU/PA-textile with solid substrate) for the model "lap seam".
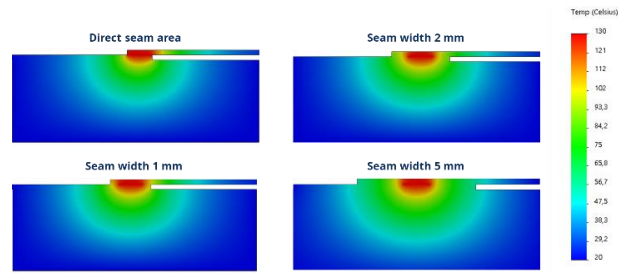

Figure 15. Thermal influence of the transfer width on the cooling behaviour of the textile plastic (stationary heat propagation; ambient temperature 20°, material combination TPU/PA-textile with solid substrate) for the model "flat seam".

Practical experience has shown that with shorter seam allowances, the immediate boundary area to the joint melts in an uncontrolled manner and shrinks or is deformed by the additional mechanical loads, thus impairing the seam strength and quality. Figure 16 shows an infrared image of a continuous ultrasonic welding process with a seam spacing of 1 mm. In it, clear temperature differences are visible in the joining zone, which are caused by different cooling zones.

Figure 17 shows the thickness-temperature diagram for a continuous ultrasonic welding process. The different temperature curves are given for different energy intesities. It shows that there is a temperature maximum in the middle range (at 0.4 mm, which represents the joining range of the joining partners involved), which cools down accordingly towards the top and bottom of the joining partners. With a few exceptions, in particular the thickness of the assumed

joining zone in the simulation, the tendens show similarities to reality with the initial numerical calculations.

Figure 18 below shows the numerical calculations for an alternative material combination for the "lap seam" and "flat seam" simulation models. The base fabric was replaced by polyester and the coating material by polyvinyl chloride. The polyester used has a higher thermal conductivity and thermal capacity than the polyamide, whereas the polyvinyl chloride used has a lower thermal conductivity and thermal capacity than the thermoplastic polyurethane (see Table 4). For the temperature propagation in and around the joining zone, this means that the thermal energy is passed on more strongly through the polyester. In practice, there would be a presumption that the joined sheet structures cool down faster than the joined sheet structures made of PA/TPU, which requires a change in the manufacturing parameters.
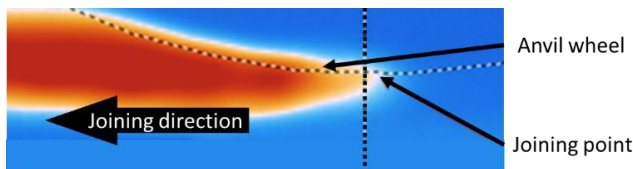

Figure 16. Infrared image of a continuous ultrasonic welding process with a seam spacing of 1 mm [6]
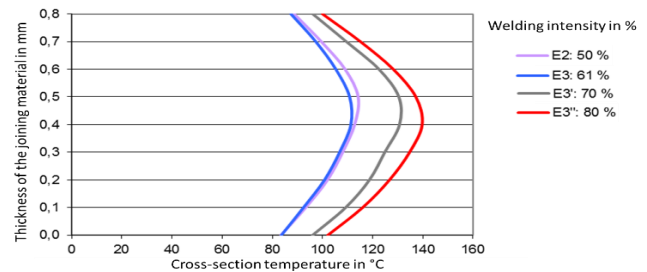

Figure 17. Temperature-thickness diagram for different single-energy intensities in the ultrasonic joining process [6]
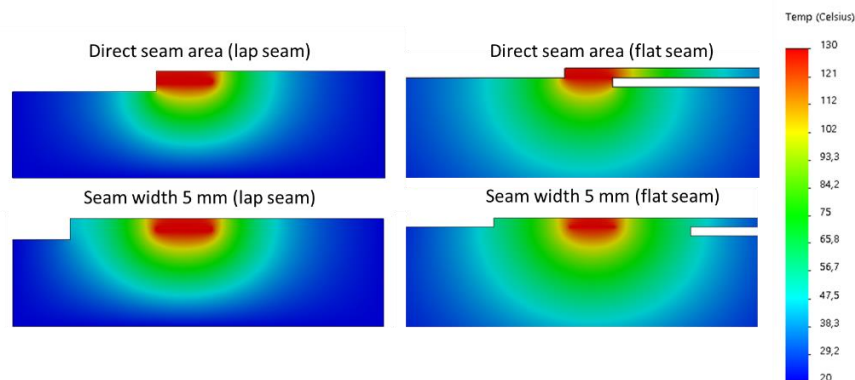

Figure 18. Different numerical calculations for the thermal influence of the material parameters thermal conductivity and heat capacity for the model "Lap seam" and "flat seam" for a seam allowance of 0 mm and 5 mm

The final numerical calculation serves to determine the influence of the joining temperature in the melting zone. For this purpose, the "lap seam" model with a seam spacing of 2 mm was selected and considered with different temperatures. The results of these numerical calculations are shown in Figure 19.

Figure 19 clearly shows that the increase in temperature significantly increases the cooling down area. In practice, this would mean that the seam allowance must also be increased to prevent damage to the joint. It also shows that at high joining temperatures, additional methods must be used to prevent the substrate from heating up.

4. CONCLUSION

By means of numerical calculation of the heat propagation during ultrasonic welding, information can be collected and processes can be represented in order to better understand the processes in the joining zone. This creates new options that can be used to increase process reliability and weld seam reproducibility for industry. However, the numerical calculation of textile ultrasonic welds is very challenging. In contrast to metals and other homogeneous materials, the textile material is a multidimensional hetrogenic material which can be strongly changed by environmental influences. Furthermore, the energy transformation processes between mechanical vibration energy and thermal energy are still not fully understood by science.

The numerical calculations carried out showed that a seam allowance of at least 5 mm is required for the selected material combination. By maintaining this minimum distance during ultrasonic welding, it is possible to keep the interface of the welded materials at room temperature and thus achieve a uniform design of the weld area. A smaller seam allowance will cause the interface to melt and the material to escape from the weld, which will significantly reduce the seam strength. This process cannot be reproduced with the current numerical calculation. For the representation of such processes, the existing numerical models must be executed as transient calculations.

The investigations in this article are a first step in the simulation-based investigation of ultrasonic textile welding. For further work and for a better understanding of the ultrasonic process, the existing model will be converted into a transient model.
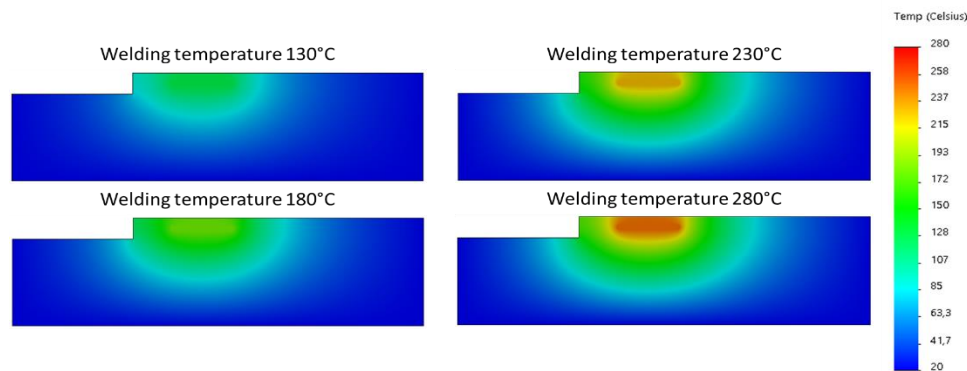

Figure 19. Numerical calculations on the influence of the joining temperature thermal conductivity and heat capacity for the "lap seam" models for a seam allowance of 2 mm and the initial temperatures of 130°C, 180°C, 230°C and 280°C

REFERENCES

1. Zein El Dine S. 2008. *Ermüdungssicherheit der Schweißnähte an Ringflanschverbindungen in turmartigen Stahlbauten*. Cuvillier Verlag.

2. Wheeler A. 2013. Modeling and Analysis of a Heat Transport Transient Test Facility for Space Nuclear Systems. Department of Nuclear Engineering and Radiation Health Physics, Oregon State University.

3. Endre N, Ferenc T. 1979. *Ruhaipari kezeköny: 6. Hegesztés*. Budapest.

4. Ottl D. 1981. *Schwingungen mechanischer Systeme mit Strukturdämpfung. Düsseldorf*, VDI-Verlag 1981 (VDI-Forschungsheft Nr. 603).

5. Ahrens R, Ottl D. 2000. Modalanalyse trotz frequenzabhängiger Steifigkeiten und Dämpfungen? In VDI-Wissensforum (Hrsg.): Experimentelle und rechnerische Modalanalyse sowie Identifikation dynamischer Systeme, VDI Schwingungstagung. Kassel, Germany.

6. Rödel H, Hund R-D. 2015. *Experimentelle Evaluierung der Mikroprozesse beim Textilschweißen am Beispiel des Ultraschallschweißens und Ableitung von Maßnahmen zur gezielten Einstellung der Schweißnahteigenschaften (IGF-BR 17762)*. Dresden: ITM

7. Yordan K, Reich A. 2021. October. Numerical optimization of the seam allowances during ultrasonic welding of textile materials. XV International Izmir Textile and Apparel Symposium. Izmir, Turkey.

8. Bobeth W, Berger W. 1993. *Textile Faserstoffe: Beschaffenheit und Eigenschaften*. Berlin: Springer.

9. Kelheim Fibres Gmbh. 2021. 09, 06. Viskosefaser DANUFIL® Langstapel. Retrieved from http://kelheim-fibres.com/viskosefaser/danufil-langstapel.

10. Wallfisch B, Schmidtbauer J. 2021. 09, 06. Maßgeschneiderte saugfähige Viskosefasern für Hygieneanwendungen (17. Hofer Vliesstofftage). Retrieved from https://www.hofer-vliesstofftage.de/vortraege/2002/2002-01.pdf.

11. Kelheim Fibres Gmbh. 2021. 09, 06. Viskosefaser Bramante. Retrieved from kelheim-fibres.com/viskosefaser/bramante/.

12. Solidworks. 2021. 09, 06. Analyse-Solver. Retrieved from help.solidworks.com/2019/german/solidworks/cworks/c_analysis_solvers.ht

A Hydrophilic/Hydrophobic Composite Structure for Water Harvesting from the Air

Güldemet Başal[1*] 0000-0003-4622-802X
Nur Oral[2] 0000-0002-7717-6122

[1] Ege University, Department of Textile Engineering, Bornova, İzmir, Türkiye
[2] Ege University, Department of Biotechnology, Bornova, İzmir, Türkiye

Corresponding Author: Güldemet Başal, guldemet.basal@ege.edu.tr

ABSTRACT

The freshwater shortage is one of the world's most pressing challenges needs to be addressed rapidly. To overcome this challenge, harvesting water from the air has emerged as a simple and cost-effective approach. Traditional wire meshes have been already used for atmospheric water harvesting from the fog. In foggy areas, the wire meshes are placed perpendicular to wind and water droplets in fog carried by the wind are trapped and deposited on the surface of meshes. The purpose of this study is to improve the water harvesting capacity of the traditional wire mesh by modifying its surface using a nature-inspired composite structure consisting of hydrophilic and hydrophobic zones. Hydrophilic zones were obtained by electrospinning or electrospraying of the polyamide 6 (PA6) / chitosan (CH) blend, and hydrophobic zones were attained by electrospraying of polycaprolactone (PCL). The water harvesting capacity of the resulting meshes was tested and compared with each other. The highest water harvesting capacity was achieved with the PA6/CH nanofiber coated wire mesh as 87 mg / cm2/h. This mesh collected twice as much water compared to the uncoated mesh. However, its water collection rate decreased when nanofiber surface reached the saturation level. The addition of hydrophobic PCL particles onto PA6/CH nanofibers significantly reduced the amount of water captured. When both PA6/CH and PCL were electrosprayed on the wire mesh in particle form water harvesting capacity slightly increased, but it was still poor compared to uncoated mesh.

1. INTRODUCTION

In today's world, clean drinking water scarcity is one of the major problems that need to be addressed urgently. It is estimated that nearly 52% of the world's population will live in water-stressed regions by 2050. Unfortunately, only about 2.5% of the water on earth is drinkable, and this rate is decreasing day by day due to increasing environmental pollution and climate change [1,2]. Treatment of wastewater for clean drinking water or obtaining freshwater from seawater are some suggested solutions to reduce the gap between the water supply and demand, but wastewater treatment and desalination of seawater are quite costly with today's technology [3]. This has led people to look for unconventional water resources.

Fog is one of the unconventional water sources, and fog harvesting, which is an ancient practice, is a simple, sustainable, and cheap method to collect water from the air. Fog harvesters are generally made from mesh nets. Water droplets are collected as fog passes through the holes of the mesh by the wind. Although meshes have been the most widely used material for fog harvesting, they have low water collection efficiency [4]. To overcome this limitation, the surface of the mesh can be modified. In recent years, with the development of new and advanced materials, mimicking nature has become very popular. The Namib desert beetle shown in Figure 1 is an insect that lives in an extremely arid desert [5]. This insect uses water vapor in the air to meet its water needs by converting it into liquid form. Due to this feature, it has caught many researchers'

To cite this article: Başal Bayraktar G, Oral N. 2022. A hydrophilic/hydrophobic composite structure for water harvesting from the air. *Tekstil ve Konfeksiyon*, 32(4), 384-389.

attention. Parker et al. [6] found that the Namib desert beetle harvests water from thin air through hydrophilic and hydrophobic regions on its back. Several other studies have also revealed that the hydrophilic/hydrophobic structures can be used to capture and condense water from the air [7-10]. Zhai et al. developed a surface consisting of hydrophilic patterns on a superhydrophobic surface to mimic the wing surface of the Namib Desert beetle for water harvesting [7]. Huang et al. produced bio-inspired water harvesters using the electrospinning method. They used polyvinylidene fluoride (PVDF) and expanded graphite (EG) to create bead-on-string nanofibers which are inspired by spider silk [8]. They also fabricated bicomponent nanofibers from polyvinylidene fluoride (PVDF) and polyacrylonitrile (PAN) which are inspired by the Namib Desert beetle [9]. While PVDF provided hydrophobicity PAN and EG created hydrophilic segments of the nanofibrous material. Garrod et al. fabricated hydrophilic-hydrophobic patterned surfaces using pulsed plasma deposition of a hydrophilic polymer array on a superhydrophobic background [10]. The main role of the hydrophilic surfaces in water harvesters is that hydrophilic surfaces promote the nucleation of water droplets since hydrophilic materials attract water molecules in the air. On the other hand, hydrophobic or superhydrophobic surfaces are preferred in water harvesters since water droplets are able to slide over these surfaces, which makes their removal easy[11,12].

Figure 1. Namib desert beetle [5]

Wire mesh has been used traditionally for water harvesting. Ghosh et al. used stainless steel wire meshes inside the cooling tower to harvest water from the rising fog stream. They found that the water harvesting efficiency of meshes was mainly affected by the shade coefficient of the mesh, effective dripping length of water droplets along the mesh, and the inclination angle of the mesh regarding the vertically rising fog stream [13]. Knapczyk-Korczak et al. used a raschel mesh coated with electrospun polyamide 6 nanofibers to condense water from the fog. It was reported that the coated mesh had a water harvesting capacity of three times higher than the uncoated one [14].

In this study in order to improve the water harvesting capacity of the traditional wire mesh hydrophilic and hydrophobic zones were created on the mesh surface. To obtain hydrophilic zones polyamide 6 and chitosan were chosen. Polyamide 6 is a hydrophilic polymer with good mechanical properties [15]. Chitosan is widely used in many areas due to its antimicrobial properties [16]. Polyamide 6 and chitosan are either electrospun or electrosprayed to form nanofibers or nano or micro size particles. To obtain a hydrophobic zone on the surface, PCL, which is a hydrophobic polymer, was preferred [17]. It was electrosprayed in the form of nano or microparticles. Instead of polymer coating, nano size fibers or particles were preferred in this study since they have the advantage of providing a large surface area for catching small water droplets.

2. MATERIAL AND METHOD

2.1 Material

Polyamide 6, chitosan (medium molecular weight), and polycaprolactone (average Mn 80,000) were used as polymers. Acetic acid (100%), formic acid (98–100%), and dimethylformamide were used as solvents. All chemicals and solvents were purchased from Sigma Aldrich. Single-layer woven stainless steel wire mesh with a mesh count of **3.5 (openings/cm)** and a wire diameter of 1 mm was purchased from the local market.

2.2 Method

Three different surfaces were created for water harvesting experiments, and the untreated wire mesh was used as control. To produce hydrophilic zones nanofibers were produced from the hydrophilic polyamide 6 (PA6) and chitosan (CH) blend by the electrospinning method. Also, nano/micro-sized hydrophilic particles were produced from the same polymer blend using the electrospraying method. In order to obtain hydrophobic zones, polycaprolactone (PCL), which is a hydrophobic polymer, was electrosprayed onto either wire mesh or nanofiber coated wire mesh. Both electrospinning and electrospraying methods utilize the electrical field to produce nano-sized fibers or particles. Electrospinning/electrospraying processes were carried out using a high voltage power supply (ISEG), a syringe pump (NE-300, New Era Pump Systems), and an aluminum foil-coated copper plate as the collecting surface. A 5 mL plastic syringe and a 0.8 mm (21 Gauge) internal diameter needle were used in all studies.

First, optimal solution and process parameters were determined for electrospinning and electrospraying to attain uniform bead-free nanofibers and uniform spherical nano or micro size particles. For electrospinning of hydrophilic nanofibers, PA6 / chitosan blend solutions with a concentration of 13.5% (w/v) were prepared by dissolving PA6 and chitosan polymers at a weight ratio of 8:1 (w/w) together in a formic acid/ acetic acid solvent mixture in the ratio of 3:2 (v/v), respectively. The distance between the needle tip to the collector was set to 10 cm and

electrospinning was performed at a flow rate of 0.2 mL/h and applied voltage of 17 kV. To obtain hydrophilic particles, PA6 / chitosan blend solutions with a concentration of 6% (w/v) were prepared using the same polymer blend ratio and solvent mixture. The distance between the needle tip to the collector was set to 10 cm and electrospraying was performed at a flow rate of 0.6 mL/h and applied voltage of 22 kV. For electrospraying of hydrophobic particles, a PCL solution with a concentration of 8% (w/v) was prepared by dissolving PCL in dimethylformamide (DMF), and it was electrosprayed at a flow rate of 0.6 mL/h. The applied voltage was 10 kV, and the distance from the needle tip to the collector was 20 cm. After the determination of process and solution parameters, wire meshes were coated for water harvesting experiments. For this purpose, PA6/CH nanofibers were directly electrospun on a wire mesh (Sample 2), PCL particles were electrosprayed on the PA6/CH nanofibers coated wire mesh (Sample 3) and also both PCL and PA6/CH were electrosprayed on a wire mesh (Sample 4). Table 1 summarizes the wire meshes used in water harvesting experiments. The main purpose was to create hydrophilic and hydrophobic zones on wire mesh. Hydrophilic zones were formed either by PA6/CH nanofibers or PA6/CH nanoparticles. Hydrophobic zones were produced by PCL nanoparticles.

Table 1. Wire meshes used in water harvesting experiments

Code	Sample Content
Sample 1	Uncoated wire mesh
Sample 2	Wire mesh coated with electrospun PA6/CH nanofibers
Sample 3	Wire mesh coated with electrospun PA6/CH nanofibers and electrosprayed PCL particles
Sample 4	Wire mesh coated with electrosprayed PCL and PA6/CH particles

The water harvesting capacity of coated wire meshes was measured using the experimental setup shown in Figure 2. Mesh samples were cut into rectangular pieces of 10 cm x 17 cm. A conventional ultrasonic cool mist humidifier was used to create fog. The test sample was placed at a distance of 5 cm from the outlet of the humidifier. A beaker was placed under the sample to collect condensed water. Ambient conditions were kept constant at 25 πC and 40 % RH for each trial. Coldwater mist was sent on the samples for a total of 3 hours. At the end of each hour, the water collected in the beaker was weighed.

3. RESULTS AND DISCUSSION

3.1 Characterization

The optimal solution and process parameters were determined for electrospinning and electrospraying prior to coating of wire meshes. Figure 3 (a) and (b) show the scanning electron microscope (SEM) images of PA6/CH nanofibers and particles obtained during optimization study, respectively. No bead formation was detected in the fiber structure. PA6/CH particles consisted of smooth spherical ones and irregular granular ones. PCL was successfully sprayed in spherical form (Figure 3c). Average fiber and particle diameters were determined as 101 nm ± 24, 515 nm ± 376 for PA6/CH, and 2.5 μm ± 0.525 for PCL, respectively. Figure 3 (d) shows the scanning electron microscope (SEM) image of the PCL sprayed onto PA6/CH nanofibers. In this case, it was observed that some PCL particles were not in the expected smooth spherical form.

Wire meshes were modified by coating them with hydrophilic and hydrophobic polymers for water harvesting from the fog. Figure 4 (a) shows the wire mesh coated with PA6/CH nanofibers and PCL particles, respectively. Nanofibers covered the holes of the mesh and the wire mesh looked like it was covered by a film. Figure 4 (b) illustrates the wire mesh coated with both PCL and PA6/CH particles. In this case, a white coating covered the wires. The holes were open.

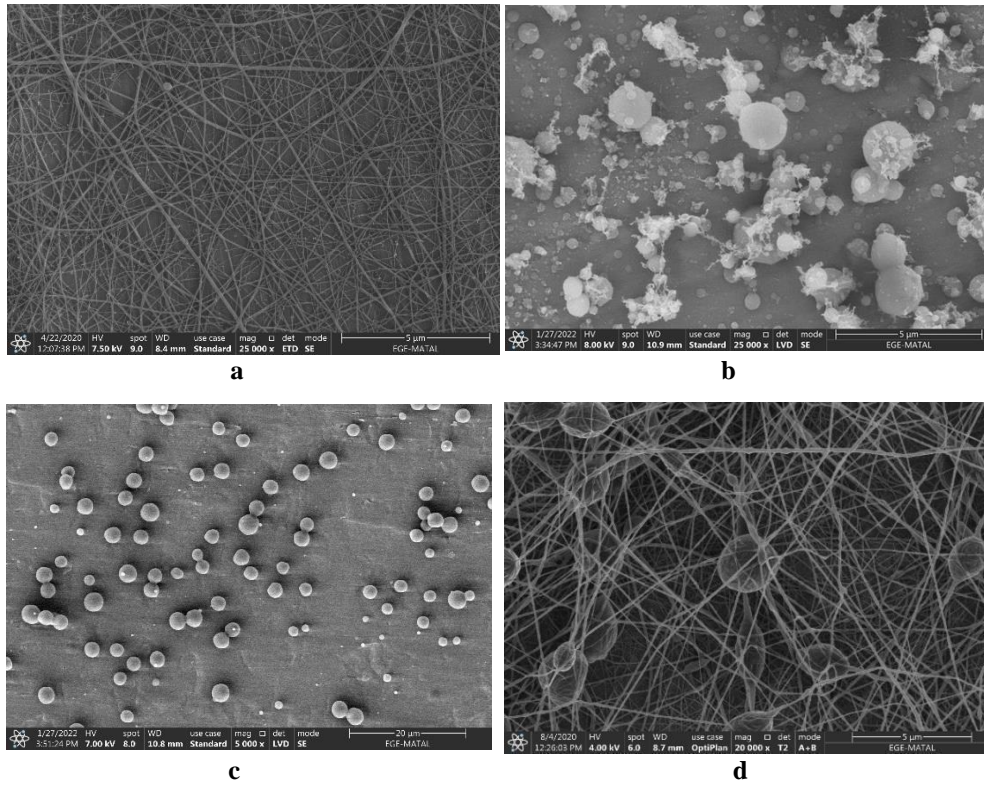**Figure 2.** Experimental setup for water harvesting capacity test

Figure 3. SEM images of **(a)** PA6/CH nanofibers **(b)** PA6/CH particles **(c)** PCL particles **(d)** PCL sprayed onto PA6/CH nanofibers
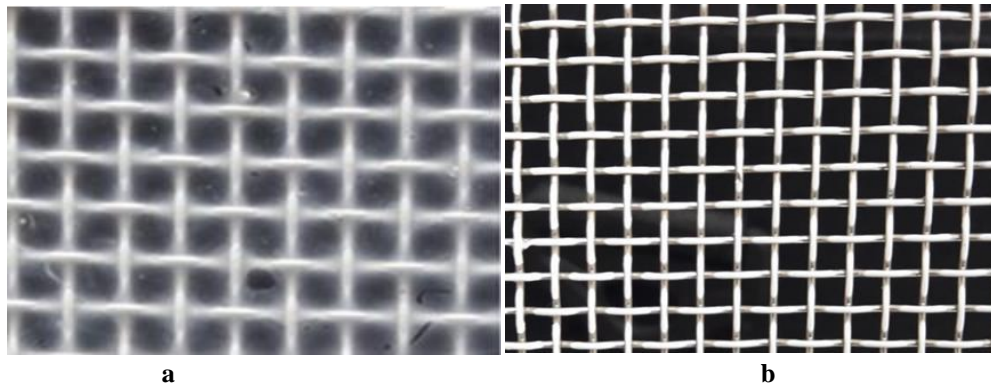

Figure 4. Coated wire mesh (**a**) Sample 3 (**b**) Sample 4

3.2 Water harvesting from wire mesh

Figure 5 shows the water harvesting from the fog with a coated mesh. As fog passed through the wire mesh, water droplets formed on the surface. Figure 6 illustrates mesh samples during water harvesting experiments. It was clearly seen that the water droplets condensed on nanofibers in case of PA6/CH nanofibers coated wire mesh (Figure 6b). The nanofiber surface increases the effective area for catching the water droplets [14]. When PCL particles were sprayed onto PA6/CH nanofibers a decrease in the water capturing performance of the mesh was observed (Figure 6c). This can be explained by the reduction of the hydrophilic area on the mesh surface.
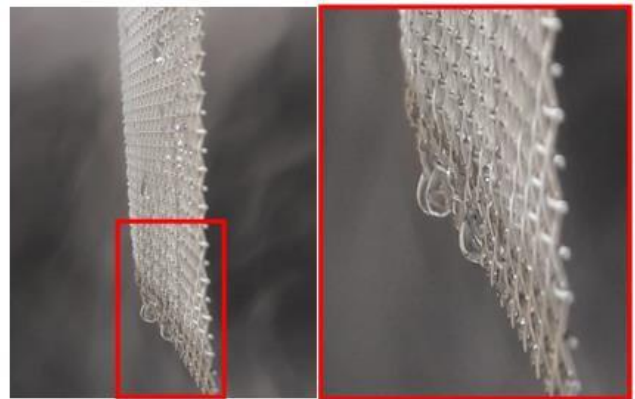

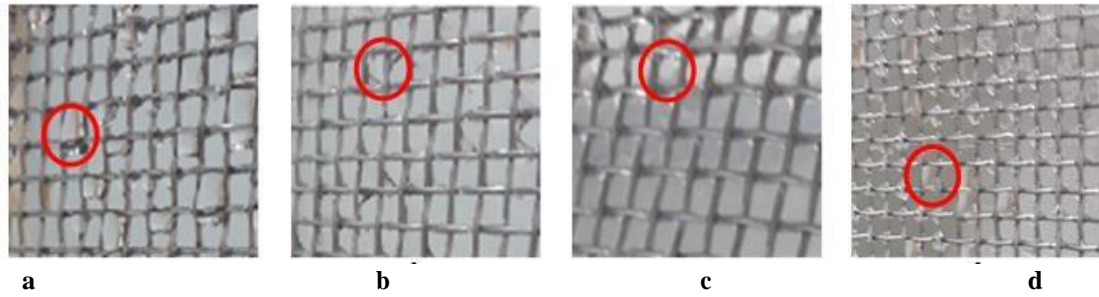**Figure 5.** Water harvesting from coated mesh

Figure 6. Water harvesting from **(a)** Uncoated wire mesh, **(b)** PA6/CH nanofiber coated wire mesh, **(c)** PCL sprayed onto PA6/CH nanofiber coated wire mesh, **(d)** PCL and PA6/CH sprayed onto the wire mesh

The water harvesting efficiency of samples was calculated at the end of the first hour according to the equation given by Huang et al.[8]. The results are given in Table 2. Huang et al. defined water harvesting efficiency as the weight of water per unit area per hour [9]. The highest water collection efficiency was obtained as 87 mg/cm^2/h with Sample 2. It was observed that the water harvesting capacity of the PA6/CH nanofiber coated wire mesh was two times higher than the uncoated wire mesh at the end of the first hour. After coating with hydrophilic nanofiber, the surface area of the wire mesh increased significantly. This increase led to higher water harvesting capacity. The addition of PCL to the nanofiber-coated surface (Sample 3) reduced the water harvesting capacity about five times compared with nanofiber-coated one. When both PA6/CH and PCL were in particle form (Sample 4) water harvesting capacity was increased slightly compared to Sample 3. It is likely that hydrophobic PCL particles masked the effect of hydrophilic PA6/CH.

Tablo 2. Water harvesting efficiency

Code	Efficiency (mg / cm^2/h)
Sample 1	45
Sample 2	87
Sample 3	17
Sample 4	25

Water harvesting capacities of the meshes versus time was given in Figure 7. The increase in the water harvesting capacity of Sample 2 slowed down after the first hour. Our experiments were conducted at a relatively low fog flow speed due to the experimental setup. It is believed that the hydrophilic nanofiber surface reached saturation level after a certain period of time. A high fog flow speed could be able to shake the captured water between nanofibers and we probably would not see this slowing down trend. With the addition of PCL, the water harvesting capacity of the mesh dropped drastically. Since PCL is hydrophobic, the addition of PCL particles to the surface reduced the hydrophilic areas which play the main role in catching the water. When both PA6/CH and PCL were in particle form (Sample 4) water harvesting capacity of the mesh was slightly better than Sample 3.
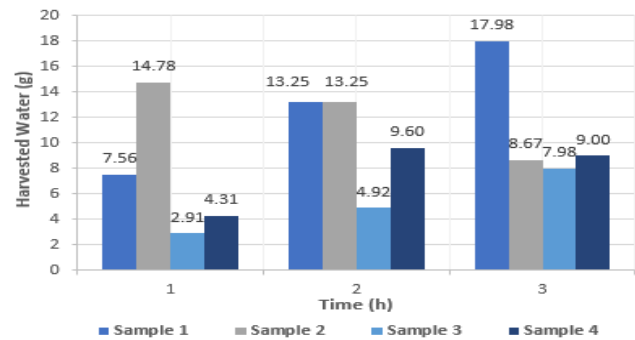

Figure 7. Water harvesting capacities of meshes with changing time

4. CONCLUSION

This study focused on increasing the water harvesting capacity of traditional wire meshes. For this purpose, hydrophilic nanofibers and hydrophilic/hydrophobic nano or microparticles were incorporated on the surface of a wire mesh. Wire meshes are effective tools to capture and condense water from fog. It was observed that the water harvesting capacity of a wire mesh can be controlled by modifying the mesh surface with hydrophilic and hydrophobic polymers. The coating of the mesh surface with hydrophilic nanofibers significantly increased the water harvesting capacity due to increasing surface area. However, when the nanofibers reached the saturation level the water capturing efficiency decreased. Water harvesting capacity was decreased sharply by the addition of hydrophobic particles onto hydrophilic nanofibers. Hydrophobic particles masked the hydrophilic zone and reduced the water capturing ability of the mesh. From these results we can conclude that the wire mesh covered with the hydrophilic nanofiber web was more effective in capturing water droplets from the fog, however, it seems that a new strategy is necessary to collect the captured water droplets from the mesh. In our experiments, gravity was the main force responsible for water collection. In addition to gravity force, applying a mechanical force such as shaking the mesh at regular time intervals might provide better outcomes. Additionally, the sustainability of the nanofiber coated mesh needs to be addressed in order to use it in practical applications.

REFERENCES

1. Claire, S.,2002, The Last Drop. *Mazaya Summer Issue*, 22–25. 2.

2. Eslami, M., Tajeddini, F., Etaati, N., 2018, Thermal analysis and optimization of a system for water harvesting from humid air using thermoelectric coolers. *Energy Convers. Manag.*, 174, 417–429.

3. Alkaisi, A., Mossad, R., Sharifian-Barforoush, A.,2017, A review of the water desalination systems integrated with renewable energy. *Energy Proc.*,110, 268-274.

4. Park K.C, Chhatre S.S, Srinivasan S., Cohen R.E., McKinley G.H., 2013, Optimal design of permeable fiber network structures for fog harvesting. *Langmuir*, 29, (43), 13269–13277.

5. https://www.smithsonianmag.com/science-nature/five-wild-ways-get-drink-desert-180952845/ (Accessed: 08.07.2021)

6. Parker, A.R., Lawrence, C.R.,2001, Water capture by a desert beetle. *Nature*, 414, (6859), 33–34.

7. Zhai, L., Berg, M.C., Cebeci, F.C., Kim, Y., Milwid, J.M., Rubner, M.F., Cohen, R.E.,2006, Patterned superhydrophobic surfaces: toward a synthetic mimic of the Namib Desert beetle. *Nano Lett.*,6, 1213–1217.

8. Huang, Z.X., Liu, X., Wu, J., Wong, S.C., Qu, J.P., 2017, Electrospinning water harvesters inspired by spider silk and beetle. *Mater. Lett.*, 211, 28–31.

9. Huang, Z.X., Liu, X., Wong, S.C., Qu, J.P.,2019, A single step fabrication of bio-inspired high efficiency and durable water harvester made of polymer membranes. *Polymer*, 183.

10. Garrod, R., Harris, L., Schofield, W., McGettrick, J., Ward, L., Teare, D., Badyal, J., 2007, Mimicking a Stenocara Beetle's back for microcondensation using plasmachemical patterned superhydrophobic superhydrophilic surfaces. *Langmuir*, 23, (2), 689–693.

11. Feng, L., Li, S., Li, Y., 2002, Super-hydrophobic Surface: from Natural to Artificial, *Advanced Materials*, 14(24), 1857–1860

12. Kenneth, K., S., Lau José Bico Kenneth, B., K., Teo Manish Chhowalla Gehan A. J. Amaratunga William I. Milne Gareth H. McKinley Karen K. Gleason, 2003, Superhydrophobic Carbon Nanotube Forests, *Nano Letters*, 3, 12, 1701-1705

13. Ghosh R., Ray T., Ganguly R., 2015, Cooling tower fog harvesting in power plants e A pilot study, *Energy*, 89, 1018-1028

14. Knapczyk-Korczak, J., Szewczyk, P. K., Ura, D. P., Berent, K., Stachewicz, U., 2020, Hydrophilic nanofibers in fog collectors for increased water harvesting efficiency, *The Royal Society of Chemistry* ,10, 22335–22342

15. Nirmala, A., Navamathavan, R., Kang, H.,S., El- Newehyd, M.,H., Kim, H.,Y., 2011, Preparation of polyamide-6/chitosan composite nanofibers by a single solvent system via electrospinning for biomedical applications, *Colloids and Surfaces B: Biointerfaces*, 83, 173– 178.Martinová, L., Lubasová, D., 2008, Electrospun chitosan based nanofibers, *RJTA*., 12(2), 72-79

16. Martinová, L., Lubasová, D., 2008, Electrospun chitosan based nanofibers, *RJTA*., 12(2), 72-79

17. Woodruff, M., A., Hutmacher, D., W., 2010, The return of a forgotten polymer Polycaprolactone in the 21st century. *Progress in Polymer Science journal*, 1217-1256